

**MULTISCALE IMPLICATIONS OF STRESS-INDUCED IONIC POLYMER
TRANSDUCER SENSING**

by

Ursula Thérèse Zangrilli

BSME, Villanova University, 2006

Submitted to the Graduate Faculty of

Swanson School of Engineering in partial fulfillment

of the requirements for the degree of

Doctor of Philosophy

University of Pittsburgh

2013

UNIVERSITY OF PITTSBURGH

SWANSON SCHOOL OF ENGINEERING

This dissertation was presented

by

Ursula Thérèse Zangrilli

It was defended on

April 12, 2013

and approved by

Jung-Kun Lee, Ph.D., Assistant Professor, Department of Mechanical Engineering and Materials
Science

Albert To, Ph.D., Assistant Professor, Department of Mechanical Engineering and Materials Science

Qing-Ming Wang, Ph.D., Professor, Department of Mechanical Engineering and Materials Science

Maurizio Porfiri, Ph.D., Associate Professor, Department of Mechanical and Aerospace Engineering,
New York University

Dissertation Director: Lisa M. Weiland, Ph.D., Associate Professor, Department of Mechanical
Engineering and Materials Science

Copyright © by Ursula Zangrilli

2013

MULTISCALE IMPLICATIONS OF SHEAR-INDUCED IONIC POLYMER TRANSDUCER SENSING

Ursula Zangrilli, PhD

University of Pittsburgh, 2013

Ionic Polymer Transducers (IPTs) can act as both actuators and sensors. As actuators, the energy density values are much better than PZT or PVDF materials. As sensors, IPTs are extraordinarily sensitive and have the potential to be used in any mode of deformation. However, application of IPT sensors is limited because of a lack of understanding of their fundamental physics. In this work, the main focus will be to explore and develop a better understanding of how IPTs function with respect to shear deformation. In turn, the results developed here will improve upon the state of understanding of IPT sensors in general and potentially expand meaningful application opportunities.

Because IPT active response is a multiscale phenomenon, this study adopts a multiscale modeling framework. Of interest are the interplay among the polymeric backbone of the ionic polymer, the diluent present in the hydrophilic regions of the polymer and the interspersed electrode particulate.

To begin, this work improves upon a past multiscale modeling framework for the polymer backbone based upon Rotational Isomeric State Theory such that the effects of material anisotropy may be considered. This is potentially significant in light of the polymer manufacturing process. These modeling results are then incorporated into a model of the diluent movement within the ionic transport regions of the IPT. The electrical current predictions are based upon streaming potential theories. Finally, this model incorporates viscoelastic behavior

in order to develop a better understanding of the coupling of these two systems (the polymer and the diluent) and how this coupling influence affects the expected current output over time.

TABLE OF CONTENTS

ACKNOWLEDGEMENTS	XVI
1.0 INTRODUCTION.....	1
2.0 BACKGROUND AND LITERATURE REVIEW.....	4
2.1 IPT MICROSTRUCTURE AND MORPHOLOGY	5
2.2 IPT TRANSDUCTION	11
2.2.1 Role of diluent uptake and type on IPT transduction	11
2.2.2 Role of cation type on IPT transduction.....	12
2.2.3 Role of stiffness on IPT transduction	13
2.3 MODELING BACKGROUND	14
2.3.1 Rotational Isomeric State Theory.....	14
2.3.2 Transduction Models.....	16
2.3.3 Streaming potential theory.....	19
2.4 THE ROLE OF THE ELECTRODE	24
2.5 IPT SENSORS: STATE-OF-THE-ART SUMMARY	27
3.0 MULTISCALE MODELING	28
3.1 FUNDAMENTAL THEORY	29
3.2 MODEL DEVELOPMENT.....	31
3.2.1 Statistical assessment	33

3.2.2	Anisotropic considerations.....	35
3.3	RESULTS AND DISCUSSION.....	38
3.3.1	Isotropic stiffness predictions	38
3.3.2	Anisotropic stiffness predictions.....	46
3.4	INITIAL SENSING SIGNAL PREDICTIONS.....	48
3.4.1	Sensing for assumptions of isotropy.....	49
3.4.2	Effect of hydration level on sensing.....	53
3.4.3	Sensing for assumptions of anisotropy.....	54
3.5	METHODOLOGY STRENGTHS AND WEAKNESSES.....	56
3.6	CHAPTER SUMMARY	56
4.0	SHEAR MODEL.....	58
4.1	‘SINGLE BODY’ MODEL DEVELOPMENT.....	61
4.1.1	Bio-inspired approach to modeling shear induced flow.....	61
4.1.2	Geometric dimensions	63
4.1.3	Force application.....	64
4.1.4	Mesh Verification.....	67
4.2	‘TWO BODY’ MODEL DEVELOPMENT	68
4.3	RESULTS AND DISCUSSION.....	71
4.3.1	Analysis of one-body model.....	71
4.3.2	Analysis of the effects of channel orientation on streaming current.....	76
4.3.3	Analysis of the ‘two body model’.....	81
4.4	METHODOLOGY STRENGTHS AND WEAKNESSES.....	84
4.5	CHAPTER SUMMARY	85

5.0	TRANSIENT SHEAR MODEL	86
5.1	BACKGROUND REVIEW FOR MODEL DEVELOPMENT	86
5.2	MODEL DEVELOPMENT	89
5.2.1	Viscoelastic model	89
5.2.2	Polymer chain evolution	91
5.2.3	Boundary and initial conditions	94
	5.2.3.1 Mechanical initial conditions	94
	5.2.3.2 Electrical initial conditions.....	96
	5.2.3.3 Channel boundary conditions and electrolyte velocity equation....	97
5.2.4	Simulation Steps.....	100
5.3	RESULTS AND DISCUSSION	102
5.3.1	Step shear strain results	103
5.3.2	Oscillating shear strain results	113
5.4	METHODOLOGY STRENGTHS AND WEAKNESSES.....	119
5.5	CHAPTER SUMMARY	119
6.0	EXPERIMENTAL VALIDATION	121
6.1	EXPERIMENTS: ANNEAL VS. ISOTROPIC	121
6.1.1	Annealing Experimental procedure	123
	6.1.1.1 Preliminary Annealing Results	123
	6.1.1.2 Preliminary Annealing Procedure Alterations.....	125
6.1.2	Sensing Experimental Procedures.....	129
6.2	MODELING: ANNEAL VS. ISOTROPIC	129
6.2.1	RIS Predictions.....	130

6.2.2	Sensing Predictions	132
6.2.2.1	Free-energy calculations.....	133
6.2.2.2	Pressure response to bending deformation.....	135
6.2.2.3	Electrolyte velocity	137
6.3	DISCUSSION OF RESULTS	138
6.3.1	Experimental Results.....	139
6.3.2	Modeling Results.....	141
6.4	CHAPTER SUMMARY	145
7.0	CONCLUSION.....	146
7.1	PROCEDURE IMPLEMENTATION.....	148
7.2	CONTRIBUTIONS	149
7.3	FUTURE WORK.....	150
	APPENDIX A	151
	APPENDIX B	152
	BIBLIOGRAPHY	157

LIST OF TABLES

Table 3.1: Model scenarios	31
Table 3.2: Summary of isotropic model results where water is the diluent.....	41
Table 3.3: Effective energy for morphology considerations	43
Table 3.4: Comparison between model predictions and experiments	44
Table 3.5: Anisotropic stiffness calculations in Cartesian directions	47
Table 3.6: For fully hydrated, 5 mm x 15 mm, Na ⁺ exchanged IPT with 42% RuO ₂ electrode particulate [65]	51
Table 3.7: Comparison of variable and streaming current values for different IPT scenarios	53
Table 3.8: Ratio of anisotropic current predictions in bending	55
Table 4.1: Channel dimensions and orientations	64
Table 4.2: Wall boundary conditions.....	65
Table 4.3: Optimum mesh specifications for channel rotation.....	67
Table 4.4: EmI-Tf model input parameters.....	68
Table 4.5: EmI-Tf RIS stiffness results	69
Table 4.6: Shear strain, deflection and stress calculations for lithium-exchanged IPT of length = 50 mm	70
Table 4.7: Steady state streaming current for a single channel (From Figure 4.4(a-c)). Please refer to Figure 4.2 for θ and ϕ reference.....	75
Table 4.8: Input values and result for Equation 4.12.....	78
Table 4.9: Predicted steady-state streaming current value.....	81

Table 5.1: Optimal model discretization values	101
Table 5.2: Input Parameters	103
Table 5.3: Maximum current values for Li ⁺ ion models with different diluents	104
Table 5.4: Rate of current signal decay.	106
Table 5.5: Maximum current results for water cases, varied hydration.....	108
Table 5.6: Maximum current value comparison with different cations.....	109
Table 5.7: Input parameters for Equation 5.48	112
Table 5.8: α -values for different diluents at different frequencies	116
Table 5.9: Maximum current output comparison, given strain input	118
Table 6.1: Tension test sample and machine setup.....	124
Table 6.2: Preliminary Tensile Test Results	125
Table 6.3: As-received Moduli and Annealed Moduli under adjusted temperature and time conditions	127
Table 6.4: Weight measurements of <i>annealed</i> Nafion® both before and after EmI-Tf uptake .	128
Table 6.5: Weight measurements of <i>as-received</i> Nafion® both before and after EmI-Tf uptak	128
Table 6.6: RIS results for Na ⁺ , EmI-Tf IPT	130
Table 6.7: Semi-crystallinity estimates.....	132
Table 6.8: Complete summary of modeling and experimental work between the as-received and annealed polymer-based IPTs (for the specific case of the deflection = 15 mm).....	142
Table 6.9: Comparison of ratio trends between experiment and model	143
Table A.7.1: Anisotropic streaming current predictions.....	151

LIST OF FIGURES

Figure 2.1: Typical Ionic Polymer Transducer (IPT)	4
Figure 2.2: Morphology of ionic polymer regions: (a) Hydrophobic region (b) Amorphous / interface region (c) Hydrophilic ionic regions.....	6
Figure 2.3: Chemical formula for Nafion [®]	6
Figure 2.4: Cluster and connected channel morphology[Reprinted from Smart Structures and Systems, 6 (4), L.M. Weiland and B.J. Akle, Ionic Polymer Transducers in Sensing: The Streaming Potential Hypothesis,2010, with permission from Techno-Press[15]]	8
Figure 2.5: Rod-like structure [Adapted with permission from[16]. Copyright 2004. American Chemical Society]	8
Figure 2.6: Lamellae morphology structure	9
Figure 2.7: Cylindrical morphology structure	9
Figure 2.8: Qualitative comparison on the trends between actuation and sensing	12
Figure 2.9: (a) Effective anion and cation centers are aligned before added stress (b) After added stress; an effective dipole is created at the center of a cluster	19
Figure 2.10: EDL theory models (a) Simple Helmholtz model (b) Gouy-Chapman model [Reprinted from Cement and Concrete Research, 38, H. Friedman et al., Physical modeling of the electrical double layer effects on multispecies ions transport in cement-based materials, p. 1394-1440, 2008, with permission from Elsevier]....	20
Figure 2.11: Gouy-Chapman used in this model	22
Figure 2.12: Optimum electrode loading [Reprinted from Smart Structures and Systems, 6 (4), L.M. Weiland and B.J. Akle, Ionic Polymer Transducers in Sensing: The Streaming Potential Hypothesis,2010, with permission from Techno-Press[15]	27
Figure 3.1: Variable definitions in building a Teflon [®] chain from RIS theory. The bond angles are given by θ and φ , where the variables i and j represent the specific carbon atoms. [Reproduced from [25] with permission of IOP].	30

Figure 3.2: RIS conformations of Nafion morphology.....	32
Figure 3.3: Draw and extrusion in the z-direction. Figure 3.4: Drawing in z-direction, extrusion in x-direction	37
Figure 3.5: PDF of Na ⁺ -exchanged IPT with 15% uptake in EmI-Tf.....	39
Figure 3.6: PDF of Li ⁺ -exchanged IPT with 38% water uptake	40
Figure 3.7: Example of a normal distribution curve	40
Figure 3.8: Experimental vs. model stress-strain curve for sodium cubic.....	46
Figure 3.9: Predictions of the streaming current in bending with the local or global polymer modulus: sample type is sodium exchanged IPT with water as diluent	52
Figure 4.1: Streaming potential response to shear deformation	59
Figure 4.2: Rotation of IPT microchannel by θ around the x -axis and/or by ϕ around the y -axis.....	63
Figure 4.3: Boundary conditions for channel morphology	65
Figure 4.4: Li ⁺ exchanged, 38% water hydration, streaming current prediction responses for a single channel (a) Aligned parallel to load (b) Rotated in θ to load (c) Rotated in ϕ to load. Steady state current values are given in Table 4.7	74
Figure 4.5: Streaming current in a single channel as a function of angle rotation with respect to external shear load.....	77
Figure 4.6: Fourier transform of model results vs. experimental results	80
Figure 4.7: Deflection vs. absolute value of current (prediction of trend)	82
Figure 4.8: Predicted current output for $\delta= 13.6 \mu\text{m}$	83
Figure 5.1: Example of a graph indicating α - and β -relaxation. [Reprinted from <i>Journal of Power Sources</i> , 187/1, Di Nota, et al., Hybrid inorganic proton conducting membranes based on Nafion and 5wt% of MxOy (M=Ti, Zr, Hf, Ta and W). Part II: Relaxation phenomena and conductivity mechanism, 57-66, Copyright, with permission from Elsevier].....	88
Figure 5.2: Polymer channel region.....	90
Figure 5.3: 2N+1 Analogical model	90

Figure 5.4: Velocity boundary conditions	97
Figure 5.5: Residual calculations to determine spatial discretization.....	100
Figure 5.6: Residual calculation to determine temporal discretization.....	101
Figure 5.7: For a step input, Li ⁺ exchanged IPT, delta = 13.6 micrometers	103
Figure 5.8: Zoom in of the streaming current with water diluent (single channel results).....	105
Figure 5.9: Zoom in of the streaming current with EMITf diluent (single channel results).....	106
Figure 5.10: Comparison of total expected current for Lithium at different hydration levels (total current output).....	107
Figure 5.11: Total current output for a Li- and Na-exchanged IPT samples	109
Figure 5.12: Comparison of experimental[98] and estimated current outcome. Note: <i>No empirical fitting imposed</i>	110
Figure 5.13: Maximum current for different volume fractions of RuO ₂ (δ=13.6 μm).....	111
Figure 5.14: Current output for input strain of $\gamma = \delta \cos(\omega t)$	113
Figure 5.15: Plot of the average transient velocity	114
Figure 5.16: Predictions for an IPT with Li ⁺ , Water, $\omega = 10$ Hz, $\alpha = 1.745$	116
Figure 5.17: Output current for an IPT with $\omega = 5$ Hz and $\alpha=0.8725$	117
Figure 6.1: Illustration of bending deflection	133
Figure 6.2: 2D deflection	134
Figure 6.3: IPT cantilever, where δ is the macro displacement and P is an imposed force	136
Figure 6.4: Sample 1a, without annealing. Deflection values: Blue = 20 mm, Red = 15 mm, Green = 10 mm[128]	139
Figure 6.5: Sample 1b, with annealing. Deflection values: Blue = 20 mm, Red = 15 mm, Green = 10 mm[128].....	140
Figure 6.6: As-received Nafion®, IPT sensing results for step deflection input of 15 mm	141
Figure 6.7: Annealed Nafion®, IPT sensing results for step deflection input of 15 mm	142

Figure B.1: Picture of parallel channel mesh used in the generation of current predictions in Chapter 4..... 153

Figure B.2: Picture of mesh rotated $\pi/4$ in the xy plane 154

Figure B.3: Picture of channel, rotated in direction of $\pi/3$ with regard to model presented in Chapter 4..... 155

Figure B.4: Picture of channel, rotated in direction of $\pi/4$ with regard to model presented in Chapter 4. This rotation is with respect to the xz axis. 156

ACKNOWLEDGEMENTS

I would like to thank my committee for giving me their valuable time to review my work, offer insightful feedback and their support. Thank you also to the staff of the MEMS Department here at the University of Pittsburgh for helping me navigate through the paperwork of graduate school. Thank you to the National Science Foundation for funding this work under grant CMMI 0747123.

Thank you to my lab mates, past and present: Rich Beblo, Eric Freeman, Mark Delaney, and Tim Bagatti: for your invaluable friendship, guidance, always willing to answer questions and general 'coolness'. I want to give special thanks to my lab mates Fei Gao and Bilge Kocer not only for their friendship and guidance, but also for working with me on ionic polymer transducers.

Thank you to my friends, especially Cynthia Wu and Jean Schneider, who's patient tutoring in high school AP Physics played an important role in giving me the confidence to pursue engineering in college. Thanks to Veronica Miller for her PhD program mentorship. Thanks also go out to my brother, Albert and sister, Mary for your encouragement throughout this process.

Very special thanks to Dr. Lisa Weiland. Thank you for the opportunity to work for you and to learn from you. Thank you for trusting me. You have been and continue to be an awesome role model during this whole project and journey. Thank you!

Thank you to my mom and dad, Ursula McKenzie and Albert Zangrilli: thank you for all that you have done for me to help me be where I am today; from giving me chemistry sets when I was eight years old, but mostly thank you for always believing in me. I am truly blessed and I thank God every day to have such wonderful people and role models as my parents.

1.0 INTRODUCTION

Ionic polymers are a class of materials that can be manufactured into actuators or sensors. This is achieved by coating the polymers with electrode layers and then sandwiching them in between conductive films [1]. The resulting transducers are sometimes referred to as ionic polymer metal composites (or IPMCs), in reference to a method of fabrication. It is also common to refer to these actuators and sensors as ionic polymer transducers (or IPTs) which is more descriptive of the function. This work adopts the IPT naming convention with a focus on sensing.

IPTs will yield a measurable current when subjected to many types of deformation[2]. These qualities make IPTs of interest for use as sensors in applications ranging from industrial to medical, to measure any number of physical quantities, including velocity and wall shear stress[3,4]. There have even been reports of possible use of IPTs for energy harvesting storage, which can serve a wide range of purposes from wireless communication to wireless structural health monitoring[5]. The advantages of using these materials include that they are light-weight[6] and have significant sensitivity in charge-sensing mode[7]. Despite these advantages, IPTs are not widely used because of a fundamental lack of understanding of their sensing behavior.

This work explores the interplay between IPT mechanical stiffness and sensing via the streaming potential hypothesis. Classic streaming potential theory explains the evolution of a

potential when an electrolyte is sheared with respect to an electrode. This can be envisioned within an IPT due to the multiphase structure of an interpenetrating particulate electrode (such as RuO₂) and a diluent (such as water) and free counterions.

The study begins with application of Rotational Isomeric State (RIS) theory in order to model the IPT mechanical stiffness at the local level. These results are coupled to the streaming potential hypothesis in order to predict the stiffness effect on diluent flow. It is believed that the streaming potential hypothesis will enable identification of what physical mechanism(s) play the most significant role in IPT sensing, thereby opening the opportunity for optimizing their effectiveness in an economical way.

Currently, there are multiple IPT sensing hypotheses, all of which can be calibrated to predict sensing in the bending mode. However, a truly robust hypothesis should be able to predict response for any mode of sensing. Only the streaming potential hypothesis is able to explain the IPT shear sensing mode, in addition to bending. Prior to the current work this argument had been strictly qualitative. In order to fully test the hypothesis, with the ultimate goal of discerning its legitimacy, quantitative predictive capability must be demonstrated. This work offers, for the first time, demonstration of the predictive capability of the streaming potential hypothesis in shear.

This dissertation will explore how the local properties affect the IPT signal from the micro- to the macro- scale primarily through computation. Chapter 2 will survey the current state-of-the-art with regard to modeling IPT transduction, with a focus on the important variables that affect IPT behavior. Chapter 3 will quantify how polymer stiffness evolves at the local level. This will include quantifying anisotropic effects on the local polymer stiffness. Chapter 4 will begin to outline how the streaming potential model can be quantified with respect to the

shear deformation of an IPT. Chapter 5 will extend the streaming potential model of IPT sensing in shear to consider the evolution of the sensing signal. Chapter 6 will present a preliminary experimental look into the modeling results presented in Chapters 3-5.

2.0 BACKGROUND AND LITERATURE REVIEW

On the device length-scale, IPTs consist of an ionic polymer, with an interpenetrating electrode region, sandwiched between conductive foil layers (Figure 2.1). This ionic polymer is typically Nafion®, but other commercial variants exist, including Flemion®. There are a few fabrication methods to build an IPT. A common method is an impregnation-reduction technique[8]. Alternatively, there is the Direct Assembly Process[1]. Distinguishing between the methods is important because of their effect on the microstructure of the IPT, which is generally accepted to govern sensitivity.

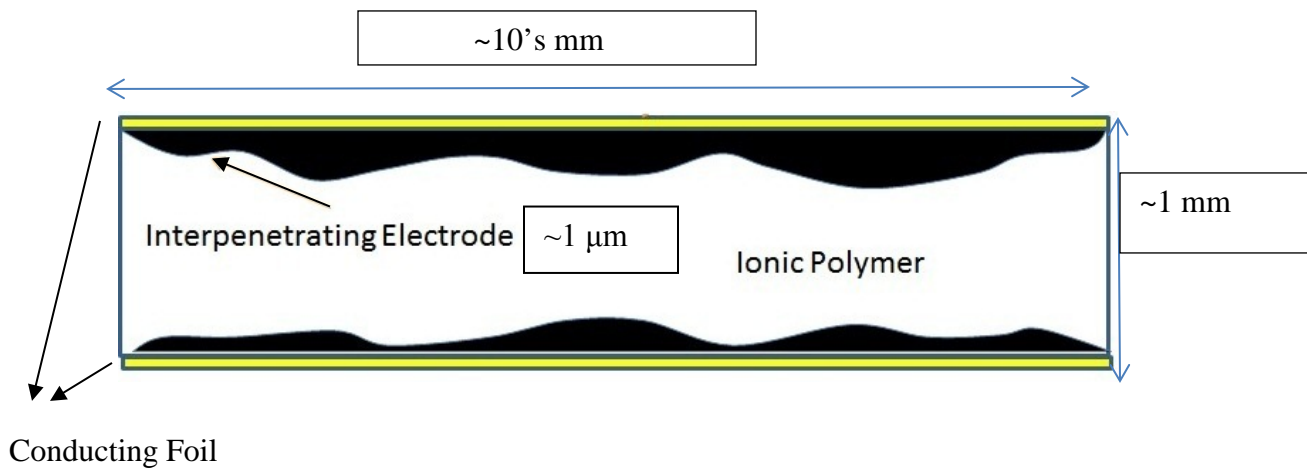


Figure 2.1: Typical Ionic Polymer Transducer (IPT)

2.1 IPT MICROSTRUCTURE AND MORPHOLOGY

The microstructure of the ionic polymer portion of an IPT is generally accepted to have three regions: (i) a hydrophobic backbone region typically made of polytetrafluoroethylene, also known as PTFE, or Teflon, (ii) a hydrophilic region populated with ionic groups; and (iii) an amorphous region with possible semicrystalline regions, depending upon the manufacturing process[9] (Figure 2.2). The term semicrystalline indicates there are both crystalline and amorphous regions in the polymer. The semicrystalline nature refers to how ordered the chains are packed together. This is in contrast to purely crystalline materials, where the polymers are packed into regular, and three dimensional arrangements. Key indications of semicrystalline polymers versus crystalline materials is in the material behavior at melting and glass transition temperatures [10] [11]. It is the backbone and the semicrystalline regions that determine the global strength of the material, while the ability to transport ions is determined by the morphology of the hydrophilic ionic regions. The monomer basis for Nafion[®] is given in Figure 2.3.

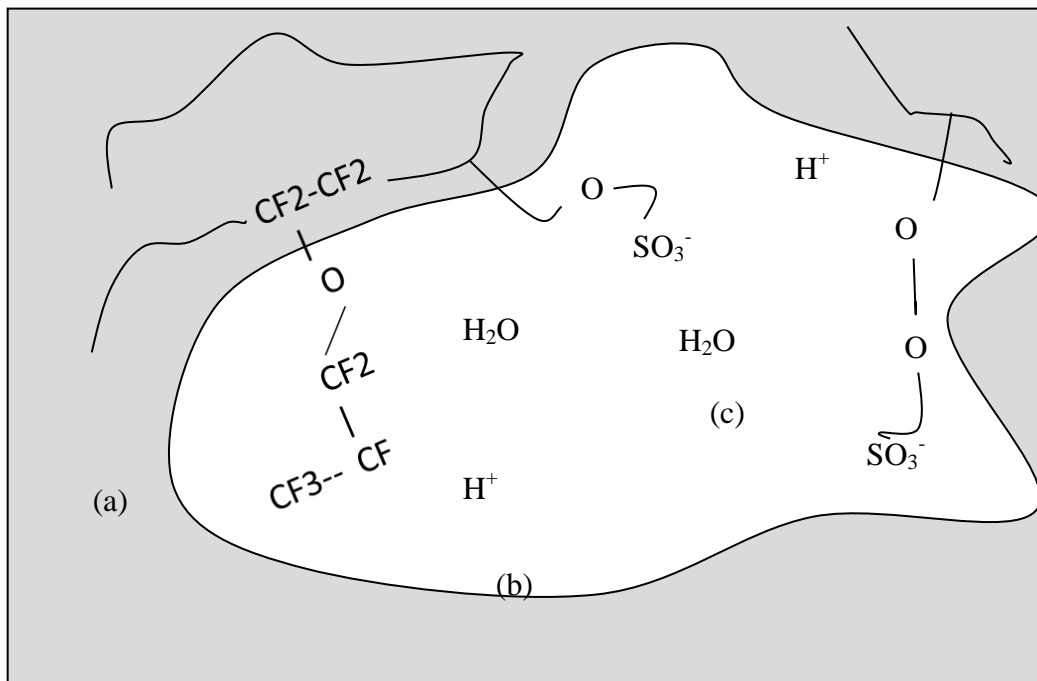


Figure 2.2: Morphology of ionic polymer regions: (a) Hydrophobic region (b) Amorphous / interface region (c) Hydrophilic ionic regions

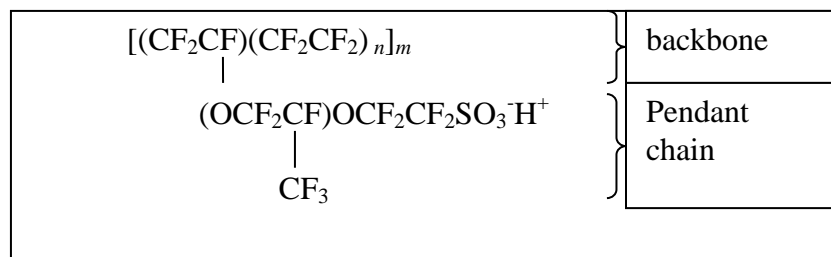


Figure 2.3: Chemical formula for Nafion®

This monomer is repeated m number of times to create a polymer chain, while the Teflon backbone portion (CF_2CF_2) is repeated n times, within a defined probability range. The portion of the molecular formula that branches from the backbone seen in Figure 2.3 is the pendant chain that terminates with an ionic group (usually sulfonate) which is hydrophilic. The relative

proportion of these ionic groups affects the ionomers ability to take up fluid. This important parameter is most often described in terms of equivalent weight (EW). EW is defined as the number of grams of dry Nafion® sulfonic group, when the associated counterion is H⁺ per [12]. EW is related to n as illustrated in Figure 2.3, but because n is a DuPont® trade secret, the relation is estimated as:

$$EW = 100n + 446 \quad 2.1$$

A second commonly used parameter for describing the fluid uptake of an ionomer is the hydration of the sample [13]:

$$w = \frac{V_{H2O}}{V_{dry}} \quad 2.2$$

where V_{H2O} is the volume of an IPT when the IPT is flush with a diluent and V_{dry} is the volume of an IPT under dry conditions.

Parameters such as EW and w receive considerable attention because it is understood that the extent of fluid uptake significantly affects IPT electromechanical transduction. It is therefore appropriate to next consider the current state of understanding regarding the hydrophilic regions. One of the initial hypotheses of the morphology of these regions was spherical clusters, connected by channels where the channels enable ion transport (Figure 2.4)[14]. Per this proposition the size and distribution of the clusters and connecting channels evolve with material state parameters including fluid uptake, counterion type and external loading.

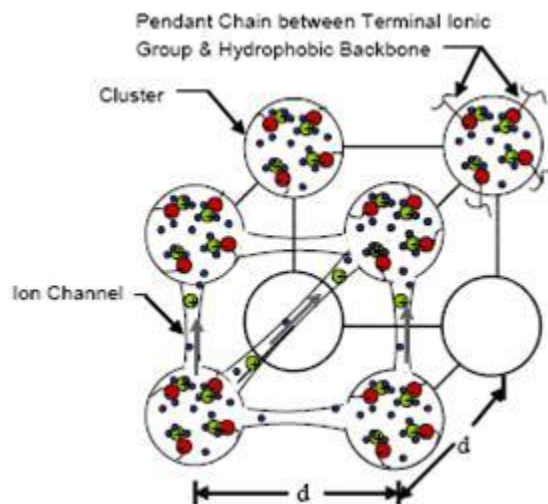


Figure 2.4: Cluster and connected channel morphology[Reprinted from Smart Structures and Systems, 6 (4), L.M. Weiland and B.J. Akle, Ionic Polymer Transducers in Sensing: The Streaming Potential Hypothesis,2010, with permission from Techno-Press[15]]

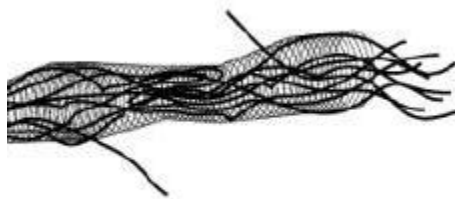


Figure 2.5: Rod-like structure [Adapted with permission from[16]. Copyright 2004. American Chemical Society]

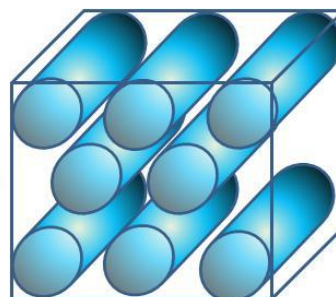
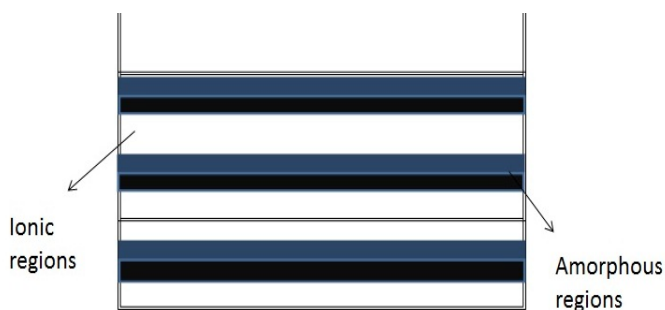


Figure 2.6: Lamellae morphology structure

Figure 2.7: Cylindrical morphology structure

The cluster model of Figure 2.4 is attractive due to its simplicity, but it is also generally accepted to be incorrect. While the exact morphology remains a point of debate, a significant number of alternate propositions exist with varying degrees of departure from the cluster model. The proposed size and shape of the hydrophilic regions can vary. It has even been suggested that the hydrophilic regions are inherently dynamic, coalescing and splitting under various conditions (such conditions can include mechanical load or humidity[17]) and at various times[14]. Further, these spheres could be scattered[18], or stacked in an HCP arrangement[19]. More recent, empirically inferred hypotheses argue significantly different cases including anisotropic aggregates (Figure 2.4)[20], lamellae (Figure 2.6)[21] or rod-like structures (Figure 2.5)[16].

Despite the fact that the details of ionic polymer morphology remain an open topic, it is widely accepted that communication among the clusters is critical for active response. For example, Hsu and Gierke, et al. note channels between the idealized clusters[14,22] and Kreuer discusses the ability of transport within ionic polymers with an eye toward fuel cell

applications[23]. Recently, the work by Schmidt-Rohr and Chen [24] postulates parallel channel morphology, has gained particular attention but still no consensus has been reached. Unifying characteristics of these proposed morphologies are (1) pathways must exist through which ionic transport may occur and (2) the elastic energy (stiffness) of the surrounding polymer plays a significant role in the ultimate morphology.

Next, therefore, consider the role of polymer stiffness. Most discussions of stiffness focus on variations of global stiffness. Global ionomer stiffness, which is measured in macroscopic experiments, is a function of multiple parameters including cation type, solvent type and hydration level[25]. Of course, global stiffness necessarily considers how mechanically robust the IPT is overall. However, the stiffness at the same time plays a role in electromechanical transduction. With regard to the role of stiffness in electromechanical transduction, there are two points to consider: (1) the role of polymer stiffness in the evolution of morphology and (2) the role of polymer stiffness in active response. Consider first the role of polymer stiffness in the evolution of morphology. It has been noted that when global stiffness effecting variables are adjusted, that there are noted differences in the morphologies of the ionic regions[20]. Thus, local stiffness is necessarily affected, which in turn has direct impact on the nature of the hydrophilic ionic transport pathways. In addition to this, and regarding the second point, stiffness – both local and global – necessarily plays a significant role in stimulating ionic transport through the morphological pathways when the IPT is deformed. Thus stiffness also effects transmission of IPT boundary conditions to the clusters thereby directly contributing to electromechanical transduction.

2.2 IPT TRANSDUCTION

There are several parameters that are known to affect IPT transduction behavior. These primarily include the diluent uptake, type of diluent and cation type. Further, and as mentioned already, significant interplay among these parameters and stiffness necessarily also exists.

2.2.1 Role of diluent uptake and type on IPT transduction

In the course of IPT production, regardless of method, an IPT is exposed to and will uptake into the hydrophilic regions of the polymer, a diluent. This has typically been water, however, other liquids have been considered. Specifically, ethylene glycol[26] and 1-ethyl-3-methylimidazoliumtrifluoromethanesulfonate (EmI-Tf) [1] have been considered for both sensing and actuation.

First, looking at actuation, results indicate a slower response from ethylene glycol when compared with water[26]. Similarly, EmI-Tf showed a slower response than ethylene glycol. However, EmI-Tf actuators display higher stability and longer life than those initially saturated with water.

Next, looking at sensitivity, it is first important to acknowledge that there is a different mechanism at work between this behavior and actuation[27]. Qualitatively, the level of voltage needed to actuate an IPT is much more than the converse voltage that can be obtained by deflecting the IPT the same distance (Figure 2.8)[28,29]. Again, water shows good sensitivity: up to a point. A weakness of water as a diluent is that an IPT sample saturated in water is subject to dehydration during the course of operation; hence, sensitivity varies during experimental characterization as the water in the IPT approaches equilibrium with ambient relative humidity.

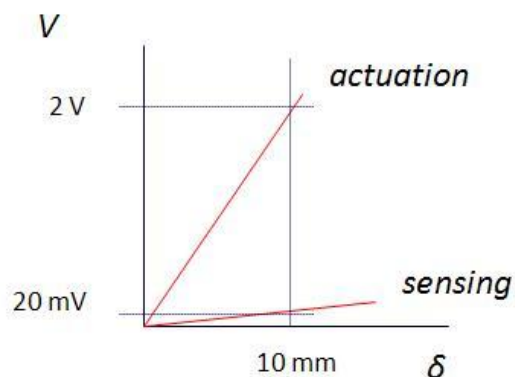


Figure 2.8: Qualitative comparison on the trends between actuation and sensing

Conversely, ionic liquids such as EmI-Tf have better stability: that is, this type of diluent is not subject to evaporation and IPTs with this as a diluent can be studied more precisely[30].

2.2.2 Role of cation type on IPT transduction

As shown in Figure 2.3, the pendant chains of Nafion[®] have a proton attached to the sulfonate group. In the as-received form of Nafion[®], the sulfonate ion is paired with a proton (H^+). While this is useful for fuel cell applications, the fabrication processes for an IPT can account for ion exchange to any number of other cation types, including (but not limited to) Li^+ , Na^+ , Rb^+ or K^+ [31,32]. These ions are exchanged with the initial proton by soaking a Nafion[®] membrane into a salt solution (such as NaCl or KCl). The salt solutions are typically at 1 M and the temperature of the solution is held at $80^\circ C$ for 24 h. However, this temperature and time duration can vary [9,25,31-33]

In terms of actuation, a key experimental hypothesis about how cations affect IPT behavior is the size of the cation. Specifically, this hypothesis suggests that exchanging to larger

ions results in IPTs with less force than those with smaller ions. It is argued that these smaller ions have better mobility values which aids transduction[33].

Interestingly, in terms of sensing, no analogous trend is noticed, for instance between sodium and lithium ions. A Na^+ exchanged IPT is about 5-10 times *less* sensitive than a Li^+ exchanged IPT. In contrast, the two IPTs display similar actuation behavior. In addition to these two ions, experimental studies have looked at cesium (Cs^+). The issue here is that Cs^+ yields sensitivities closer to that of Li^+ , however, Cs^+ atoms are bigger than both Li^+ and Na^+ [34]. Thus the size-mobility argument from actuation studies does not translate well to sensitivity studies.

In terms of macroscopic stiffness values, there is a range of values, even when comparing results for the same type of ion, once the sample is exchanged. For example, a Li^+ exchanged IPT with water as diluent can have a macroscopic stiffness from 75-160 MPa[9,32,35]. However, it is interesting to note that a qualitative trend is seen in increasing stiffness with the increasing size of the ions used in the ion-exchange process. The reason that such a trend is qualitative is given the variation in stiffness values that a particular ion-exchanged sample can exhibit[32,36].

2.2.3 Role of stiffness on IPT transduction

It is clear that stiffness is a key factor in the microstructure and the transduction performance of an IPT. For instance the experimentally reported stiffness of the ionomer layer can vary by as much as three fold, where this variation is often attributed to hydration variation as water evaporates from the IPT during characterization[9,37]. This results in both direct and indirect effects on IPT electromechanical transduction, which is a function of both stiffness and hydration. It is therefore not surprising that reported electromechanical response can also be variable.

For example, Nemat-Nasser et al. reports on micro-structural parameters that affect actuation. The model which the authors present is one where if the micro-scale forces are pushed out of equilibrium, then IPT actuation is observed. The authors' results link the stiffness indirectly to the actuation results, via how much the IPT is solvated [26].

Park and Moore report on how the stiffness affects the actuation of IPMCs. Again, while the stiffness is not a direct control variable, the authors are able to show that the curvatures obtained by the samples were inversely proportional to the bulk modulus of the IPMC [38].

2.3 MODELING BACKGROUND

There exists several ways to model IPT behavior currently in the literature. These include empirical, empirical-physics hybrids and physics-based models. These models vary in terms of empirical information needed in order for the model to be complete. These models can also vary in terms of applicable uses (i.e. transducer application or mode of transducer deformation). The physics based models built within this dissertation will draw upon fundamental physics including probability and streaming potential theories.

2.3.1 Rotational Isomeric State Theory

As discussed in the previous section, stiffness plays a significant role in IPT active response, beginning with lower length scale morphology evolution and concluding with higher length scale transduction effects. This section addresses a strategy to explore lower length scale stiffness, which is experimentally inaccessible. The approach explored is Rotational Isomeric

State (RIS) theory which was first developed by PJ Flory in the 1930s and continues to be among the most accurate approaches for relating physical crosslinking with material stiffness.

RIS theory has previously been used to preliminary explore local stiffness in Nafion[25,39,40]. This theory has its roots in the 1930s, when statistical approaches began and eventually assumed a dominant role in the treatment of polymer constitution, reactions and physical properties. Flory based this theory on the unique structural feature common to all rubberlike substances: long polymer chains, which rearrange themselves in other configurations under applied external stress. These deformations can occur without suffering permanent rearrangement. A key requirement is that the polymer chain system must also possess sufficient internal mobility to allow such required rearrangement [41]. Mathematically, from the development of a thermodynamic basis of Lord Kelvin through to the Second Law of Thermodynamics, it is shown that the elastic force which evolves within the polymer chain in response to an external force is a function of entropy[41].

While RIS theory has demonstrated good capability over the years since it was developed, there are still some issues with respect to polymer behavior that it does not address, such as entanglement issues. Prior work has looked at cross-linking that can change with time, available space and energy inputs; applicable to shape memory polymers (SMP)[42]. This prior work by Kumar and Shankar considered that the total stress is a combination of the stress from the single polymer chains (considered by RIS) and stress from junction constraints (not modeled in this dissertation). Junction means stress that arises especially due to physical entanglements. The primary concern with junction constraint theory as reviewed is that in order to account for these constraints in the molecular modulus, certain constants are derived that can lead to instabilities (mathematically, the denominator goes to zero). In terms of the SMP studies, even

when these denominator values are assigned particular values, these additional considerations cannot account for differences between experiments and the RIS calculations [42].

This dissertation expands on RIS and the extended theoretical details of this approach will be covered in Chapter 3.0

2.3.2 Transduction Models

The models that have been proposed thus far to explain IPT transduction behavior can be classified into a few categories: black box/empirical, grey box/empirical-physics based hybrids, capacitive and physics-based. Black box models take the approach of relating certain macroscopic and measurable quantities to measured outputs [43]. The grey box models include some physical consideration; they remain limited to specific types of transducer development [44-46]. Physics based models take the approach of developing expressions to explain the IPT behavior, but from a starting point of fundamental physics (such as electrostatics and mechanics [43]). Among the grey-box and physics based models are the hydraulic models. These models focus primarily on the actuation properties of the material[47,48], whereas this dissertation seeks to unveil physical mechanisms responsible for sensing. Thus the hydraulic models are not considered in detail here.

Also among the grey-box and physics based models are capacitive type models which seek to determine charge accumulation vis-à-vis mechanical deformation. Some models have attempted to look at this relationship in a time domain while others focus on frequency domain characterization[7]. In terms of actuation, a voltage is applied to an IPT and the resulting current flow is measured. These variables are related via impedance[7]:

$$\frac{V(j\omega)}{I(j\omega)} = (Z'(\omega) + jZ''(\omega)) \quad 2.3$$

However, it is the dielectric properties that are of interest in these capacitive type models because it is the dielectric relaxation that is related to how electric charges are affected by an electric field[49]. The dielectric properties of a material come from a simple electrical relationship of Equation 2.3 via the impedance by[7]:

$$\frac{Q(j\omega)}{V(j\omega)} = \frac{1}{j\omega Z(j\omega)} = C(j\omega) \quad 2.4$$

and by the relationship between the capacitance and the permittivity[50]:

$$\epsilon(j\omega) = \frac{C(j\omega)t}{\epsilon_0 A} = \epsilon'(\omega) - j\epsilon''(\omega) \quad 2.5$$

where t is the thickness of the ionomer, A is the surface area of the electrodes and ϵ_0 is the permittivity of vacuum. It is from Equation 2.5 that ionomer dielectric relaxation (and hence charge movement) can be characterized. For instance, at low-frequency values, experimentally measured high permittivity has been interpreted as charge accumulation at the electrode[51]. Equivalent circuit models are then employed in order to link this math with physical regions of the IPT[7]. The equivalent circuit models can be tailored to investigate more detailed aspects of IPT behavior such as short-range ion motions. This was presented in a lumped “Debye” element by Deng and Mauritz, where elements such as a resistor is meant to capture ionic migration or drift, and a capacitor is meant to represent the membrane/electrode interface[49]. Other similar papers have constructed models of the permittivity to explain how ionic polymers behave[52,53].

Among the physics based models of sensing, only the dipole model of Li and Nemat-Nasser has met with some success[54], which has since been expanded by Porfiri[43]. Porfiri's expansion takes into account critical physical factors not considered in prior work such as the effects of solvent migration and polymer relaxation. The strength of this model is the focus on

the micromechanics energy of the system. This includes all parts of the system, such as the electrostatic energy of clusters and the elastic energy of the polymer backbone. Further benefit of this model is the use of homogenization techniques (such as multi-inclusion model and self-consistent approaches) to link the micro-morphology and hydration levels to the mechanical characteristics of the IPT. However, there is still dependence on unknown parameters to describe the sensing of the IPTs requiring application of unknown assumptions.

The fundamental assumption of the dipole model is that the pendant ionic groups are perfectly paired with cations. What this means is that the SO^{-3} and H^{+} , respectively in Figure 2.3, are perfectly paired in spherical cluster morphology. In the dipole hypothesis, mechanical deformation of the idealized configuration results in evolution of a dipole within the spherical clusters. However, even under the noted ideal conditions the described dipole mechanism cannot accommodate experimental observation of sensing under shear loading[55]. Furthermore, the assumption of ideal ion pairing is unlikely[12,56]. Conversely the hypothesis of the evolution of streaming potential, and subsequently a streaming current as the dominant mechanism in IPT sensing can accommodate each of the above noted discrepancies [15,57].

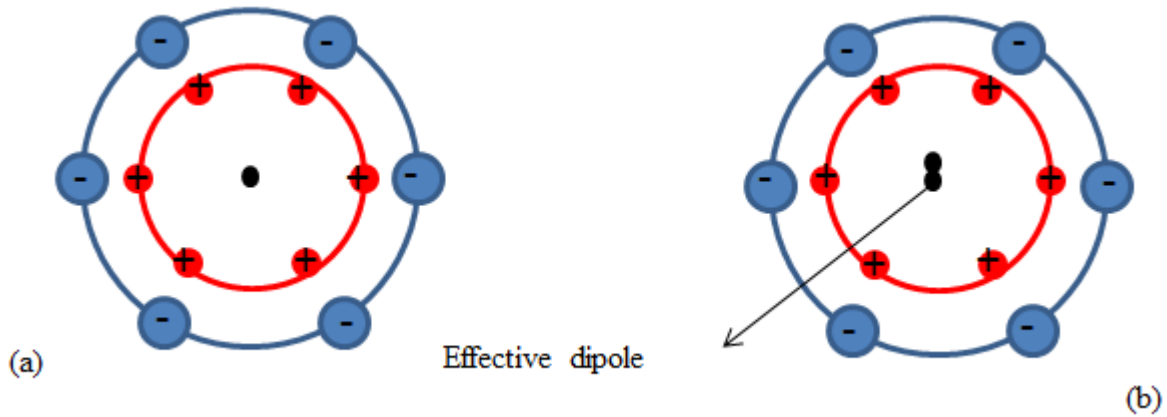


Figure 2.9: (a) Effective anion and cation centers are aligned before added stress (b) After added stress; an effective dipole is created at the center of a cluster

The fundamental physics explored in this dissertation is the streaming potential theory. Applying this to IPT behavior, the streaming potential theory has a similar thought process to the capacitive models recently reviewed, regarding surface area and charge accumulation, but explores lower length scale issues which open opportunity to explain phenomena such as sensing in shear.

2.3.3 Streaming potential theory

To appreciate the streaming potential theory within an IPT, it is important to first recall classic streaming potential theory. An electric double layer (EDL) forms when an electrode is immersed in an electrolyte, due to the electroneutralizing ions assuming close proximity to the electrode[58,59].

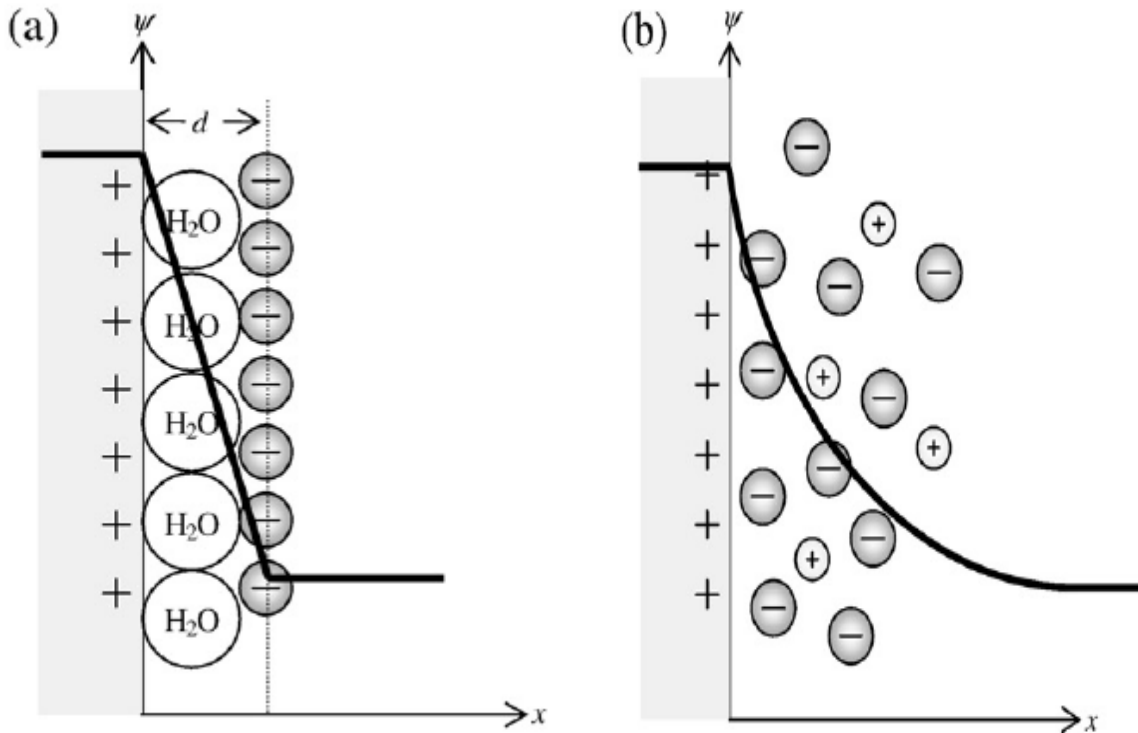


Figure 2.10: EDL theory models (a) Simple Helmholtz model (b) Gouy-Chapman model [Reprinted from Cement and Concrete Research, 38, H. Friedman et al., Physical modeling of the electrical double layer effects on multispecies ions transport in cement-based materials, p. 1394-1440, 2008, with permission from Elsevier]

If the liquid electrolyte is sheared with respect to the electrode, it will disrupt the EDL. This will give rise to a measurable streaming potential in the electrode. If the circuit is closed, current will flow. Thus, the liquid electrolyte response to stress can have a significant effect on the behavior of a system[60]. As noted, the EDL is a major factor in this theory; hence, how the EDL is modeled will in turn play a role in how a streaming potential will evolve.

The EDL models have grown more complex with the advent of more advanced scientific research. The first one to put together a model of the EDL was Helmholtz. This simple model presented the ions on a metal electrode surface balanced by ions of opposing charge immediately on the outside of the metal layer (Figure 2.10(a)). In this model, the bulk solution was quite

prominent. However, the mobility of the ions in the electrolyte was thought to be more complex. This thought yielded the Gouy-Chapman model where the distribution of ions (similar to the charge at the surface of the electrode) follow a more exponential decrease approaching the bulk electrolyte solution[61] (Figure 2.10(b)). This distribution in ions within the EDL can follow a Poisson-Boltzmann distribution[62]. Some key points in this theory are a few assumptions: (i) symmetric ions (ii) the electric field is perpendicular to the channel wall and (iii) no convection in the channel.

There are extensive models within literature on how to model the EDL besides the Guoy-Chapman theory. They include approximations such as the Debye-Hückel theory, which is an approximation based on the *size* of the EDL. Extensions from this Debye-Hückel approximation and theory include a Simple Stern layer model and a combined Stern-Helmholtz model. The Simple Stern layer model considers that there will be a specific layer which has absorbed counterions. Above this layer (called the Stern plane) is the slip plane where ions and diluent can move. The electric potential at this plane is where the zeta potential is defined. The combined Stern-Helmholtz model considers two layers of binding ions to the surface: an inner and outer Helmholtz plane, where ions and diluent can move past these two layers. In this model, the zeta potential is defined at the outer Helmholtz plane[62].

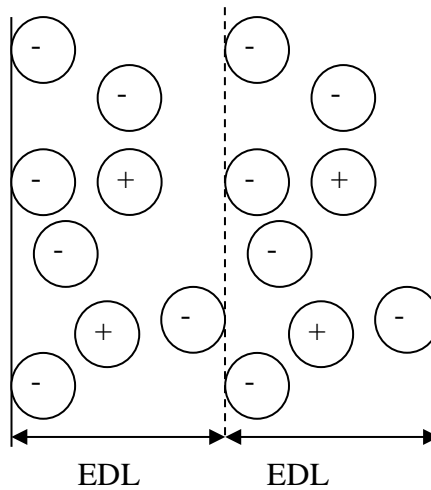


Figure 2.11: Gouy-Chapman used in this model

In the case of an IPT, unpaired ions exist in the diluent; in other words, an electrolyte exists in the hydrophilic region of the ionomer. This diluent comes into contact with the interpenetrating electrode, where an electric double layer is formed. For any deformation of the IPT the electric double layer will be disrupted, and a streaming potential will evolve. The strengths of this hypothesis include (i) while the magnitude of the predicted streaming potential/current will vary with assumed morphology, its existence can be argued for any morphology and (ii) while closed, analytical solution is in some cases elusive, the hypothesis is able to predict the existence of a sensing response under any deformation, including shear loading.

The application of the streaming potential hypothesis to explain IPT response in sensing was first used by Weiland and Akle[15]. Here, the authors show that it is the nature of the interpenetrating electrode within the electrolyte that ions are transferred to an equilibrium potential: from the high energy metal to the lower energy chemical energy phase[15]. Next, Gao

and Weiland quantify this hypothesis into a model for the case of bending. In the case of bending, the velocity of the diluent can be solved analytically via a Poiseuille flow[63]:

$$v(x) = \frac{1}{2\eta} \frac{\Delta p}{l} (h^2 - x^2) \quad 2.6$$

This velocity expression is used in the general equation for the streaming current[64]:

$$I_s = w \int_{-h}^h \rho(x) v(x) dx \quad 2.7$$

where $\rho(x)$ is the charge density in the hydrophilic region described as a channel, w is the width and h is the height of the channel. In the case of bending, the IPT is modeled as a cantilever beam, enabling the calculation of the pressure gradient in terms of the stiffness:

$$\frac{\Delta p}{l} = \frac{3E}{L_f^2} \delta \quad 2.8$$

where E is the Young's modulus of the IPT, l is the length of an hydrophilic channel, L_f is the free length of the IPT sample and δ is the imposed deflection[63]. Also, Gao expands this model to investigate trends in the model to predict how the IPT current would behave over a range of deflections. Further, she demonstrates that the strength of the EDL (in other words, if the EDL from the opposite walls overlap) makes a difference in how the current evolves. This is because if the EDL overlaps, it creates a unipolar solution, which in turn affects the dynamics of the diluent [65] and the charge density becomes a constant value.

Therefore, a key effect to consider is the size of the EDL and the size of the channel width. First, if the size of the channel is very small (<2 nm), several additional forces may arise such as ion-correlation effects, steric effects, image forces and/or solvation forces[62].

The second consideration is whether the EDLs from opposite sides of the channel overlap or not. This affects models of the flow of the fluid velocity within the channel. For example, if the EDLs do *not* overlap, the EDL potential and streaming potential should be added in superposition[62]. A common key factor when considering this type of EDL model is a question

of how the charge distribution and velocity changes with respect to the EDL and the ‘bulk’ part of the channel.

However, if the EDLs *do* overlap, the EDL potential is *not* zero in the middle[66]. Further, overlapped EDLs make a difference in the ‘relaxation processes’. That is, the time that it takes to re-establish equilibrium of the charge distribution is greatly affected by the overlapped EDLs vs. non-overlapped EDLs[67].

In this work, the Gouy-Chapman model (without the Stern layer) is adopted. The reason for this is that the Stern layer is a layer that adsorbs ions onto the surface and hence there is no current flowing in this layer. The reason for this choice is that these channels are assumed to be of such a small size that such a Stern layer does not have the space or time to develop. Therefore, there is no ‘bulk solution’ in this model. Instead, the layers overlap each other as shown in Figure 2.11. Thus, this defines the zeta potential as the potential at the channel.

2.4 THE ROLE OF THE ELECTRODE

Physically, electrodes are quite varied. They can be composed of particles of RuO₂, platinum (Pt) or even organic conductors[68]. Further, the shape can include dendritic structures and can vary in thickness[15,26]. Electrodes can be built onto an IPT in primarily one of two ways: impregnation-reduction method or the direct assembly process (DAP).

A brief summary of the impregnation-reduction process is as follows. The first step is to roughen the surface of the polymer. The purpose of this step is to increase the surface area density where the Pt ions will enter the polymer[33]. Next, the polymer is soaked in a Pt solution in order to thoroughly coat the material with Pt ions. Third, a reducing agent (such as

NaBH₄) is introduced in order to convert the Pt to metal precipitates. At the completion of this step, a conductive, electrode layer has developed on the polymer surface[38]. While this method is reliable in that it creates IPTs, there are a few drawbacks. For example, it is very difficult to control the electrode architecture with this method. Also, this method limits the type of electrode particles that can be built onto the polymer[1].

A more recent method to incorporate electrodes in an IPT is the DAP. There are two options to applying the electrode to the polymer base via the DAP: begin with a dry or solvated membrane. If the process begins with the dry membrane, the steps start with dissolving liquid ionomer and dispersing conductive powder into an alcohol solution. Next, this solution is painted onto the polymer surface, with additional baking steps. Finally, gold layers are hot pressed onto the polymer surface. A second option involving ‘solvated’ membranes is outlined because this first option of ‘dry’ membrane may not work as well for some diluent options. While this method may have drawbacks in terms of swelling, this method addresses the issue of electrode uniformity found in the impregnation-reduction method. As will be discussed, the electrode is very important in terms of how the IPT performs, in either actuation or sensing[1].

Experiments have investigated many aspects of electrode particulates: including thickness and concentration. For example, the work of Akle et al., performed experiments for actuators and found that the charge accumulation can be increased by increasing the volume fraction of electrodes (for a given, set electrode thickness). Further, that the current density increases with an increase in electrode thickness (for a given, set volume fraction of electrodes). This work also explored numerical models via field equations. While the results compared well with experiments, it did not give any insight into lower length scales[69]

The forgoing discussion draws attention to the role of electrode surface area, which has also been considered in terms of roughness. Increased polymer-electrode surface area not only represents increased opportunity for communication of an internally evolving streaming potential, it also represents increased charge storage in an IPT. The primary variable affected by the electrode roughness is the double-layer capacitance. Porfiri developed a model which quantified the roughness and the steric effects for a cantilever IPT in bending mode. The results indicate an increase in charge, capacitance and bending moment with increase surface roughness. This matched experimental results, thus leading to an effective model: again at the scales larger than the local level of the ionic polymer[70].

In terms of sensing, Weiland and Akle looked at electrode effects on the sensing signal. The author found that the loading of the electrode can create an optimum signal. That is, when the electrode particulate volume fraction is about 0.5, the predicted streaming current (in bending) is maximized, while a higher volume fraction is detrimental to the strength of the streaming current signal[65].

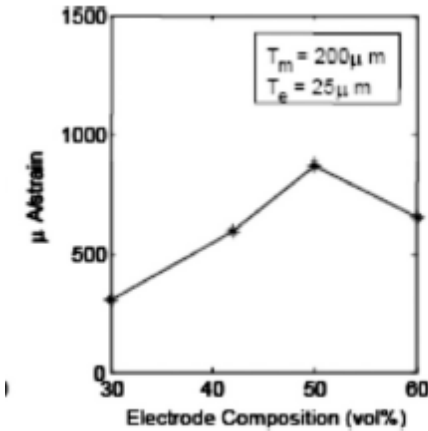


Figure 2.12: Optimum electrode loading [Reprinted from Smart Structures and Systems, 6 (4), L.M. Weiland and B.J. Akle, Ionic Polymer Transducers in Sensing: The Streaming Potential Hypothesis, 2010, with permission from Techno-Press[15]

2.5 IPT SENSORS: STATE-OF-THE-ART SUMMARY

There are many factors to consider when looking at IPT sensing. As discussed, there are several variables that play a role in how well the sensor performs such as the type of diluent, the amount of diluent and the type of cation exchanged into the polymer. These variables also play a role in how stiff the polymer is, thus creating a web of dependencies that need to be quantified. The modeling background presented in this chapter builds a foundation of the fundamental theory that will be used to quantify a model that can relate these variables in a way to describe the physics of IPT sensors. The RIS theory focuses on modeling the polymer chains. The streaming potential theory will focus on modeling the development of electric current in the polymer. These theories will be coupled in a way that considers the physical aspects of the IPT from the local to the macro level.

3.0 MULTISCALE MODELING

In this chapter, multiscale modeling is used to investigate local mechanical stiffness of ionic polymers considering both isotropic and anisotropic variations. To explore the postulate that local stiffness plays an important role in sensing, the chapter concludes by implementing the multiscale stiffness predictions in an existing sensing model for IPT bending.

One purpose of multiscale modeling is to assess parameters that would otherwise be inaccessible via experiment. To date, experimental characterization of Nafion stiffness for use in IPTs has focused on the global material stiffness. This measurement includes contributions from semicrystalline inclusions, hydrophilic cluster regions and polymer backbone stiffness. Conversely, the presented predictions are for backbone (local) stiffness only. While difficult, if not impossible, to experimentally isolate, this parameter is expected to play an important role in morphology evolution as well as sensing. The approach accommodates the observation that both stiffness and sensing response can be affected by cation type and hydration level.

Rotational Isomeric State (RIS) theory is used to predict the conformation of the hydrophobic backbone of a Nafion, 1200 equivalent weight (EW) ionomer in lithium and sodium forms. Then, the conformations under anisotropic processing are considered. The RIS method generates crosslink-to-crosslink chain lengths to assess material backbone stiffness. Both the stiffness and the effect on sensing predictions are compared to experiment for validation. It is observed that the local stiffness does not necessarily evolve in concert with the global stiffness.

However, the implications are consistent with, and offer an explanation of experimentally observed water uptake and sensing phenomena.

3.1 FUNDAMENTAL THEORY

It is important to consider first fundamental RIS principles as these are adapted for the model described in this chapter. This theory applies to ideal rubber networks, but requires additional consideration when discussing network structures or crystallization. An adaptation of Flory's theory and RIS principles is the Mark-Curro approach which helps explain short polymer chains. This work enables prediction of the polymer chain conformation with the constraint that a polymer chain can only take so many configurations.

It is appropriate to first review some basic terminology. The first important term is the 'bond-length' of the polymer backbone (Figure 3.1). In the case of Teflon®, this is the length between carbon atoms[71]. It is also important to understand the valence angle. This is the angle between adjacent bond lengths. The in-plane valence angle (θ) is fixed while the out of plane orientation, (φ) can vary.

For modeling purposes, the variation of φ is governed by statistical weight matrices. Statistical weight matrices are a way to describe the conformational characteristics of the polymer chains: for example, how the polymer chains move under deformation. These matrices are calculated based upon the rotational energy between the atom bonds within a polymer chain [72]. The energy differences between these configurations are temperature dependent and are used to populate these matrices[25].

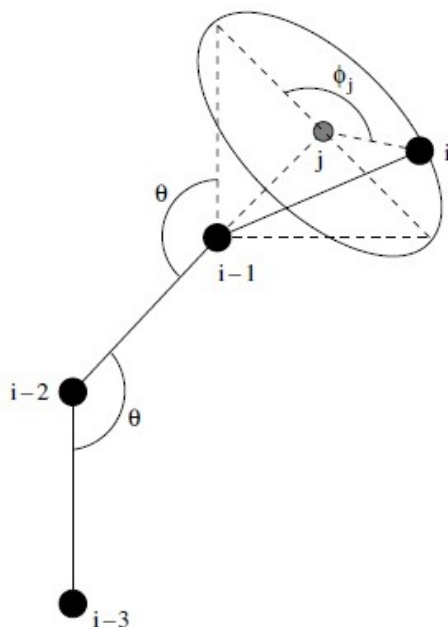


Figure 3.1: Variable definitions in building a Teflon® chain from RIS theory. The bond angles are given by θ and ϕ , where the variables i and j represent the specific carbon atoms. [Reproduced from [25] with permission of IOP].

These rotational angles can be based on a three state model or a four state model. In other words, ϕ can take on three or four discrete values so that the word ‘state’ refers to a particular conformation [39]. The identification of a low energy state ϕ is based on both probability and the orientation of the previous bond[25]. For the purposes of this system, these configurations are set to a four state model. This four state approach has previously been shown to appropriately capture chain coiling while the three-state model cannot. Per the method of Matthews et al., a pendant chain is placed approximately once per every 7 repeat units, where the actual frequency is sampled from a range between 5 and 11[25]. Finally, it is understood from the literature that a cross-link definition can be applied to this cluster placement because these

clusters restrict the mobility of the polymer chains and hence affect the overall deformation of the material [73,74].

3.2 MODEL DEVELOPMENT

The model predicts a low energy conformation of a Nafion backbone polymer chain within a volume of 5000\AA^3 . This setup is similar to the work of Matthews et al., where the longest possible, uncoiled polymer chain (according to the maximum m value – per Figure 2.3) could be contained within this grid[25]. The morphology, cation types and hydration are assumed *a priori* and are noted for various possible cases in Table 3.1. The scenarios were chosen in order to isolate cases for comparison. For example, these scenarios vary between the Li^+ and Na^+ exchanged IPTs, various morphologies, and hydration levels. The only “dehydrated” scenario is the first case for a lithium sample, where the cluster volume fraction is 10%. The cluster radius and center-to-center distance are a function of the cluster volume fraction, which is in turn a function of how much diluent is within the system. These variables are based upon the energy calculations of Li and Nemat-Nasser[54].

Table 3.1: Model scenarios

Cation	Cluster Packing	Cluster Radius (Å)	Center-to-Center Distance (Å)	Cluster Volume Fraction (%)
Li^+	Cubic spheres	12.6	32.7	10
Li^+	Cubic spheres	23	50.6	38
Li^+	HCP spheres	23	43.8	38
Na^+	Cubic spheres	21	50.4	30
Na^+	HCP spheres	21	43.6	30
Na^+	Parallel Cylinders	r = 12 h = 30	33.3	30

In order to predict a viable polymer backbone conformation, a carbon-to-carbon bond length of 1.53\AA and a fixed valence angle of $\theta = 116^\circ$ are applied; the statistical weight matrix described in the previous section is used to choose a low energy out-of-plane angle of rotation[25]. If the polymer backbone (hydrophobic) is predicted to coincide with a cluster (hydrophilic), or occupy a location outside the model's bounds, another low energy angle is chosen in order to avoid early termination[40]. It is assumed that, if the pendant chain placement point is within 8\AA of a cluster, communication occurs between the polymer backbone and the cluster and the location is noted and labeled as an r -value end point (Figure 3.2).

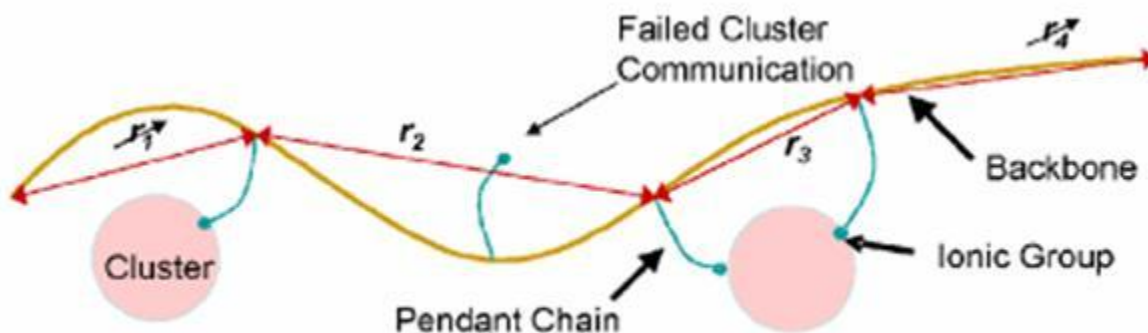


Figure 3.2: RIS conformations of Nafion morphology

Physically, an r value represents the distance between neighboring cluster induced crosslinks in the material system. The ultimate goal of this portion of the model is to generate a large number of r values ($\sim 10\,000$) in order to assess the probability density function (PDF) of the lengths. The r -values can be envisioned as analogous to trusses in a bridge which dictate bridge stiffness.

Thus, this PDF of r -values can be employed to estimate local material stiffness in the vicinity of a cluster.

3.2.1 Statistical assessment

A number of options exist for developing a PDF. Some of these options include cubic splines or Bézier functions[25,71]. In this work, the bounded function of the Johnson family of distributions is employed. This approach has previously been shown to be more consistent than the often applied binning approaches[25]. This is because in comparison to the Johnson families, the binning approach of the cubic spline method and Bézier functions are open to interpretation, depending on where certain points are chosen. In contrast the Johnson family of distributions is well defined and therefore comparatively immune to interpretation variations. The objective of the Johnson family of distributions was to create a standardized method for transforming variables into PDFs. The four families, or special forms of transformation, include: log-normal, unbounded, bounded and normal systems. The significant difference between these families is the transformation functions utilized. Johnson discusses the various ways that these transformation functions can be fitted in terms of the normal distribution [75].

The most general form of the Johnson function is given as

$$P(r) = \frac{\delta}{\lambda\sqrt{2\pi}} f' \left(\frac{r-\xi}{\lambda} \right) \exp\{-1/2[\gamma + \delta f \left(\frac{r-\xi}{\lambda} \right)]^2\} \quad 3.1$$

In Equation 3.1, the Johnson distribution fitting parameters are given as δ , γ (shape parameters), λ (scale parameter), and ξ (location parameter). These fitting parameters can be obtained via the FITTR1 software package. In addition to the fitting parameters, the FITTR1 program provides the Kolmogrov-Smirnov (K-S) statistic, which is a goodness-of-fit parameter. Also provided are

several fitting methods including: moment matching, ordinary least squares (OLS), diagonally weighted least squares (DWLS), L₁-norm and L_∞-norm estimations[25,75].

The root mean square r_o of the PDF is given as:

$$r_o = \sqrt{\int P(r)r^2 dr} \quad 3.2$$

Once defined, the PDF can be related to entropy according to Boltzmann statistical thermodynamics. Here it is assumed that the rotation of a bond is unrestricted under a load; thus the Helmholtz free energy is strictly a function of entropy and the nominal stress can be expressed as

$$f^* = \frac{-\nu k T r_o}{3} \left[G'(r_o \alpha) - \alpha^{-\frac{3}{2}} G' \left(r_o \alpha^{-\frac{1}{2}} \right) \right] \quad 3.3$$

where

$$G(r) = \ln[P(r)] \quad 3.4$$

$$G'(r) = \frac{dG(r)}{dr} \quad 3.5$$

In Equation 3.3, ν is the number density of network chains; k is Boltzmann's constant, T is temperature and α is change in length of the sample, defined as:

$$\alpha = \frac{L}{L_i} \quad 3.6$$

where L_i is the original length of the sample and L is the deformed length. The resultant modulus can be determined from[71]:

$$[f^*] = \frac{f^*}{\alpha - \alpha^{-2}} \quad 3.7$$

In the limit as $\alpha \rightarrow 1$, this modulus approaches Young's modulus. The stiffness of the polymer backbone can be determined via l'Hôpital's rule. This yields the expression[39]

$$E = \frac{-\nu k T r_o}{6} \left[\frac{r_o P(r_o) P''(r_o) - r_o \{P'(r_o)\}^2 + P(r_o) P'(r_o)}{P(r_o)^2} \right] \quad 3.8$$

In the studies performed here, five simulations were performed for the first four scenarios presented in Table 3.1 and the results will be noted and discussed in the Section 3.3. However, in order to consider the anisotropic effects on the polymer modulus, it is necessary to alter the mathematics of this section slightly. These modifications will be discussed in the following section.

3.2.2 Anisotropic considerations

The goal here is to adapt Equation 3.8 for isotropic Young's modulus to transversely isotropic and orthotropic cases. A reason to look at these cases is because experimental reports have shown that anisotropic properties resulting from material processing can affect the strength and conductivity of Nafion®[76,77]. Consideration of anisotropic effects via RIS proceeds in a similar manner as before except that the r -values now have direction as well as length.

Following the work of Sharaf et al., it is assumed that the polymer fibers will have an affine response to applied forces. An affine response means that the polymer fibers will deform in the same proportion. Further, the conservation of volume is assumed. This means that the principle components of the deformation tensor, α_x , α_y and α_z are related via Equation 3.9[78]

$$\alpha_x \alpha_y \alpha_z = 1 \tag{3.9}$$

Two external processes are considered here: extrusion and drawing. Extrusion is important because it is a common manufacturing method for polymers. Drawing is important because it is a manufacturing method that is used to impart semicrystallinity on polymers, or to enforce polymer chain alignment in a particular direction. This work considers (*i*) a case where extrusion

(α_e) and drawing (α_d) collinear and (ii) a case when the extrusion and drawing are applied perpendicularly, as noted in Figure 3.3 and Figure 3.4.

The final variable that requires consideration is the effective stretch (α_{eff}). Physically, the purpose of an effective stretch is to consider hydrodynamic effects of the polymer chains. Hydrodynamic effects account for interaction between the polymer chain ‘beads’ and the diluent. In this case, this means the interaction between the sulfonate groups in the electrolyte flow. The effective stretch is therefore defined as

$$\alpha_{eff} = \alpha_i X_{eff} \quad 3.10$$

where X_{eff} is an amplification factor defined by Equation 3.11 or Equation 3.12:

$$X_{eff} = 1 + 2.5v_f + 14.1v_f^2 \quad 3.11$$

$$X_{eff} = 1 + 0.676\delta v_f + 1.26\delta^2 v_f^2 \quad 3.12$$

Equation 3.11 is for sphere-like cluster morphology and Equation 3.12 is for cylinder-like cluster morphology. In these equations, v_f defines the volume fraction of clusters and δ is the aspect ratio of the clusters[78]. This aspect ratio is defined by the deformation of drawing, as given in Equation 3.13.

$$\delta = \alpha_d^{3/2} \quad 3.13$$

The amplification factors from Equation 3.11 and Equation 3.12 were developed in the 1930s to explore the effects of carbon black spheres in a rubber matrix [79] and has been applied to poly(ethylene) and to poly(dimethylsiloxane)(PDMS) by Sharaf et al. [78]. The physical origin of these equations is in Einstein’s theory of viscosity of colloidal solutions. The development of this theory was to investigate how elastic properties were altered by the presence of both spherical and rod-like fillers[79].

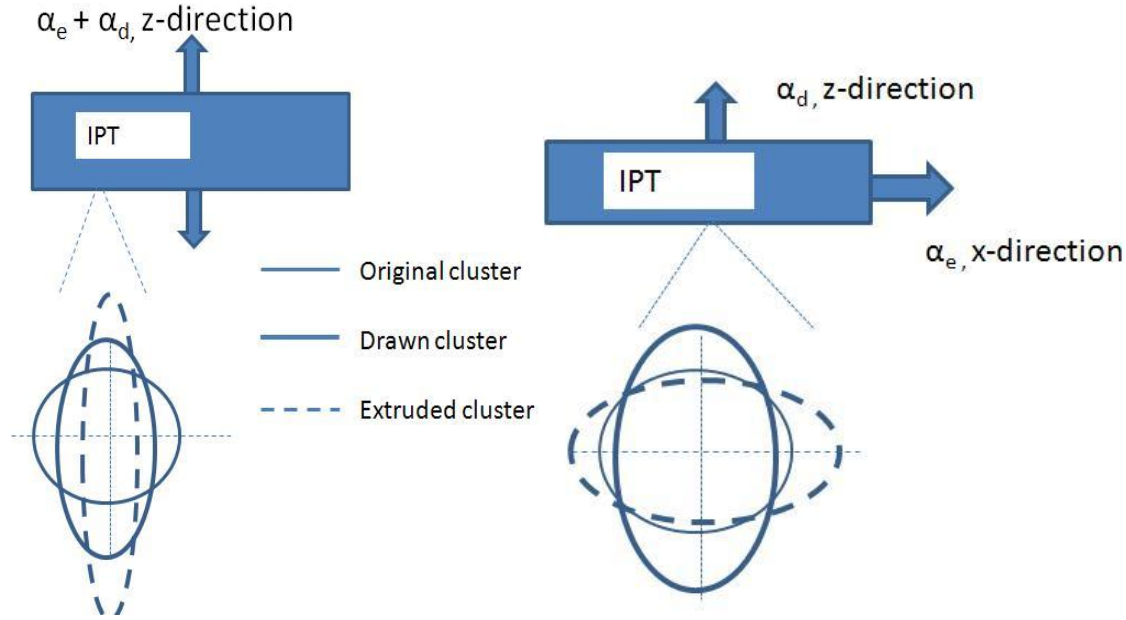


Figure 3.3: Draw and extrusion in the z-direction. Figure 3.4: Drawing in z-direction, extrusion in x-direction

So, the following is an example on how to apply these equations, to calculate the modulus in the z-direction for the case illustrated in Figure 3.3. The change in relative deformation is given by:

$$\alpha_z = \alpha_d \alpha_e \quad 3.14$$

Then, from Equation 3.9,

$$\alpha_x = \alpha_y = \frac{1}{\sqrt{\alpha_d \alpha_e}} \quad 3.15$$

With the change in relative lengths now defined, the nominal stress is re-defined from Equation 3.3 as:

$$f^* = \frac{-v k T r_o}{3} \left[G'(r_o \alpha_z) - \alpha_e^{-\frac{3}{2}} G'(r_o \alpha_{y,x}^{\frac{1}{2}}) \right] \quad 3.16$$

The modulus in the z-direction is then calculated using Equation 3.16 in Equation 3.7, applying l'Hôpital's rule with respect to α_e , as follows:

$$[f^*] = \frac{f^*}{\alpha_z X_{eff} - \alpha_z X_{eff}^{-2}} \quad 3.17$$

For this particular example, of the z -direction modulus, the equation would result in

$$E_z = \frac{-vkTr_o}{3} * \left\{ \begin{array}{l} \frac{\frac{d}{dr_o} \frac{d}{d\alpha_e} P(r_o, \alpha_e, \alpha_d)}{P(r_o, \alpha_e, \alpha_d)} - \frac{\frac{d}{dr_o} P(r_o, \alpha_e, \alpha_d) * \frac{d}{d\alpha_e} P(r_o, \alpha_e, \alpha_d)}{P(r_o, \alpha_e, \alpha_d)^2} + \\ \frac{3 \frac{d}{dr_o} P\left(r_o, \frac{1}{\sqrt{\alpha_e}}, \frac{1}{\sqrt{\alpha_d}}\right)}{2 * \alpha_e^{\frac{5}{2}} * P\left(r_o, \frac{1}{\sqrt{\alpha_e}}, \frac{1}{\sqrt{\alpha_d}}\right)} \\ - \frac{\frac{d}{d\alpha_e} \frac{1}{2} P\left(r_o, \frac{1}{\sqrt{\alpha_e}}, \frac{1}{\sqrt{\alpha_d}}\right) * \frac{d}{dr_o} P\left(r_o, \frac{1}{\sqrt{\alpha_e}}, \frac{1}{\sqrt{\alpha_d}}\right)}{2 * \alpha_e^3 * P\left(r_o, \frac{1}{\sqrt{\alpha_e}}, \frac{1}{\sqrt{\alpha_d}}\right)^2} \end{array} \right\} * \left(\frac{1}{1 + \frac{2}{(\alpha_{tot,z} * X_{eff})^3}} \right) \quad 3.18$$

3.3 RESULTS AND DISCUSSION

3.3.1 Isotropic stiffness predictions

Five simulations were performed for each of the three scenarios presented in Table 3.2, which yields a summary of the predicted polymer backbone stiffness. The only exception was for the case of a lithium exchanged IPT with assumed HCP cluster packing. In this case, ten simulations were performed in order to get a clearer picture of the standard deviation in the results. The additional cases only marginally improved the standard deviation (from 1.35 to 1.27); however,

it was ultimately concluded that on a relative basis the standard deviation was acceptable. Among the fitting strategies mentioned in the last section, the diagonally weighted least-squares method (DWLS) of data fitting yielded the best Kolmogorov–Smirnov (KS) statistic (compared to the order of least squares, or OLS method). Therefore, the DWLS fitting was chosen for all presented analyses. Some examples of PDFs generated by this method are illustrated in Figure 3.5 and Figure 3.6, along with a normal distribution function in Figure 3.7.

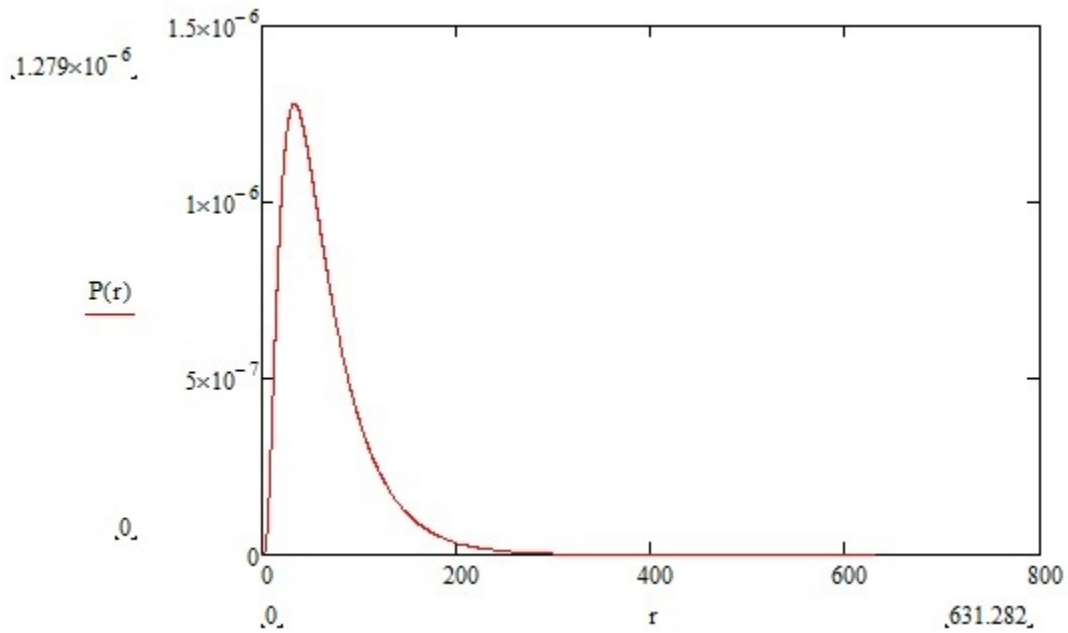


Figure 3.5: PDF of Na⁺-exchanged IPT with 15% uptake in EmI-Tf

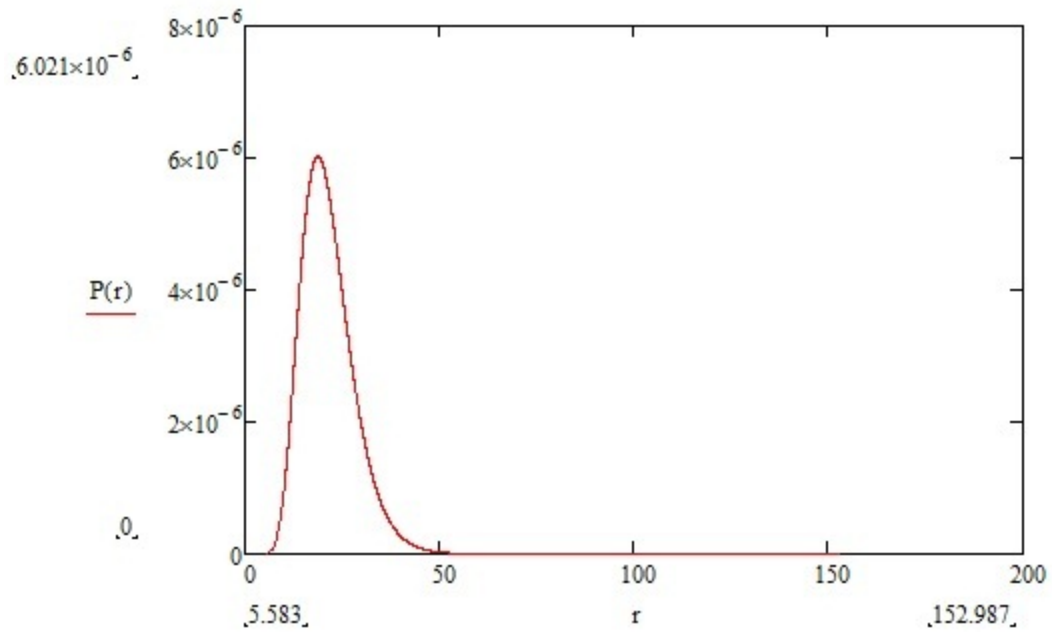


Figure 3.6: PDF of Li⁺-exchanged IPT with 38% water uptake

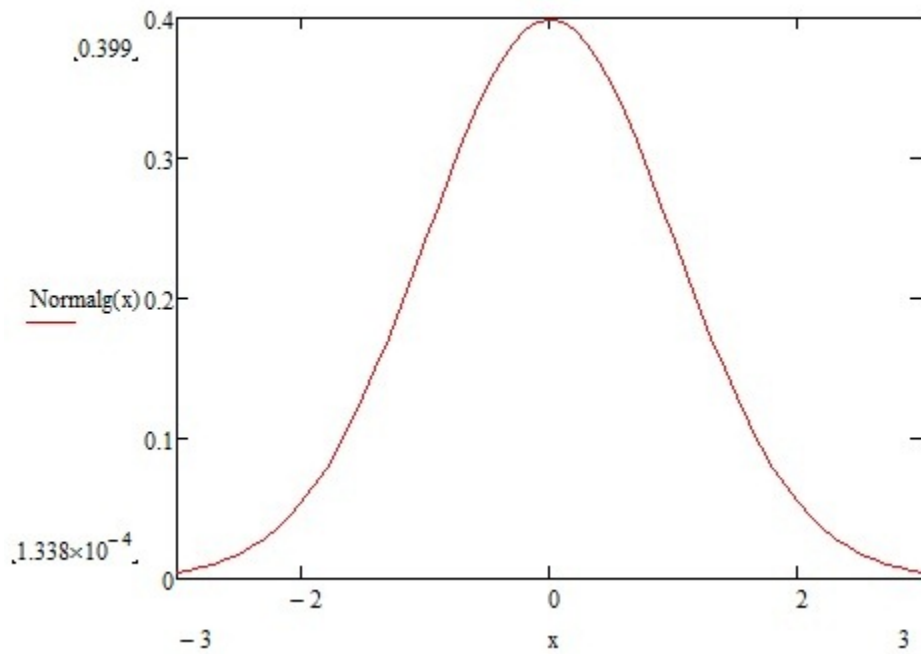


Figure 3.7: Example of a normal distribution curve

The main objective in showing Figures 3.5-3.7 is to illustrate not only the differences between the PDFs of two different scenarios, but also to show the difference between the PDF shapes with the normal distribution. These differences illustrate that a normal distribution cannot be fit to the data from these various cases of the IPT and that a PDF needs to be built in each of the various cases.

Table 3.2: Summary of isotropic model results where water is the diluent

Cation Type Cluster Volume Fraction	Li ⁺ : cubic		Li ⁺ : HCP	Na ⁺ (30%)		Na ⁺ (30%)
	10%	38%	38%	Cubic	HCP	Cyl
Young's Modulus (MPa)	13.3	9.5	15.1	5.8	10.7	5.24
Modulus Standard Deviation	0.8	0.4	1.27	0.3	0.05	0.9
KS statistic average	0.09	0.12	0.09	0.1	0.1	0.09

Recall that one purpose of multiscale modeling is to assess parameters that would otherwise be inaccessible via experiment. The results shown in Table 3.2 are valuable because experimentally, Li⁺ and Na⁺ exchanged IPTs vary in sensing response: these presented predictions (for the local, backbone stiffness) unlock the ability to investigate how the stiffness works at the local level and how this affects sensing at the local level. The latter will be considered ultimately in Section 3.4. First, it is important to consider from a purely mechanical domain the legitimacy of the predictions. For instance, looking at the results in Table 3.2, one sees a substantial difference in the stiffness between cubic packing and HCP arrangements. There is a significant difference as well between the fully hydrated and dehydrated lithium samples. Of these, consider first the implications of the assumed morphology. Inspection of this issue through the lens of classic packing density (P) of these cases may be instructive. This is generally defined as:

$$P = \frac{V_{atom}}{V_{cell}} \quad 3.19$$

where V_{atom} is the volume of an ‘atom’ (or in this case, the volume of a cluster) and V_{cell} is the volume of the representative volume element. For a body-centered cubic (bcc) lattice, $P = 68\%$ and for a HCP lattice, $P = 74\%$. This means that for the bcc lattice, 32% is left as free space for the polymer chains to conform, vs. 26% for the HCP. Intuitively, the HCP case is therefore more tortuous for the polymer chain conformation. In an attempt to further quantify this, consider the “effective energy” as follows:

$$\Delta U = -T\Delta S \quad 3.20$$

where T is temperature and S is expressed as

$$S(r) = k \ln(P(r)) \quad 3.21$$

ΔS is the change in entropy that can be expressed based upon an understanding of rubberlike elasticity[80] as:

$$\Delta S = \frac{V}{3}[S(r_o\alpha) + 2S(r_o\alpha^{-1/2}) - 3S(r_o)] \quad 3.22$$

Therefore, to evaluate Equation 3.20 with the values of root mean square (r_o) from Equation 3.2, the effective energy values are given in Table 3.3.

Table 3.3: Effective energy for morphology considerations

Case	Effective Energy (10^{-14} J)
NaHCP	1.6
Na Cubic	0.9
LiHCP	2.4
Li Cubic	1.6
Li Cubic(10%)	2.4
NaCyl	1.9

Because all systems tend toward low energy states, then for the cases considered and in the absence of strain hardening processing, the cubic morphology is more likely than the HCP or cylindrical morphologies.

Despite the absence of available experimental data to directly validate the local stiffness, it is prudent to critique the validity of the predictions presented in Table 3.2 against available data. A relatively simple approach employs the rule of mixtures to compare experimentally available global stiffness values as benchmarks. Using this tenet, the experimental stiffness of Nafion® can be expressed as [81]

$$E_{ave} = f_{cl}E_{cl} + f_{sc}E_{sc} + f_{bb}E_{bb} \quad 3.23$$

where f represents the volume fraction of the respective parts of the polymer and E represents the stiffness held by the respective moiety. The subscripts are as follows: ‘cl’ denotes clusters; ‘sc’ denotes semicrystalline regions and ‘bb’ denotes the backbone. The global, experimentally accessible stiffness is E_{ave} . The hydrated clusters do not support a tensile load, so E_{cl} is set equal

to zero. Depending on material synthesis, semicrystallinity can be varied between [1.8, 7.4]% (volume fraction percentage)[12]. This semicrystallinity stiffness is estimated to be 5000 MPa[82]. For the scenarios of this study this volume fraction becomes 2% for the fully hydrated lithium case. Because the volume fractions of semicrystallinity will shift with hydration, this value becomes 2.25% for the fully hydrated sodium case and 2.9% for the partially dehydrated lithium case (10%hydration).

Table 3.4: Comparison between model predictions and experiments

Case		Predicted E_{ave} (MPa)	Experimentally Reported E_{ave} (MPa)
Li ⁺ , 38% water		106	75-160 ^a
Na ⁺ , 30% water	Cubic	116	80-249 ^b
	HCP	119	
Li ⁺ , 10% water		158	220-390 ^c

^a[9,32,35], ^b[13,83,84], ^c[13,33]

Taking the fully hydrated lithium-exchanged case as an example, the cluster volume fraction is 38%. For 2% semicrystallinity this leaves a backbone volume fraction of 60%. Using the median backbone stiffness (E_{bb}) prediction of 9.5MPa in Equation 3.23, the global stiffness prediction (E_{ave}) of 106 MPa is obtained. This can be carried out similarly for the other cases as summarized in Table 3.4. A broad variation in experimentally reported global stiffness is also noted; this is related to variation in experimental methods, especially as it relates to control of hydration.

In discussing Table 3.4, it is pertinent to note the implications of the high stiffness of the semicrystalline regions. First, in the absence of this term the predicted backbone stiffness values may be perceived as too low (Table 3.2); however, when considered as one constituent alongside the semicrystalline regions the magnitudes of predicted backbone values are revealed to be

reasonable. Next, if validation of the backbone stiffness values had been attempted via direct comparison to available global stiffness data, the higher compliance of the sodium-exchanged case as compared to the lithium (38%) would appear incorrect. By introducing the rule-of-mixtures assessment a reversal for the global stiffness is also predicted; thus this reversal is physically plausible.

Further, while many Nafion experimental studies hydrate and ion exchange as-received samples, the more compliant hydrophobic backbone is expected to dominate deformation for uniform load distribution. To explore this expectation a comparison of the predicted stress-strain response as compared to experiment may be made if both are normalized with respect to stiffness. Kundu et al. have presented experimental stress-strain results for fuel cell membranes with a core of Nafion 112 (EW 1100). In this study of Nafion 112 a sodium ion exchange was performed as means to characterize the effect of this contaminant ion[9,12]. Figure 3.9 shows a comparison between the experimental study and the predictions of our model (when adapted to 1100EW) for the cubic case where the predicted stress values have been normalized with respect to modulus.

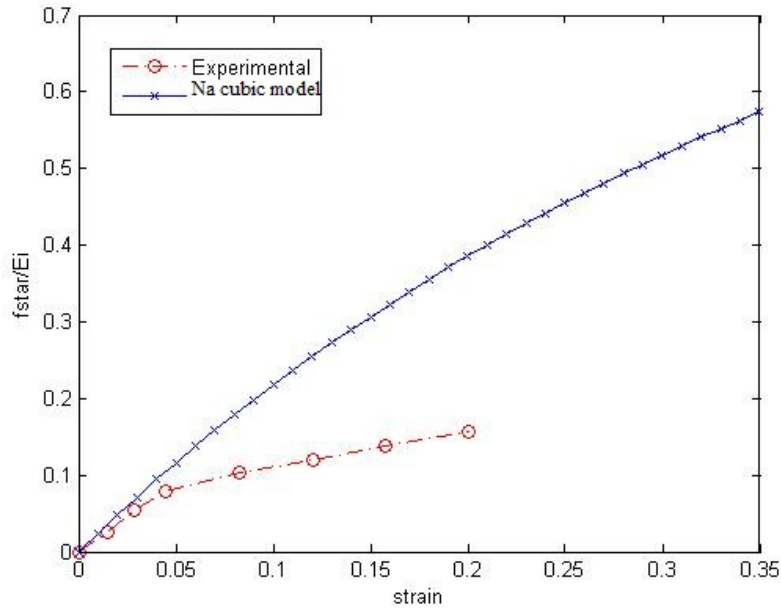


Figure 3.8: Experimental vs. model stress-strain curve for sodium cubic

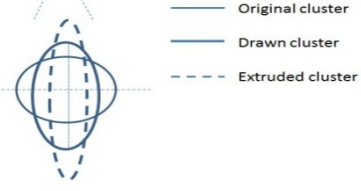
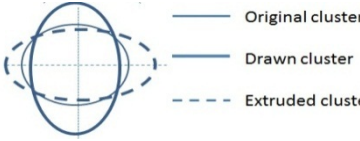
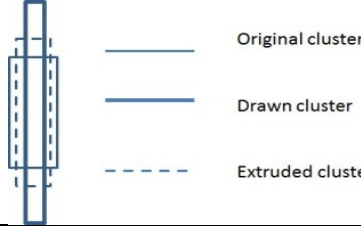
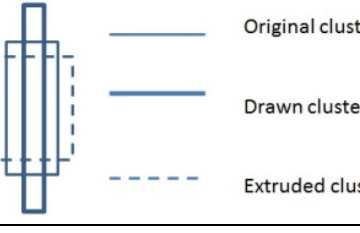
This shows that the model has reasonable predictive capability up to a few percent strain. This is to be expected for the assumption of affine deformation. Further, in both electromechanical and fuel cell applications, in-service strain is rarely expected above a few percent and thus this method should be reliable in the deformation range of interest.

3.3.2 Anisotropic stiffness predictions

The extent of Nafion anisotropy observed in the global stiffness (measured in macroscopic experiments) due to processing is modest. However, the effect is not necessarily modest in the context of morphology. Recalling that morphology plays a significant role in active response, while simultaneously being a function of stiffness, it is prudent to explore the algorithm's ability to detect directional variations in stiffness due to processing. Here, Sharaf's

approach to aligned or normal extrusion and drawing directions is considered as analogous to similar potential effects from machining and pressing.

Table 3.5: Anisotropic stiffness calculations in Cartesian directions

$\alpha_e = 1.1$	Per Figure 3.3 	Per Figure 3.3 
Direction	Modulus	Modulus
<u>Sphere</u>	$\delta = 1.1$	$\delta = 0.8$
x	13.0 MPa	22.5 MPa
y	13.0 MPa	22.0 MPa
z	13.6 MPa	20.8 MPa
		
<u>Cylinder</u>	$\delta = 1.3$	$\delta = 1.2$
x	12.6 MPa	31.5 MPa
y	12.6 MPa	26.0 MPa
z	18.3 MPa	33.0 MPa

In the absence of processing parameters, the values for δ (drawing ratio) and α_e (extrusion deformation) are chosen to be similar to the work of Sharaf [78]. When δ and α_e are applied in the same direction, onset of transverse isotropy is expected. This is the result noted in the first quadrant of Table 3.5. This is due to the polymer chains aligning themselves to move around the now elongated clusters and will align along the direction of the combined draw and extrusion. As there is symmetry between the x - and y - directions, there is no relative difference in the stiffness

values along these bearings. Similarly, when the model accounts for cylindrical clusters with a change in aspect ratio, $\delta \sim 1.3$, the predicted stiffness is 18.3 MPa in the z -direction and 12.6 MPa in the x - and y - directions. This is expected and similar to the model of Sharaf [78] and corresponding experimental results. While these experimental results took a different polymer (polystyrene), the idea of taking the spherical particles and applying heat in order to deform filler particles in ellipsoids is similar to the objectives here [76,84-86]. Moreover, the magnitudes predicted are the same order as those for the isotropic case and therefore assumed plausible per rule of mixture arguments. The new insight gleaned is that transverse isotropy becomes more pronounced for this higher aspect ratio case; this trend is expected but access to the predicted magnitude of the effect may become useful for sensing.

Next, when deformation in the clusters is imposed to follow Figure 3.3, the onset of anisotropy occurs in the reverse sense. That is, the z - direction stiffness lessens in favor of the x - and y - direction: further note that the stiffness lends itself to orthotropic behavior as expected as compared to the other cases because the ellipsoidal case has a larger cross-section in the x -than y - directions. Looking at the cylindrical case, the z -direction has a stiffness of 33.0 MPa and 31.5 MPa and 26.0 in the x - and y - directions respectively. This is expected in order to be in line with the conservation of the cluster volume.

3.4 INITIAL SENSING SIGNAL PREDICTIONS

This chapter began by postulating that local stiffness plays a significant role in IPT sensing. This section explores that postulate by implementing the predictions of the previous sections into an existing sensing model for IPTs in bending. While IPT sensing in shear is the ultimate focus of

this dissertation, it is prudent to first sanity-check the postulate for the comparatively well studied bending case. Recall from Section 2.3.3 that the streaming current can be calculated for a channel considering the charge density and velocity of the diluent flow. In the prior streaming current work where this equation was derived, the stiffness value that was the macroscopic IPT value, which was the only value available at that time. Because that model sought only to explore predictive *trends*, direct substitution of global stiffness was previously adequate. This work, however, seeks to advance the predictive capability, beyond simple trends, thus application of local parameters is sought.

3.4.1 Sensing for assumptions of isotropy

The predictions utilizing local properties begin with the predicted streaming current for an IPT in the bending case[65]

$$I_{tot} = \frac{3C}{2} \frac{v_f f_{cl} w \beta^2 a^2 \rho_e E}{\phi \mu L} \delta_f \quad 3.24$$

where C is described as a ‘dimensionless constant’. In the absence of empirical data for calibrating C , this is set equal to one. The other variables are as follows: v_{fis} the volume fraction of the electrode particulates, f_{cl} is the cluster volume fraction, w is the width of the IPT sample, β is a radius ratio, a is the diameter of an ionic channel, ρ_e is the charge density, E is the *local* modulus value, ϕ is a porosity value, μ is the diluent viscosity, L is the free length of the cantilever and δ_f is the deflection imposed on the IPT. The radius ratio β addresses the anticipated evolution of hydrophilic cluster/channel size in the blended electrode region, where the presence of metal particulate will affect the elastic energy balance. As detailed in [65] β is an estimate: based on Eshelby micromechanics arguments:

$$\beta = \frac{a_c}{a_{c,0\%}} \quad 3.25$$

where $a_{c,0\%}$ is the radius of the channel without any electrode particulate.

The porosity (ϕ) of the medium addresses evolving electrode-ionomer interface as the electrode architecture varies and is defined as[65]:

$$\phi = \frac{V_{void}}{V_{total}} \quad 3.26$$

It is important to re-iterate here that the modulus in Equation 3.24 is the *local* modulus, the results of which were calculated in Section 3.3.1. This is in contrast to the work of Gao and Weiland[63], which in the absence of any other available parameter assumed that E was the macroscopic modulus. Equation 3.24 for a fully hydrated, sodium exchanged IPT with 42% RuO₂ electrode particulate and assumed parallel channel morphology is then implemented with specific input parameters summarized in Table 3.6, with results illustrated in Figure 3.10. Note that the thickness term drops out because of an assumption that the ionic transport regions span the length of the thickness.

Table 3.6: For fully hydrated, 5 mm x 15 mm, Na⁺ exchanged IPT with 42% RuO₂ electrode particulate [65]

Electrode volume fraction (v_f)	0.42
Cluster volume fraction (f_{cl})	0.3
Width of IPT (w)	0.005 m
B	0.92
Channel diameter (a)	2.4e-9 m
Charge density (ρ_e)	3.8e7 C/m ³
Local polymer modulus, cylindrical (E)	5.24e7 Pa
Global polymer modulus[13] (E)	~8e7-9e7 Pa
Local polymer modulus, cubic (E)	5.8e6 Pa
Porosity (ϕ)	0.6

The values of Table 3.6 (with the exception of the E values) are taken from the work of Gao[65], where the variables are explained in detail as a function of electrode particulate volume fraction (v_f). Therefore, the v_f values dictate the values for β and ϕ . A graph of the predictions over a range of tip displacements is given in Figure 3.10. The values for the current calculated with the global modulus are extrapolated from the work of Gao and Weiland[63].

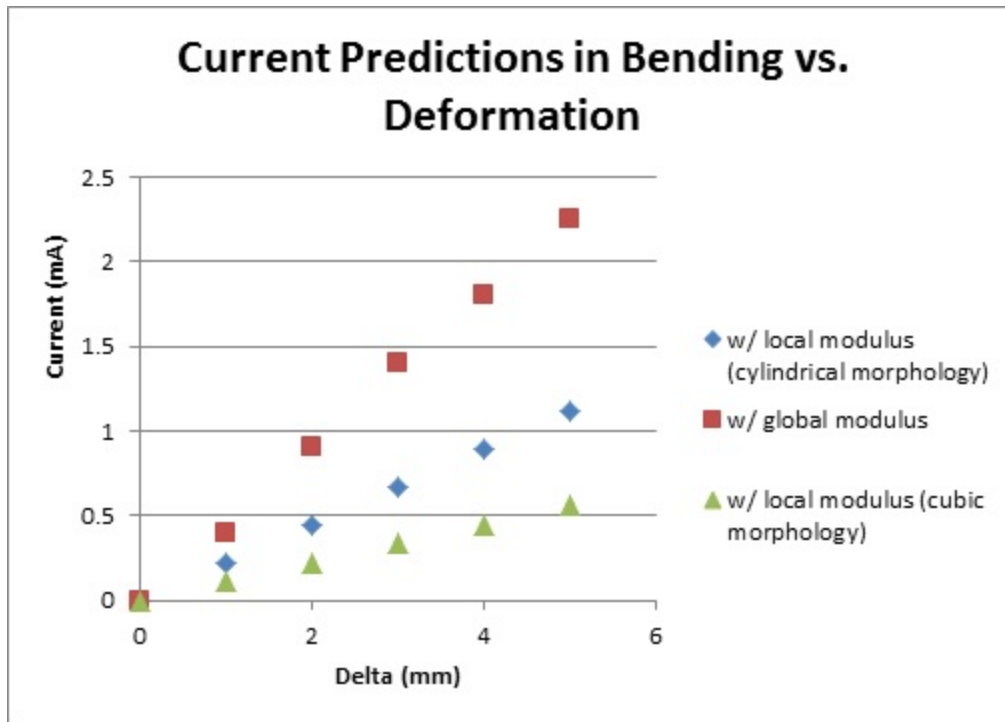


Figure 3.9: Predictions of the streaming current in bending with the local or global polymer modulus: sample type is sodium exchanged IPT with water as diluent

These results show that focusing on the local modulus; the current prediction is noticeably reduced. For example, Gao and Weiland noted specifically in their predictions that for a deflection of 2 mm, the current prediction is 0.9 mA, while they cite experimental work that indicates the deflection current should be more along the lines 0.1 mA[45,63]. When instead imposing local stiffness predicted when a cylindrical morphology was imposed, the current prediction is about 0.4 mA. This suggests that application of global stiffness may have been a significant source of error in the Gao and Weiland study. Also considered in Figure 3.10 is the substitution of the local stiffness when a cubic cluster morphology had been imposed *a priori*. Strictly speaking, this is somewhat at odds with the parallel assumption imposed on Equation 3.24, but yields insight into the implications of seemingly small predictive variations.

3.4.2 Effect of hydration level on sensing

Because the extent of diluent uptake is known to affect IPT transduction (Section 2.2.1), it is appropriate to explore this effect per the combined RIS/streaming current bending model. Because the relative effect of dehydration is of interest, a ratio approach is employed[37]:

$$\frac{I_{t,1}}{I_{t,2}} = \frac{v_{f,1} h_1^2 E_1}{v_{f,2} h_2^2 E_2} \quad 3.27$$

Here, $v_{f,i}$ represents the volume fraction of the hydrophilic regions for the respective case, E_i represents the *local* modulus for the respective case and h_i represents the cluster size. The expression here is developed by taking the ratios of I_{tot} as defined in Equation 3.24, for two cases that are identical except for hydration level. Each of these respective variable ratios, as well as the subsequent current predictions, are noted in the following table:

Table 3.7: Comparison of variable and streaming current values for different IPT scenarios

Cases (IPT ₁ /IPT ₂)	Volume fraction (v _{f,1} /v _{f,2})	Dimension (h ₁ ² / h ₂ ²)	Stiffness (E ₁ /E ₂)	Predicted Current (I _{t,1})/ (I _{t,2})	Experimental Current (I _{t,1})/ (I _{t,2})
Li ₃₈ %/Na ₃₀ %	1.28	1.14	1.64	2.3	5-10 [87]
Li ₃₈ %/Li ₁₀ %	3.8	3.2	0.71	8.6	6 [88]

The predicted ratio is smaller than that observed experimentally, but the trend direction of a stronger signal for Li₃₈% vs. Na₃₀% is still similar to experimental results.

With regard to the Li₃₈% case vs. the Li₁₀% case, there are reports that the sensing performs better in the dehydrated case[44,89]. However, both cited references noted are for sensing under

dynamic conditions, instead of the step modeling produced here. When considering a step input, measurements in terms of conductivity [88] are available, where it has been reported that the increased hydration gives a better conductivity by a factor of six. This trend matches well with the factor of 8.6 reached in Table 3.7. It is hypothesized that the water dynamics is the deciding factor in the differences between the reports given in references [44,88,89].

3.4.3 Sensing for assumptions of anisotropy

Since a goal of this work is to develop a robust model of the fundamental physics of these transducers, it is important to investigate how the streaming current generation is affected by manufacturing processes such as drawing. An initial look at how the current model will predict the changes in the streaming current due to such drawing affects shows promise.

In order to predict how drawing and extrusion affect the streaming current requires one modification to the modulus used in the streaming current prediction. The modification is that the modulus considered is now the local *directional* modulus. In the case of Equation 3.24, as an example, E_z is the value for the local modulus, specifically for the z -direction. What this enables, is a calculation of the directional output current, the numerical results of which are given in Appendix A.

A more insightful way to look at these results would be to investigate the ratios between the directional current values. However, noting in Equation 3.24, the only variable that would be different is the local directional modulus. In other words, in bending, to compare the currents in a given coordinate direction, it is necessary only needs to compare the moduli. The simplified relationship is

$$\frac{I_z}{I_x} = \frac{E_z}{E_x}$$

3.28

Looking in the literature to compare how such ratios of streaming current would compare to experimental results, the best available comparative base are conductivity studies of polymers that have been subjected to such processing methods. Lin et al. show a slight increase in relative conductivity given an increased draw ratio[77], which is in general agreement with the ratios of Equation 3.27 (the results of which are shown in Table 3.8). In addition, an earlier work by Cable et al. concluded that the ionic conductivity in the direction that is parallel to the stretching direction was 40% more than the conductivity in the perpendicular direction when subjected to a draw ratio of $\delta = 3.8$. In other words, the ratio is about 1.4[76], which is akin to the ratio of the z - and x -directions for (specifically the cylindrical morphology) as reported in Table 3.8. Also, to fully appreciate these values, additional 3D effects may ultimately need to be considered. However, the ratios comparing the streaming current between z - and x - directions for column 1 in Table 3.8, which correspond to the same loading conditions as the work by Cable[76], merit further investigation.

Table 3.8: Ratio of anisotropic current predictions in bending

Case	Ratio of Streaming current	Ratio of streaming current	Experiment
<u>Sphere</u>	Per Figure 3.3 $\delta = 3.8$	Per Figure 3.3 $\delta = 1.1$	
I_z/I_x	1.31	1.2	1.4*
	Per Figure in Table	Per Figure in Table	
<u>Cylinder</u>	$\delta = 3.8$	$\delta = 1.1$	
I_z/I_x	1.45	1.27	

*For this value from reference[76], clusters were illustrated as spheres. Experiments measured conductivity.

The predictions suggest that the seemingly modest variations in directional modulus, per the RIS methodology, may in fact play an important role in transduction and that the magnitude of the effect could be reasonable well predicted by these methods.

3.5 METHODOLOGY STRENGTHS AND WEAKNESSES

The primary strength of the multiscale modeling method presented in this chapter is the ability to predict the polymer backbone stiffness that is inaccessible via experiment. Further, the novelty of this method is that it can predict engineering changes to the material, such as drawing and extrusion, can have on the polymer backbone stiffness and how this in turn affects the material sensing behavior. A weakness in the method as presented here is that this it is a static model. That is, as the material is deformed by stress over time, the polymer backbone will undergo conformation changes that will in turn affect the stiffness.

3.6 CHAPTER SUMMARY

This chapter presented a statistical method to predict the local, polymer backbone modulus. This was based on the Mark-Curro approach to RIS theory. This chapter expanded on previous RIS studies to examine more cases of various ion-exchanged and hydrated Nafion® based IPT sensors. As demonstrated, this method is proved even more rigorous because of the ability of the method to detect directional stiffness values at the local level. Further, by considering the local stiffness values in terms of the streaming current predictions for bending mode, a noticeable

improvement in the predictions is demonstrated. There was also a consideration of how the polymer chain alignment can affect the streaming current when subjected to anisotropic processing methods. While the literature can only offer, to the best of the author's knowledge, information on conductivity, the trends between the anisotropic predictions and the experimental results for conductivity measurements is promising. With this understanding of how the polymer chains can be modeled, the focus shifts to modeling how the diluent flow affects the streaming current development.

4.0 SHEAR MODEL

In this chapter, a computational model for the prediction of IPT sensing in response to shear deformation is presented. To mitigate complexity, this study will utilize local, *isotropic* stiffness predictions from the previous chapter. It is postulated that the streaming potential hypothesis has the capacity to accommodate all modes of IPT sensing, while prediction of sensing in shear has been elusive per the current state of the art. Per the previous chapter, model development is alert to multi-scale phenomena. A conceptual rendering of the evolution of a streaming potential is given in Figure 4.1

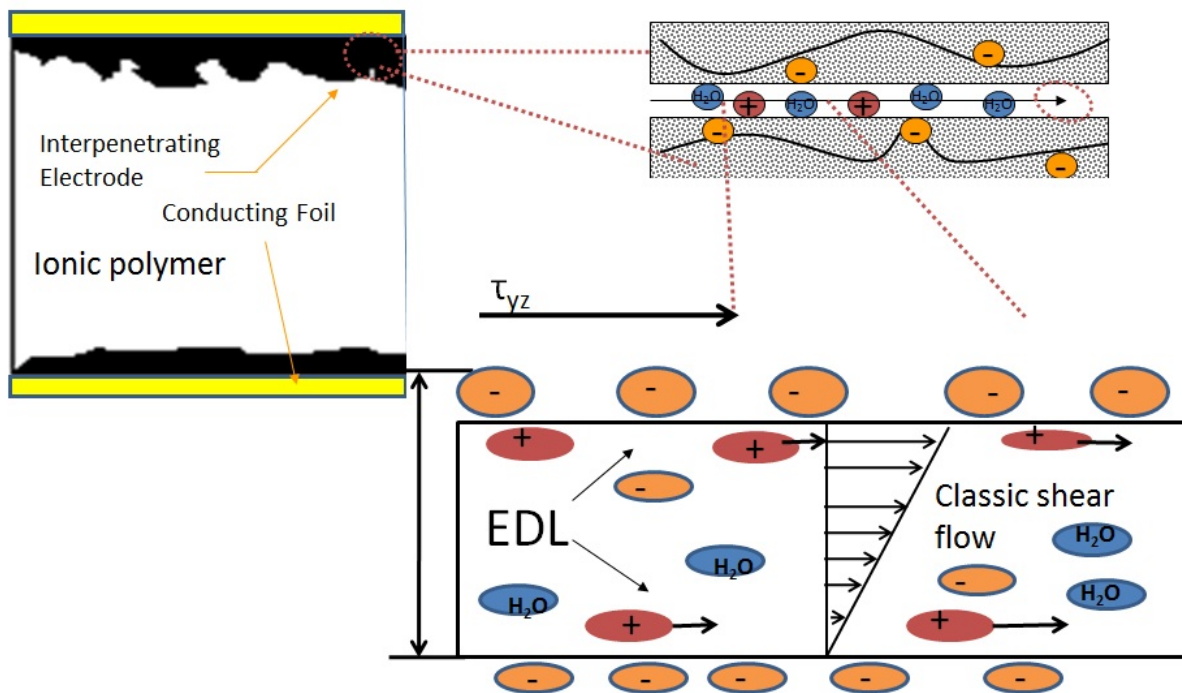


Figure 4.1: Streaming potential response to shear deformation

Recall that the streaming potential hypothesis argues that unpaired ions exist in the diluent; that is, an electrolyte exists in the hydrophilic region of the ionomer. This diluent comes into contact with the embedded electrode, where an electric double layer (EDL) has formed, also as a result of phase separation. It is then argued that for any IPT deformation the EDL will be disrupted by diluent flow and a streaming potential will evolve. The strengths of this hypothesis include: (i) while the magnitude of the predicted streaming potential and current will vary with assumed morphology, its existence can be argued for any morphology and (ii) while closed, analytical solution is in some cases elusive, the hypothesis is able to predict the existence of a sensing response under any deformation, including shear loading.

Recall also that the morphology of the ionic transport regions plays a role in the sensing response of IPTs. Of the modes of IPT deformation known to display a sensing signal, the pure shear mode is arguably the most difficult to isolate, both theoretically and experimentally. In the case of modeling, the complete absence of a hydrostatic component of loading complicates strategies for estimating the nature of diluent flow, where this flow is the very impetus for EDL disruption and subsequent evolution of the streaming potential. Because a closed form solution of flow along a constrained path due to shear load is elusive, a finite element approach is employed.

In addition, streaming potential models to date, in addition to being largely focused on sensing in bending, have also assumed idealized, perfectly aligned diluent channels. In reality, irrespective of actual morphology, the orientation of diluent flow paths within the electrode region will necessarily be random. To explore the implications of imperfect flow path alignment, varied path orientations are considered. Further, as the computational models are only as good as the programs used to implement them; two different modeling scenarios will be considered. First, a ‘single body’ model will look at the response of the diluent when the shear stress is applied directly to the fluid. Second, a ‘two body’ model will look at the response of the diluent when the shear stress is applied to a thin material layer, which in turn creates shear forces on the diluent. Using the observed trends in predicted flow for different path orientations with respect to load, a volume averaging scheme is imposed to predict IPT current evolution; both transient and steady state results are provided.

4.1 'SINGLE BODY' MODEL DEVELOPMENT

4.1.1 Bio-inspired approach to modeling shear induced flow

Review of past precedents in assessing shear induced flow within a compliant channel unveils similarities between IPT pathways and blood vessels. For example, it has been observed that IPTs swell with change in hydration levels and this swelling has an effect on the morphology of the material[17,90], which is similar to the behavior of blood vessels. Also, it is postulated that the morphology in Nafion® is irregular, with channels branching and reaching dead-ends[83]and are most likely of complex shape. Again, this is similar to how medical scientists understand blood vessels. Even so, biomechanical studies have argued that a cylindrical approximation is a reasonable simplifying assumption[91]. This work similarly adopts the simplifying assumption that the hydrophilic region can be approximated as a collection of 'channels'. In the case of the IPT, deformation induces fluid flow and subsequently disruption of the EDLs within this collection of channels. Another blood vessel analog is adopted when it is next considered that prediction of shear induced flow is the goal here. In the case of blood flow it has been reported that velocity gradients arise from frictional forces between layers of fluid and also between the fluid and the vessel walls. The wall shear stress within blood vessels has subsequently been studied because it has implications for the development of certain diseases. It is further understood within the medical field that there is a shear stress threshold that is required to initiate blood flow in a vessel [92].

In order to develop a velocity within the microchannel, an estimate for the wall shear stress value must be imposed. It is assumed here that the channel walls are nonporous (solid). To estimate a relationship between shear load on the IPT and the shear load seen by the walls of the

channels, the Voigt approach is applied. In this approach, the strain is the same in all elements of the model. A proportional relationship between the global strain and strain in one channel is incorporated into this relationship, yielding:

$$\tau(E, \gamma) = \frac{E}{2(1+\nu)} \frac{\gamma l}{b} \quad 4.1$$

Here, τ is the shear stress seen by one IPT channel perfectly aligned with the external shear load, γ is the global strain seen by the entire IPT, l is the length of one microchannel and b is the length of the entire IPT. The value of l is described by some experimental work as being “tens of nanometers” [24]. Further, given that there are most likely tortuous regions[36], this estimate is deemed reasonable and l is set equal to ninety nanometers and is noted in Table 4.1. It is important to note here that the Young’s modulus that is used to obtain the shear modulus is not the global, averaged Young’s modulus of the IPT or even of the Nafion® layer; instead it is argued that the local shear modulus is the key parameter. In the results presented in this section, the modulus is chosen according to the spherical morphology with rectangular packaging. While there are still channels connecting the spherical cluster regions, this stiffness is chosen going forward because the energy of a spherical versus pure cylindrical morphology, the spherical arrangement of the hydrophilic clusters is lower. Because global stiffness also includes volume averaged contributions from semi-crystalline inclusions and non-load-bearing hydrophilic clusters the local moduli are expected to vary significantly within the material. Here it is assumed that the walls of the channel are locally dominated by the amorphous hydrophobic backbone[25]. For the Poisson’s ratio, the material is assumed to be incompressible, thus $\nu = 0.5$.

Consider next that this study aims to explore the evolution of streaming current for a collection of randomly oriented channels within a three-dimensional (3D) space, as it is

unrealistic to assume that all flow pathways are perfectly aligned with the direction of shear loading. This is investigated by rotation around Cartesian axes, as is illustrated in Figure 4.2.

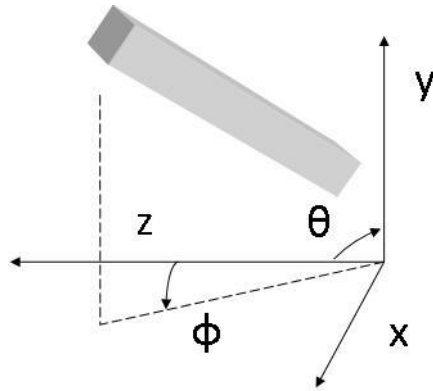


Figure 4.2: Rotation of IPT microchannel by θ around the x -axis and/or by ϕ around the y -axis

The approach employed here begins by considering the evolution of streaming current for single channels oriented with discrete rotations about the x and y axes with respect to shear loading. The subsequent predictions are then used to estimate a surface representing the streaming current for a collection of channels that are randomly oriented in θ and/or ϕ directions.

4.1.2 Geometric dimensions

The commercial finite element package ANSYS version 12.0 has been used for an IPT microchannel. For simplicity, a rectangular shape channel is assumed. The geometry was built in ANSYS Design Modeler version 12.0.1, with meshes investigated within ANSYS Meshing, also v. 12.0.1. Tetrahedrons were used for the cell type, with the verification detailed in a later

section. Surfaces are placed at the midsection of the channels in order to inspect the velocity profile at the midpoint of the channels.

Table 4.1: Channel dimensions and orientations

Length (nm)	90
Cross-sectional area (nm ²)	5.76
θ (radians)	0, $\pi/4$ or $\pi/2$
φ (radians)	0, $\pi/4$, $\pi/3$ or $\pi/2$

Channel dimensions in Table 4.1 are adapted to the rectangular shape, but based on the sizes argued for the parallel channel morphology proposed by Schmidt-Rohr and Chen[24]. The cross-sectional area is based on a rectangle side of 2.4 nm (also from Schmidt-Rohr and Chen). It is further important to note that the length of a channel side range proposed by these authors will yield an overlapped EDL throughout the range of proposed values.

Two mesh configurations were considered. The first configuration assumed that the shear stress imposed on the channel would be imposed directly onto the diluent itself. The second approach consideration considered a second part within the mesh as the wall. Further details on these mesh choices are given in the following sections.

4.1.3 Force application

Channels aligned parallel to shear loading are necessarily subject to significant distortion along the fluid flow direction. With the channels inclined at an angle, the shear pressure applied

to the channel walls is reduced. To implement the model, first the shear pressure is calculated via Equation 4.1 for an imposed global strain. Second, this value is applied to the walls of a single channel via the following illustration and tabular summary.

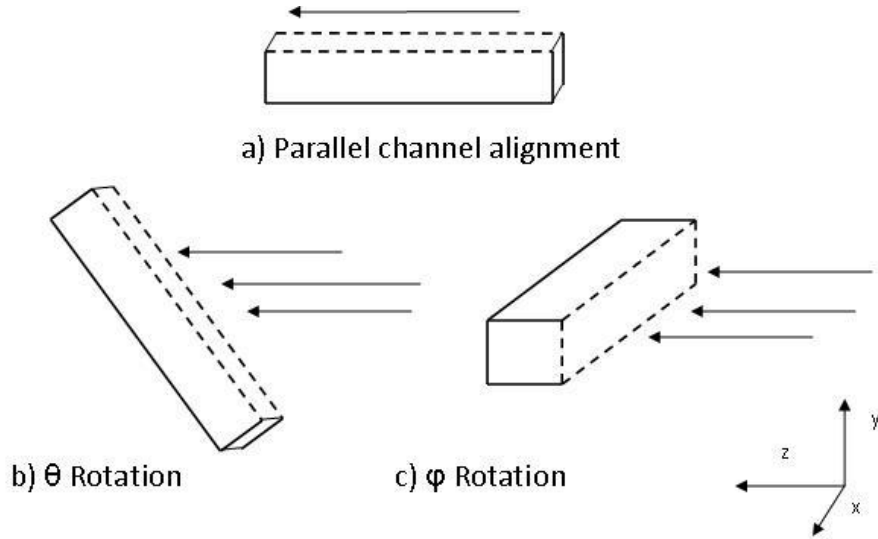


Figure 4.3: Boundary conditions for channel morphology

Table 4.2: Wall boundary conditions

Wall Location	Boundary Condition
—————	Moving wall, no slip or shear, θ_m, γ_w
- - - - -	UDF: τ θ_m, γ_w

In Table 4.2, the θ_m value is an estimate on the contact angle between the fluid and channel wall and is a factor in the surface tension force calculations. Specifically the contact angle governs the curvature of the liquid in relation to the channel walls:

$$\kappa = \nabla \cdot (\hat{n} \cos(\theta_m) + \hat{t} \sin(\theta_m)) \quad 4.2$$

where n and t are the normal and tangential unit vectors respectively with respect to the channel walls. The surface tension (γ_w) is included in the momentum equations via:

$$\mathbf{P}_{st} = \gamma_w * (2\kappa) \quad 4.3$$

The numerical value for the contact angle (θ_m) is taken from the review of van Honschoten et al. [88], calculated via

$$\theta_m \approx \frac{\theta_\infty}{2(2 - \cos(\theta_\infty) - \cos^2(\theta_\infty))} \quad 4.4$$

where θ_m is the macroscopic contact angle. The boundary conditions noted in Table 4.2 are necessary for defining a tractable problem but are also simplified assumptions, for two reasons. First, making a continuum assumption of no-slip behavior at this length is most likely not realistic[93]. Second, the contact angle imposed is that for the given diluent with respect to Teflon® walls which is, at best, an estimate of the microscopic contact angle. This is an assumption of necessity because definitions of how this contact angle may change at this length scale are still in development[94].

With these considerations, the momentum equation used by ANSYS is as follows:

$$\frac{\partial}{\partial t}(\rho\vec{v}) + \nabla \cdot (\rho\vec{v}\vec{v}) = \mathbf{P}_{st} + \tau(E, \gamma) + l(\nabla \cdot (\bar{\tau} - \nabla p)) \quad 4.5$$

The forces on the right-hand side of Equation 4.5 include the surface tension (represented by Equation 4.3). This necessarily opposes the shear pressure applied to the channel wall (τ) given in Equation 4.1. Also, consideration is given to the friction associated with the fluid viscosity (noted by $\bar{\tau}$). It is important to note here that the dynamic pressure (∇p) is dependent on the velocity and density of the fluid and will therefore evolve in response to other terms in Equation 4.5. The final boundary condition to consider is the inlet and outlet conditions. The outlet boundary condition was set to a zero-pressure inlet. For this ‘one body problem’, the inlet boundary condition was a very small velocity inlet value.

4.1.4 Mesh Verification

Several simulations have been conducted in order to verify the proper mesh with which to proceed with calculations. The results of these trials are noted in Table 4.3. The mesh images are listed in Appendix B. The angles of rotation are for the mesh consideration when the shear stress is imposed directly onto the diluent. The two-body mesh optimum specifications are also noted as follows.

Table 4.3: Optimum mesh specifications for channel rotation

Angle of Rotation (radians)	Direction	Average Skewness	Nodes	Elements
0	θ	0.23	5 634	24 534
	φ	0.23	5 634	24 534
$\pi/4$	θ	0.21	6 767	31 160
	φ	0.29	5 984	28 298
$\pi/3$	θ	----	-----	-----
	φ	0.38	758	2 459
$\pi/2$	θ	2.6×10^{-4}	3 009	12 284
	φ	0.21	17 206	85 154
2-Body mesh	-	0.2	21003	97 643

The purpose of considering different orientations is to enable the creation of a volume averaging strategy. In the case of rotations in θ a trend became evident with the three noted orientations, while an extra case was deemed necessary for rotations in φ ; thus the extra case of $\pi/3$ in the φ direction is offered. Re-verification of the mesh at different angle values is necessary because the mesh is deformed with the rotation of the channels. Therefore, it is necessary to find the optimum mesh specifications in each direction to ensure that the mesh captures the converged flow patterns.

4.2 ‘TWO BODY’ MODEL DEVELOPMENT

The two-body model is an ANSYS® model with a second layer of material over the diluent. In this case, this second layer (meant to represent the polymer) receives the shearing stress directly and then transfers this stress onto the diluent. This is in contrast to the one-body model where the stress is applied directly to the diluent. Here, the two-body model is considered with a Li⁺ exchanged, EmI-Tf saturated Nafion® base. The model input parameters with these considerations are given as follows:

Table 4.4: EmI-Tf model input parameters

EmI-Tf Viscosity[1]	45 x 10 ⁻³ Pa*s	EmI-Tf Density[1]	1387 kg/m ³
Local modulus	5.5 MPa	Electrode thickness	0.194 mm
IPT width	15 mm	IPT length	50 mm
Channel width	2.4 nm	Channel length	90 nm
Surface Tension (γ)[95]	0.03831 N/m	Contact Angle (θ _m)[94,96]	34°

Similar to the one-body model, the local Young’s modulus was established via a RIS theory model, with assumed cubic packing, spherical morphology. The IPT width, length and electrode thickness are based upon IPTs built in recent studies [97]. The results from the RIS model predictions are given in Table 4.5. The ionic liquid volume fraction uptake into the polymer was modeled according to the experimental measurements taken by Akle, et al. [1]. The procedure for obtaining these stiffness values was outlined in Chapter 3.0 of this dissertation.

Table 4.5: EmI-Tf RIS stiffness results

Cation Type	Li ⁺ : cubic
Ionic Liquid volume fraction uptake	58%
Young's Modulus (MPa)	5.5
Modulus Standard Deviation	0.3
KS statistic average	0.09

The electrode thickness and the IPT width were chosen to match the experimental component of Kocer et al. [98]. Here, the authors built IPTs with similar dimensions and carried out shear sensing experiments. Further in Table 4.4, the surface tension was chosen for a similar ionic liquid to EmI-Tf. Finally, the contact angle for the channel walls and the electrolyte was chosen as the equilibrium contact angle from the work of Stalcup et al. However, given the size of the channels, a more reasonable estimate was calculated using the equation for the microscopic contact angle estimated in the work of van Hoschten et al., as shown in Section 4.1.3. The mesh refinement values are given within Table 4.3 and the method follows in a similar fashion as was described for the ‘one body model’ in the previous sections.

In this particular model, it was desired to look at how the streaming current developed over different strain values (vs. just the ‘one body model’, where only one strain value was considered). The shear stress is calculated for various strain values as given in the following table and according to Equation 4.1.

Table 4.6: Shear strain, deflection and stress calculations for lithium-exchanged IPT of length = 50 mm

γ	δ (μm)	τ (Pa)
0	0	0
0.00025	0.05	0.00083
0.04	7.8	0.132
0.07	13.6	0.231

The deflection values in Table 4.6 are calculated via simple shear, so:

$$\delta = \gamma t \quad 4.6$$

where t is the thickness of the IPT *electrode layers* (not the entire IPT thickness), δ is the actual deflection imposed for a specific shear value (γ). The goal here would be to stay in the linear elastic regime. There are two concerns: (i) to stay within the linear elastic regime at the macro-level and (ii) staying in the linear elastic regime at the micro-level. By ensuring $\delta \ll 1$, concern (i) is addressed. However, this does not say anything about concern (ii). The macroscopic deformation could potentially create nonlinear deformations on the microscale. While an in depth response to this question should involve an investigation of linear micromechanics (such as equivalent continuum methods[99]), a general defense of our final displacement range for the micro regime would be to keep the strain imposed on the sample to be: $\gamma \sim 0.1$. This is based on the initial comparison between our models and the macroscopic behavior[39]. Also, a key fact to distinguish about Table 4.6 is that the shear stress is dependent on the type of ion-exchanged polymer under consideration.

The final boundary condition to consider is the inlet and outlet conditions. The outlet boundary condition was set to a zero-pressure inlet. For this ‘two body problem’, the inlet boundary condition is set to zero-pressure.

4.3 RESULTS AND DISCUSSION

4.3.1 Analysis of one-body model

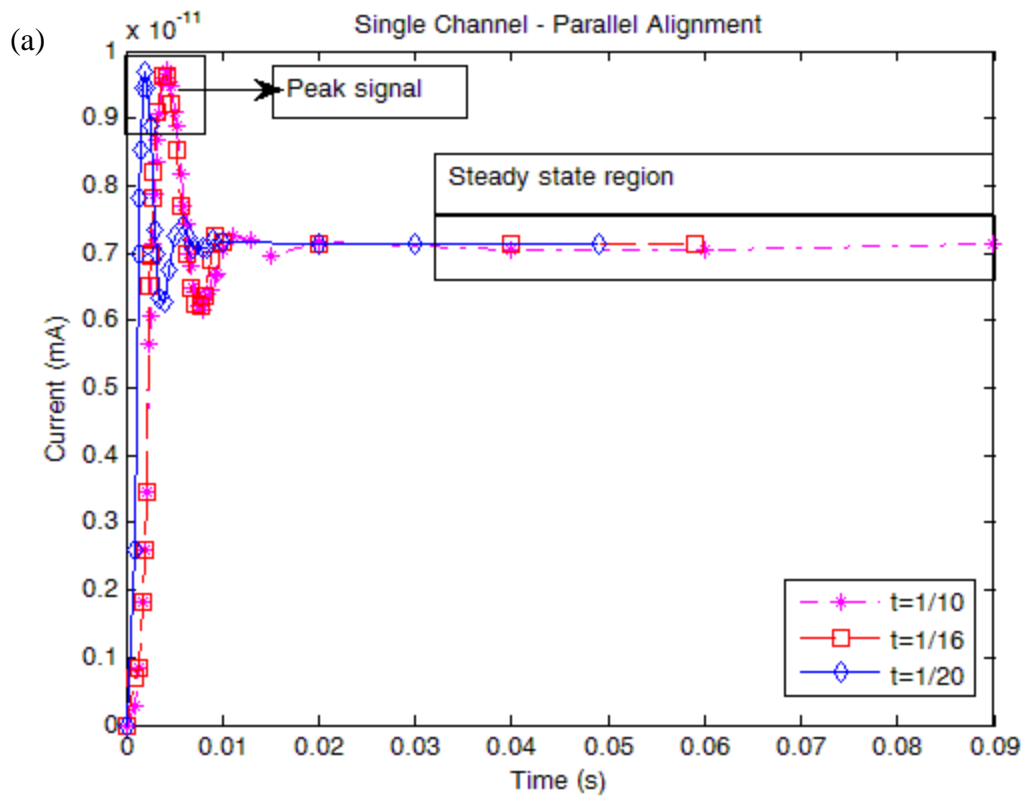
Recall that the objective of this section is to investigate how the possible channel orientations affect the development of the streaming current within the IPT. Therefore, in this case, water was considered as the diluent for a single deformation value.

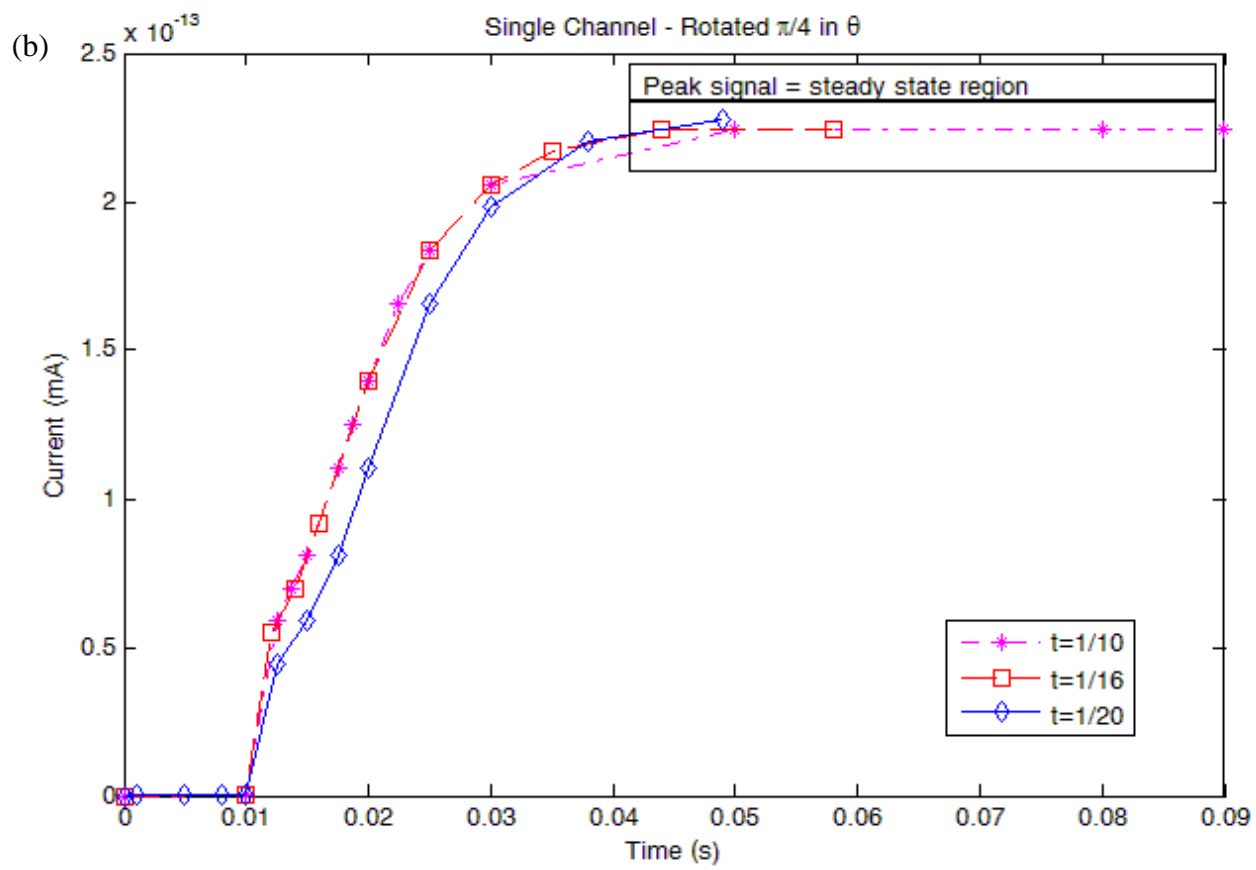
Gao and Weiland have previously argued that the EDLs of the opposite channel walls are expected to overlap, and subsequently the diluent may be treated as a unipolar solution[63]. The parallel channel model proposed by Schmidt-Rohr and Chen argues a particularly large channel size[24]. Thus the validity of the unipolar solution assumption can only improve for alternative assumed morphologies. The streaming current can be expressed as follows.

$$I_{st} = \rho_e w \int_0^{2h} \vec{v} dy \quad 4.7$$

Here, I_{st} is the streaming current expected for an individual microchannel, ρ_e is the charge density, w is the width of the channel, dy is the height of the channel mid-section piece and v is the velocity of the diluent within the microchannel as determined by ANSYS.

The results of this computation are shown for water diluent and for the loading rates noted in Figure 4.4: (a-c).





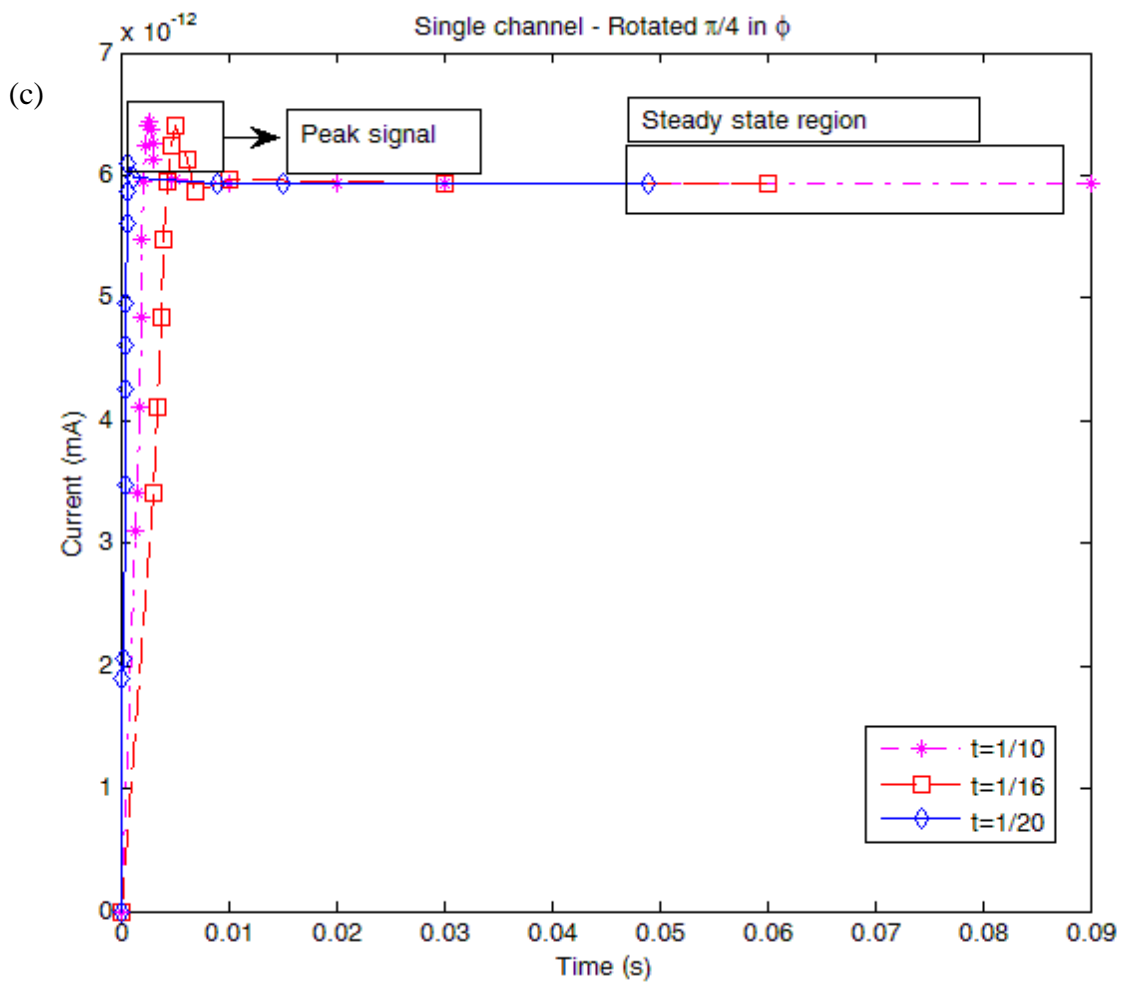


Figure 4.4: Li⁺ exchanged, 38% water hydration, streaming current prediction responses for a single channel (a) Aligned parallel to load (b) Rotated in θ to load (c) Rotated in ϕ to load. Steady state current values are given in Table 4.7

The steady-state current values were taken from Figure 4.4 (a-c) and are tabulated as follows.

Table 4.7: Steady state streaming current for a single channel (From Figure 4.4(a-c)). Please refer to Figure 4.2 for θ and ϕ reference

Angle (radians)	Time (s)	Current (mA) for θ	Current (mA) for ϕ
0	1/20	7.2×10^{-12}	7.2×10^{-12}
	1/16	7.1×10^{-12}	7.1×10^{-12}
	1/10	7.1×10^{-12}	7.1×10^{-12}
$\pi/4$	1/20	2.2×10^{-16}	5.9×10^{-12}
	1/16	2.3×10^{-16}	5.9×10^{-12}
	1/10	2.3×10^{-16}	5.9×10^{-12}
$\pi/3$	1/20	Not calculated	2.25×10^{-12}
	1/16	Not calculated	2.25×10^{-12}
	1/10	Not calculated	2.25×10^{-12}
$\pi/2$	1/20	4.3×10^{-20}	5.3×10^{-22}
	1/16	4.3×10^{-20}	5.3×10^{-22}
	1/10	1.8×10^{-18}	5.3×10^{-22}

It is pertinent to note that the values reported in Table 4.7 are those from the steady state regions as illustrated in Figure 4.4 (a-c). Results were not calculated for the $\theta = \pi/3$ as they were not necessary for curve-fitting purposes.

Next, a differentiation must be made between transient and steady state response. Near alignment with load results in the prediction of transient extrema followed by a steady state response (that is, steady over the length of the simulation). This transient region develops a peak for the parallel channel case in Figure 4.4 (a). The existence of these extreme is a function of channel orientation with respect to load as illustrated in Figure 4.4(b) and Figure 4.4(c). As alignment degrades not only do the total magnitudes diminish - more or less as expected, but in addition the transient response is predicted to disappear entirely as is seen for example in Figure 4.4(b). While only a small proportion of actual flow pathways can be expected to be in alignment

with loading, because the magnitude of the signal is large these transient peaks may be apparent in the overall IPT signal.

4.3.2 Analysis of the effects of channel orientation on streaming current

It is prudent to next consider how the predicted streaming current degrades with orientation as a first step toward imposing a volume averaging scheme. Because a steady state region is observed for all orientations, evolution of the steady state signal with orientation will be considered first.

For microchannel rotation in the direction of θ about the x -axis (please refer to Figure 4.2), a curve may be fit to the diminishing steady state streaming current predicted with increasing rotation. The evolution with respect to θ in radians can be estimated by

$$I(\theta) = I_{max}e^{-9\theta} \quad 4.8$$

where I_{max} here is steady state for the perfectly aligned case (7.2×10^{-12} mA). A similar procedure is invoked for curve fitting the diminishing streaming current with increasing rotation about the y -axis, yielding

$$I(\phi) = -4.55 \times 10^{-12}\phi - I_{max} \quad 4.9$$

where I_{max} is 7.2×10^{-12} mA (again for the perfectly aligned case) and ϕ is again measured in radians. Here, a linear rather than an exponential decay is predicted. Finally, it is assumed that the trends between these two cases, that is rotations about the x - and y -axes, evolve smoothly for intermediate rotations through the z -axis; Equation 4.8 can be combined with Equation 4.9 to obtain the sought three dimensional model. Multiplying and normalizing with respect to I_{max} yields:

$$I(\theta, \phi) = I_{max}(e^{-9\theta})(-0.639\phi + 1) \quad 4.10$$

A visualization of Equation 4.10 is shown in the following figure:

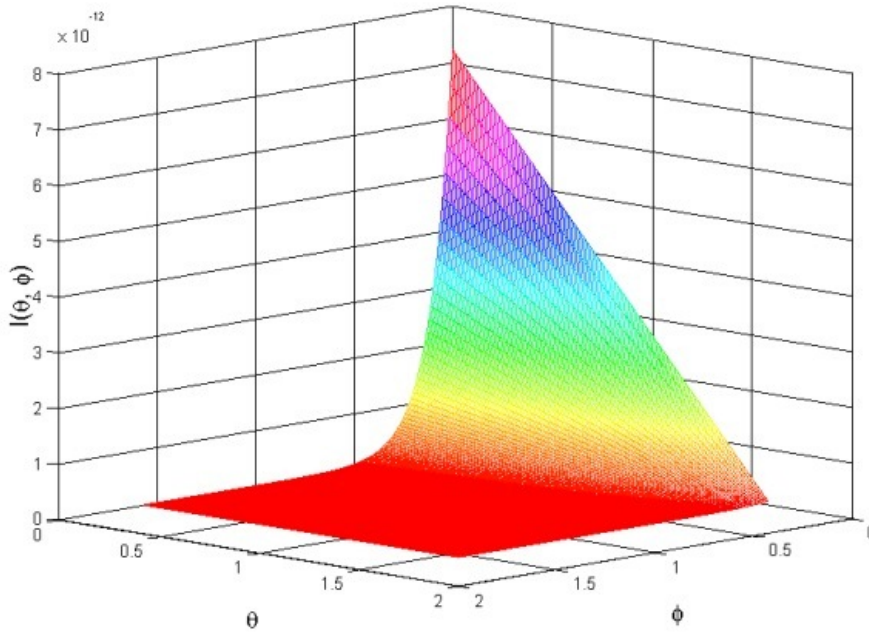


Figure 4.5: Streaming current in a single channel as a function of angle rotation with respect to external shear load

An evaluation of Figure 4.5 indicates a few trends. First, it shows the intuitive result that the streaming current is at a maximum when a microchannel is aligned perfectly parallel with the loading direction. Also, that the streaming current approaches fundamentally zero as θ and ϕ approach $\pi/2$. While the figure illustrates only one octant of three dimensional space, symmetry arguments are intuitive. Since the model developed in this work was built over the range $[0, \pi/2]$, it is desirable to create a projection of the streaming current over a small volume, that is, over 2π for the response modeled in Equation 4.10. This response is integrated over this range and normalized according to:

$$Q = \frac{\iint_0^{\pi/2} I(\theta, \phi) d\theta d\phi}{\iint_0^{\pi/2} d\theta d\phi} \quad 4.11$$

Next, in order to estimate the total streaming current from an IPT with randomly oriented channels, it is necessary to consider the total number of channels in communication with the electrodes. This can be estimated using a direct volume fraction approach[37]. Assuming equal probability of any channel orientation in 3D space the net IPT signal can be estimated by multiplying the number of channels by the volume average of Equation 4.11. Therefore the IPT total streaming current can be estimated by:

$$I_{tot} = Q * \frac{v_f f_{cl} h w b}{V_{ch}} \quad 4.12$$

where variables in Equation 4.12 are defined in Table 4.8. These values conform to the IPTs considered in references[1,15].

Table 4.8: Input values and result for Equation 4.12

Physical Meaning	Variable	Value
Volume fraction of electrodes	v_f	0.2
Volume fraction of channels	f_{cl}	0.3
Depth reached by electrodes into an IPT	h	9.4 μm
Width of macro IPT	w	5 mm
Length of macro IPT	b	15 mm
Total estimated streaming current	I_{tot}	20.5 μA

The resulting prediction of 20.5 μA (steady state) is about 95 times lower than that predicted for a system of perfectly aligned channels. Thus, flow path orientation is clearly a significant consideration for shear loading. These results, however, are not yet comparable to previously reported experimental results. Rather, experimental results consider transient signals, and further, are reported in terms of sensitivity; see for example[55]. Therefore, the next steps in this analysis are to incorporate consideration of the transient signal shown in Figure 4.4(a-c), both before the peak signal and just after, as well as to correlate results to sensitivity reports.

The results noted in Table 4.8 and in Figure 4.4(a-c) represent the streaming current (μA) in the time domain, whereas the published experimental results in literature are sensitivity ($\mu\text{C}/\varepsilon$) in the frequency domain[55]. In order to obtain a proper comparison of the data, the predicted values shown in Figure 4.4(a-c) are transformed to the frequency domain via a Fourier transform:

$$I(f) = \int_{-\infty}^{\infty} I(t) * e^{-j2\pi ft} dt \quad 4.13$$

Equation 4.13 is evaluated using the discrete Fourier transform in MatLab®, utilizing the current predictions for an IPT with perfectly aligned channels. In the first step to evaluate Equation 4.13, the data points from Table 4.7 are reduced by $95\times$ (according to the discussion immediately following Table 4.8). Next, these values are evaluated according to Equation 4.13 which enables a direct comparison to experimental data. These results are plotted in Figure 4.6. The experimental results within this figure are visually approximated and extrapolated from[55].

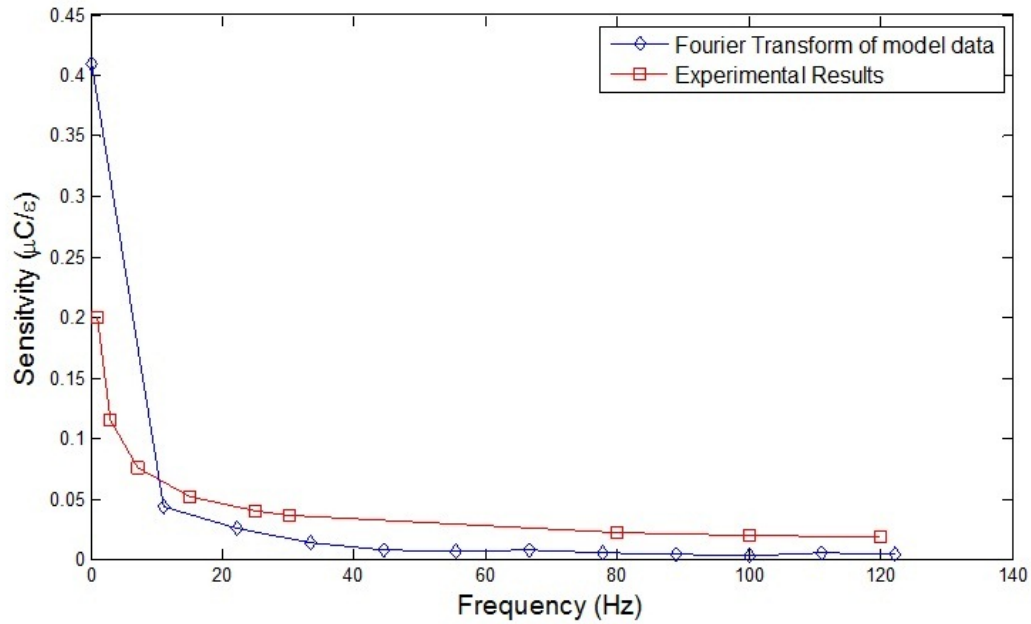


Figure 4.6: Fourier transform of model results vs. experimental results

The results in Figure 4.6 are encouraging because the predicted trend for charge output is quite similar to the experimental results. The difference in the initial sensitivity between the model and the experiments may be attributed to the use of IPT-securing Kapton tape in the shear test experimental method as noted in the report[55]. It could also be that the $95\times$ factor from the steady state assessment is inexact, especially when imposed on a transient response. Further examination of the transient response of the model given in Equation 4.10 will be warranted as recommended future work.

4.3.3 Analysis of the ‘two body model’

The ‘two body model’ differs from the ‘one body model’ because there is an extra, thin layer that surrounds the channel. The shear stress is applied to this outer layer instead of being applied directly to the channel diluent (as is done in the ‘one body model’). The model prediction results over a range of deflection values for the ‘two body model’ are listed in Table 4.9.

Table 4.9: Predicted steady-state streaming current value

δ (μm)	Maximum Streaming Current (μA)
0	0
.05	-0.02
7.8	-2.32
13.6	-4.06

The absolute value of these predicted trends is plotted in Figure 4.7.

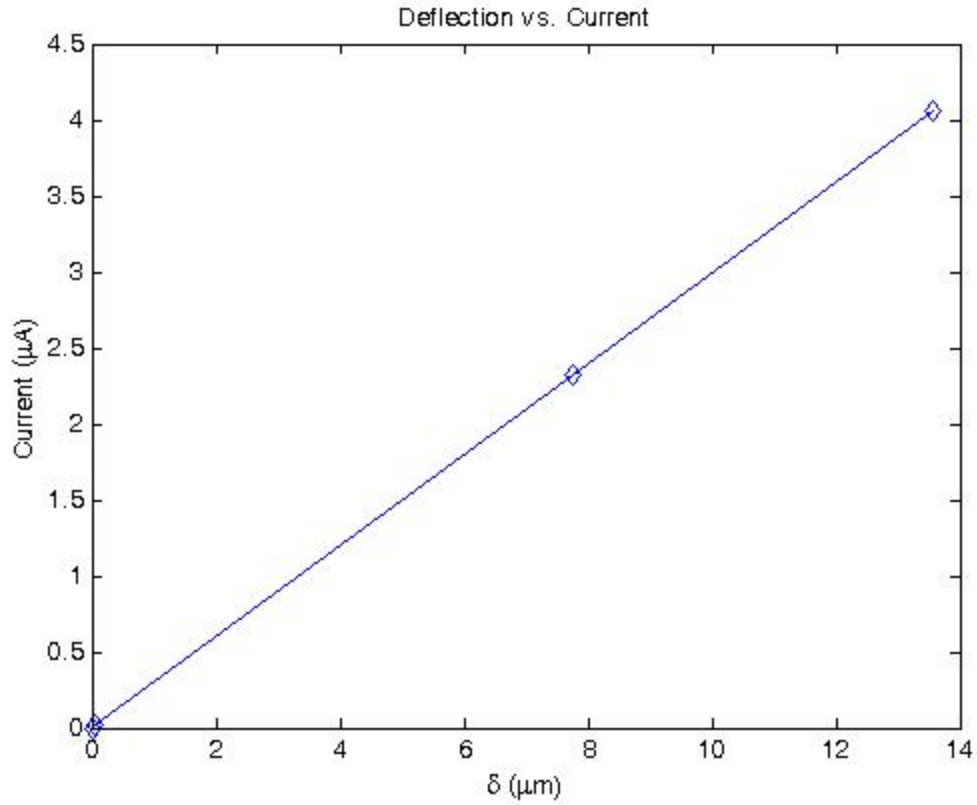


Figure 4.7: Deflection vs. absolute value of current (prediction of trend)

When considering a specific deflection, the model predicts a similar behavior in that there is a peak current that develops, but with a negative magnitude. An example of how the current develops for a particular deflection case is given in Figure 4.8.

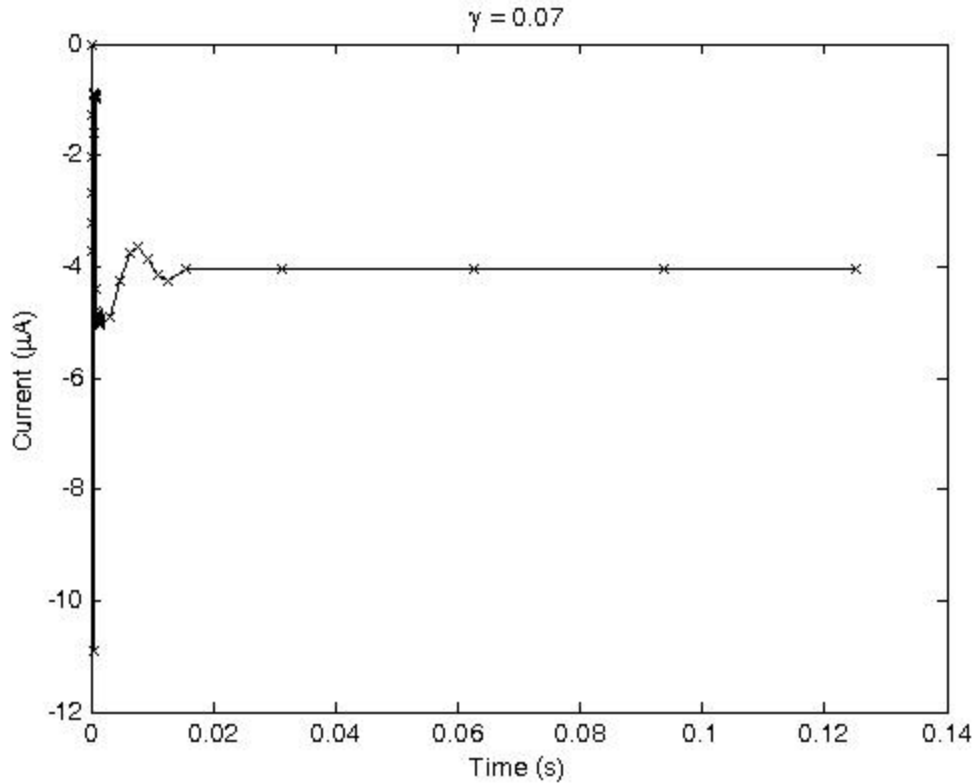


Figure 4.8: Predicted current output for $\delta=13.6 \mu\text{m}$

The first issue to note in Figure 4.8 is that the results factor in the effects of channel rotation discussed in Section 4.3.2. The second issue to discuss is the negative current values given in Figure 4.8. For the purposes of comparing model and experiment this is simply a matter of sign convention (as is taken into consideration for Figure 4.7). However, for the purposes of understanding the physical implications it is a point worthy of consideration. It is believed to be a function of the inlet boundary condition, which has been set as a zero-pressure inlet. The zero-pressure inlet is very important because the alternate option, a velocity inlet (as used in the ‘one body model’), will create a hydrostatic pressure that would not develop in a pure shear case. From the basic study of fluid dynamics, it is understood that fluid particles subject to shearing

(or in other words, angular deformation) will produce further shear forces within the channel diluent; creating vorticities. When there is no hydrostatic pressure in the channel, these vorticities can take on an even more prominent role within the channel, creating a backflow in the velocity. It is this backflow in the velocity that triggers the negative current values that are shown as example in Figure 4.8. A second possible reason for this negative current value is due to the no-slip boundaries at the channel boundaries; in fact, it is acknowledged that any modeling outside of molecular dynamics cannot provide a valid explanation for what is in fact occurring at the channel walls. However, quasi-continuum methods indicate that continuum assumptions can hold for the part of the channel slightly removed from the channel walls[100]. A final note on the results in Figure 4.8 is the consistency of a peak signal, which was also shown in the one-body model. This is encouraging because such peaks are intuitive and confirmed by experimental results (both shear experiments [97] and bending experiments[87]).

With regard to the linear trend over various deflection values, the values in Table 4.9 are calculated via Equation 4.12, where every term is known except for the velocity; which is determined from the ANSYS models. Taking the absolute value of the steady state currents yields a linear trend, which is shown in Figure 4.7. The linear trend with increasing deformation is similar to the prediction of current output when subjected to bending deformation [63].

4.4 METHODOLOGY STRENGTHS AND WEAKNESSES

The main strength of the methodology produced in this chapter is that it has demonstrated the importance of the channel alignment with the stress input. This strength improves the prediction of the current output of the IPTs by an order of magnitude. Finally, the strength of this method

will be demonstrated to hold over various different IPT forms in the next chapter. That is, this improvement in the current prediction will hold over various diluent and cation types. A primary concern that this method does not address is the specific and likely complexity of the ionic channels. Specifically, complexity can refer to the likely tortuosity of the channels, as well as the likelihood of channel breakdown and reformation with time.

4.5 CHAPTER SUMMARY

The purpose of this chapter was to apply the streaming potential theory to calculate the electrical current in an IPT in response to shear deformations. This chapter showed two approaches to a computational model via ANSYS. The one-body model is worthwhile as it shows a clear dependence in the channel alignment. The two-body model is worthwhile because it shows the important effect of no hydrostatic pressure on the development of velocity flow, in that there is a possibility for a backflow. However, the results presented here show that there is quite a difference in the magnitudes of the expected streaming current values. These differences show a conflict as to how the shear-induced current signal behaves over time, thus requiring a more detailed look at how the shear stress affects the current response over time. This is the objective that will be addressed in the following chapter.

5.0 TRANSIENT SHEAR MODEL

As demonstrated in the prior chapter, the evolution of the streaming current over time requires a more detailed investigation. The first set of results from the ANSYS® model which showed evolution of peak and steady-state current (one-body model) were intuitive and similar to experimental results[97]. However, the magnitudes of the current values were high, as well as lacking in signal decay, as the steady state values showed no sign of decreasing. Considering the second set of results from ANSYS® (two-body model), the absolute value of the results yielded current magnitudes more similar to those reported experimentally. However, again the transient signal response did not indicate the expected decay with an increase in time that is expected. The purpose of this chapter is to incorporate a viscoelastic response of the polymer chains into the model. It is hypothesized that the viscoelastic natures of the polymer chains will in turn create the deformation of the EDL and, with the relaxation inherent to a viscoelastic material; this model will generate a more accurate electrical signal value over time.

5.1 BACKGROUND REVIEW FOR MODEL DEVELOPMENT

This work will continue to focus on the material behavior at a local level. Physically, it is assumed that the ionic channel boundaries consist of polymer backbone chains. Therefore, for a given shear stress, there will be conformational changes in the backbone chains that will give rise

to the shearing of the electrolyte regions. This can be modeled via a ‘three-bond motion’, ‘five-bond motion’ or a ‘kink model’. The ‘three-bond’ and ‘five-bond’ motion are best described as a crankshaft type motion. However, the main concern with these types of motion is that they violate ‘swept out volume’. This means that such rotation takes up too much volume within a polymer to be realistic. Therefore, the kink model is the most probable way to explain the conformational changes in the backbone chains and is the model that will be adapted in this chapter. In the kink model, the stem (the link between the atom that moves and a stationary atom) is displaced slightly and therefore can allow mechanical activity [101] [102]. These models were developed in order to explain the molecular behavior that gives rise to relaxation processes. It is hypothesized that a model which can explain these relaxation processes at the molecular level will enable a better understanding and prediction of the expected streaming current.

There has been much discussion in literature about relaxation processes of semi-crystalline polymers. There are two types of relaxation behavior: mechanical and dielectric. The main focus here is the mechanical relaxation. The mechanical relaxations can be characterized differently than the dielectric relaxation by two considerations: by the time for the relaxation process to complete and more importantly, by which region of the polymer that the process dominates. The mechanical relaxations are governed by the amorphous region [102]. The work in this chapter focuses on mechanical relaxation.

Mechanical relaxation is observed during dynamic relaxation studies. There are usually three peaks observed and are called α , β and γ peaks. These are temperature dependent: that is, the peaks will change in shape or position depending on the temperature of the experiments. A generic example of these plots is shown in the inset of Figure 5.1.

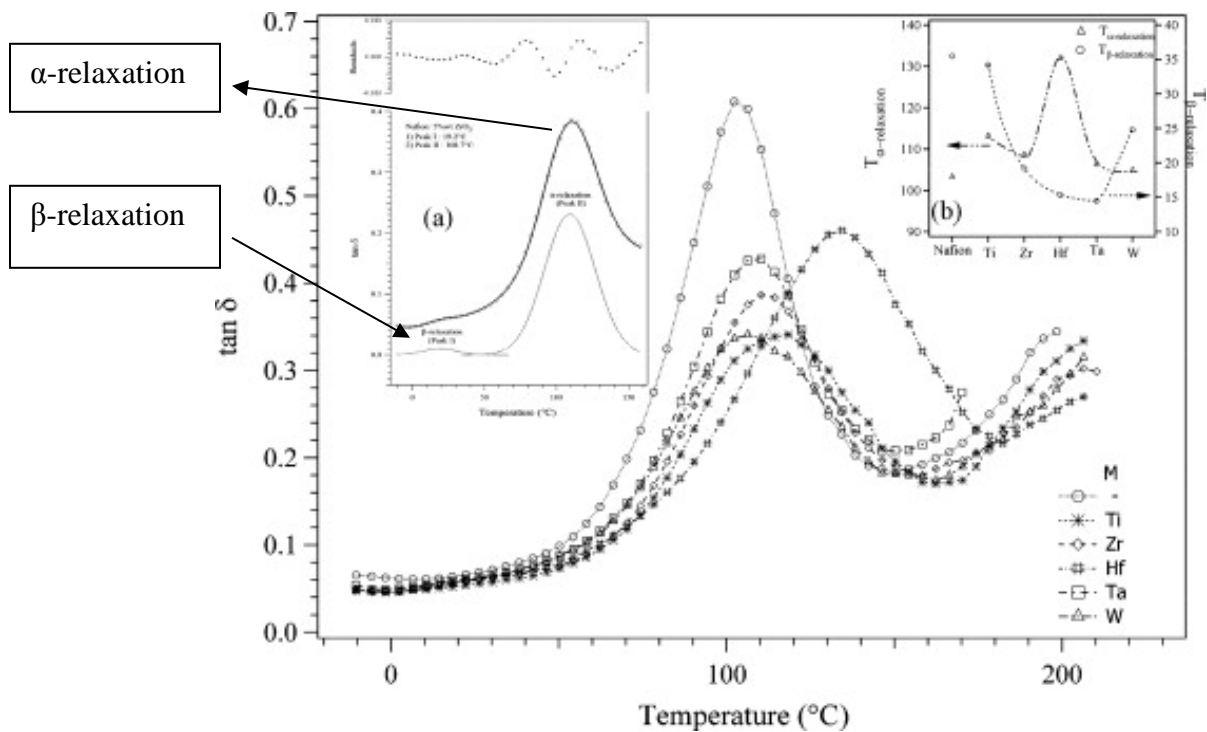


Figure 5.1: Example of a graph indicating α - and β -relaxation. [Reprinted from *Journal of Power Sources*, 187/1, Di Nota, et al., Hybrid inorganic proton conducting membranes based on Nafion and 5wt% of $MxOy$ ($M=Ti, Zr, Hf, Ta$ and W). Part II: Relaxation phenomena and conductivity mechanism, 57-66, Copyright, with permission from Elsevier]

Another important variable of mechanical relaxation in polymer materials is the hydration level. The stiffness is affected by the water content of Nafion® samples, which in turn will govern the stress relaxation behavior. For example, it has been noted that with an increase in polymer modulus, the relaxation moves slower and a decrease in polymer modulus causes faster relaxation[103]. The variation in these relaxation behaviors has been attributed to molecular phenomena. For example, Kyu and Eisenberg discuss a hypothesis that the γ relaxation (or “dispersion”) can be attributed to short range motions of the polymer backbone chains. These authors also hypothesize that parts of the β relaxation can be attributed to movement of the polymer side chains [104].

Mechanical relaxation phenomena vary at different temperatures. Typically the three peaks discussed in the previous paragraph occur in descending order with respect to temperature, where γ relaxations occur at temperatures below the glass transition temperatures[102]. Because IPT applications currently do not consider elevated temperatures, the work that is presented here is in the gamma range of relaxation. So, if the temperature goes significantly up or down, then this model might not hold, or would have to be re-evaluated starting as far back as the statistical weight matrices discussed in Chapter 3.0.

5.2 MODEL DEVELOPMENT

The model development in this section will present a viscoelastic model, with clearly defined variables. These include both mechanical and electrical variables, which will influence both the mechanical and electrical aspects of this system.

5.2.1 Viscoelastic model

A viscoelastic $2N+1$ analogical model is adopted to represent the physical nature of the microstructure of the polymer. Analogically, the N value represents the number of elements that have a spring and dashpot in series. In terms of the physical meaning, the value for N is dependent upon the number density of network chains. Finally, the '1' value in the $2N+1$ model description is a single spring element. The analogical model is shown in Figure 5.3, with the corresponding physical illustration in Figure 5.2

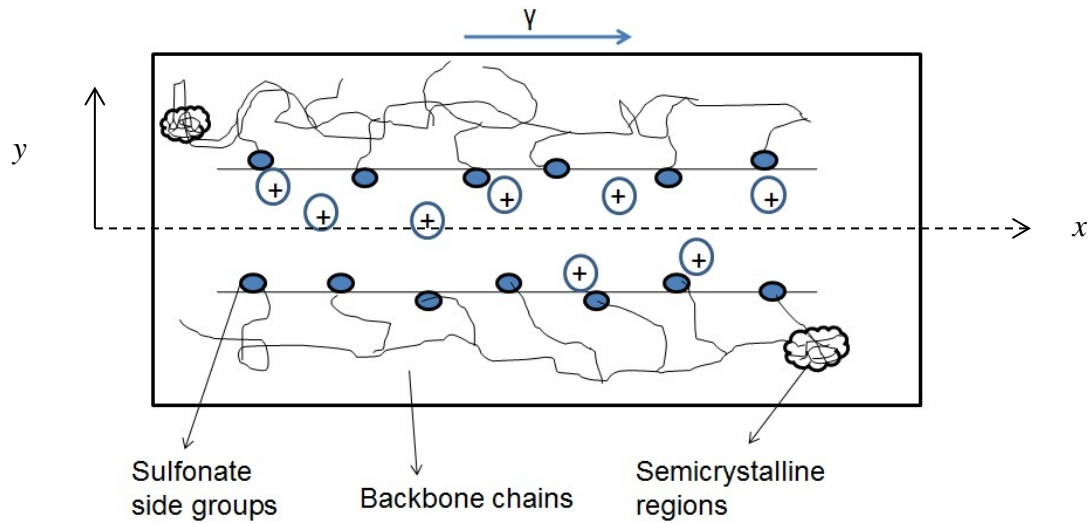


Figure 5.2: Polymer channel region

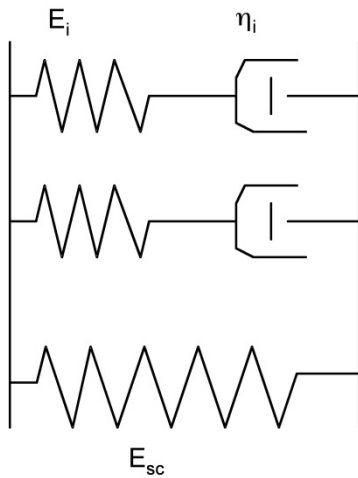


Figure 5.3: 2N+1 Analogical model

This model holds promise because each factor within Figure 5.3 can have a physical meaning. Each successive spring and damper element can represent a single polymer chain within the Nafion® region. The damper (η_i) is to model the response of the polymer chain to external deformation. The viscous nature of this movement will depend on the diluent used within the IPT. The spring element (E_i) is to model the local stiffness of the polymer chain. The

numerical value for E_i is the local polymer modulus that was derived in Chapter 3.0 according to the RIS theory. The choice of E_i is taken according to the results for various scenarios given in Table 3.2. The semicrystalline strength is taken to be about 5000 MPa [40] and is represented as E_{sc} . This strength value is based on the experimental results of Krüger and Fischer investigating the directional stiffness of Teflon® [82].

The corresponding stress and evolution equations for this model can be given in Equations 5.1 and 5.2 respectively.

$$\sigma(\gamma, t) = E_{sc}\gamma + \sum_{i=1}^N E_i(\gamma - q_i) \quad 5.1$$

$$\frac{dq_i(t)}{dt} = \frac{E_i}{\eta_i}(\gamma - q_i(t)) \quad 5.2$$

The other variables within Equations 5.1 and 5.2 left to define are the shear strain, given by γ and t is time. Finally, q_i is defined as an evolution term and. The evolution equation given by Equation 5.2 is meant to model how the individual chains evolve when subjected to an external strain over time. Equation 5.2 will be derived for specific shear strains in the following section.

5.2.2 Polymer chain evolution

There are two shear strain inputs that will be investigated: a step input and a cosine input. In order to couple the external shear strain on the IPT to the system described in Figure 5.2 and Figure 5.3, the first step is to apply the work of Marrucci and Grizzuti who derive the average change in polymer chain free energy under deformation[105]:

$$A(\gamma) = \frac{1}{2} \int_0^1 \ln\left(\frac{1+\gamma^2 x^2 + \sqrt{[x^4(\gamma^4+4\gamma^2)-2\gamma^2 x^2+1]}}{2}\right) dx \quad 5.3$$

The complete free energy change due to deformation is then obtained as [105]:

$$\Delta \mathcal{A} = 3k_B T A(\gamma) \quad 5.4$$

where T is the temperature and k_B is the Boltzmann constant.

In order to continue with the calculation, the first quantity to evaluate is the enthalpy to the free energy via a Gibbs relation. Therefore, a functional form of the change in entropy is required. Using Legendre Transformation on a Taylor-expansion of entropy, it is possible to obtain such an expression as given in the following equation:

$$\Delta S = \frac{\partial^2 \mathcal{A}}{\partial T \partial \gamma} \Delta \gamma \quad 5.5$$

It is prudent to pause for a moment and discuss how Legendre is considered here. Legendre Transformations are for reversible processes. It is known from basic thermodynamics that the entropy for reversible processes should remain constant. It is hypothesized that since the strains input to the polymer chains are very small, that this simulation would qualify for a reversible process. This is for a simplified case of constant temperature and pressures. Post-processing of data shows that the entropy is zero for a case of cosine strain input, with a constant entropy value for the step strain input.

With an expression for the change in entropy and the change in free energy, the change in enthalpy (ΔH) for a constant pressure, temperature and volume is given by:

$$\Delta H = \Delta \mathcal{A} + T \Delta S \quad 5.6$$

Once the change in enthalpy is obtained, the Arrhenius pre-exponential factor (given by A') in the equation governing the frequency of molecular jumps between the two rotational states of the polymer chain can be determined[106]. Namely, in keeping with rotational state discussions of Chapter 2.0, low energy out-of-plane rotational angles are equally likely in mirror

image configurations of the backbone. The frequency of the jumps between these conformations is given in the following equation:

$$\nu = \frac{A'}{2\pi} \exp\left(-\frac{\Delta H}{R_u T}\right) \quad 5.7$$

where R_u is the universal gas constant. This frequency is related to the characteristic time for the polymer chain relaxation (τ') via[106]:

$$\tau' = \frac{1}{2\pi\nu} \quad 5.8$$

The next question to fully evaluate Equation 5.7 is the pre-exponential factor A' . A first order estimate begins by looking at the theory of activated complex for bimolecular molecules. This initial estimate fits since the polymer backbone chain consists of two atom types: carbon and fluorine (Figure 2.3) This constant can be expressed according to [107]:

$$A' = \pi(r_c + r_{fl})^2 \sqrt{\frac{8k_B T}{\pi m_{tot}}} \quad 5.9$$

where m_{tot} is defined as:

$$m_{tot} = \frac{m_c m_{fl}}{m_c + m_{fl}} \quad 5.10$$

where m_c and m_{fl} are the mass of the carbon and fluorine atoms respectively. Also, r_c and r_{fl} are the radius of carbon and fluorine atoms respectively. This work considers a Zimm model in a good solvent to solve for the friction coefficient of the chains to be:

$$\eta_i = \frac{\tau' k_B T}{\langle r_o^3 \rangle} \quad 5.11$$

In Equation 5.11, r_o is the average distance between the cross-links, or average r -value. Finally, Equation 5.11 can be substituted into Equation 5.2 to yield a solvable differential equation.

5.2.3 Boundary and initial conditions

In order to solve this differential equation (5.2), the initial conditions are required: both mechanical and electrical. First, the initial conditions are presented for the mechanical aspects of this system. Next, the electrical conditions are presented in Section 5.2.3.2.

5.2.3.1 Mechanical initial conditions

The mechanical initial conditions refer to the polymer chain conditions and the electrolyte conditions. In this section, the evolution equation of the polymer chains will be derived for two different types of strain input. Also, the conditions for the electrolyte will be established.

Assuming that the polymer chains start from rest, this establishes that $q_i(0) = 0$. The objective will be to investigate two forms of shear displacement: (i) step displacement and (ii) a cosine input:

$$\gamma_1(t) = A \quad 5.12$$

$$\gamma_2(t) = A \cos(\omega t) \quad 5.13$$

Substituting the displacement given in 5.12 back into 5.2 and considering that $q_i(0) = 0$, the non-homogenous equation yields this solution for the step input response:

$$q_1(t) = \gamma_1 \left[1 - \exp\left(-\frac{E_i t}{\eta_i}\right) \right] \quad 5.14$$

Considering a cosine input requires solving a nonhomogeneous differential equation again. In this case, the solution requires a homogenous and a particular solution. The homogenous equation is the same as before:

$$q_H = C_1 \exp\left(-\frac{E_i t}{\eta_i}\right) \quad 5.15$$

Per classic differential equations methodology, a guess is made as to the form of the particular solution:

$$\mathbf{q}_p = C_2 A \cos(\omega t) + C_3 \sin(\omega t) \quad 5.16$$

Substituting 5.16 and 5.13 into 5.2 and matching the coefficients yields 5.17.

$$\mathbf{q}_2 = \frac{EA}{\omega^2 \eta^2 + E^2} * \left[\exp\left(-\frac{Et}{\eta}\right) - \cos(\omega t) + \omega \eta \sin(\omega t) \right] \quad 5.17$$

Next, it is important to consider the governing equations for the flow of the diluent in response to the evolution of the polymer chain: continuity (5.18) and conservation of momentum (5.19).

$$\nabla \mathbf{u} = \mathbf{0} \quad 5.18$$

$$\rho \left(\frac{\partial u}{\partial t} \right) = \mu \left(\frac{\partial^2 u}{\partial y^2} \right) + \rho_e \nabla \phi \quad 5.19$$

These equations are based on the assumption that the velocity (u) is one-dimensional and a function of y (Figure 5.2).

$$\vec{U} = [u(y, t), \mathbf{0}, \mathbf{0}] \quad 5.20$$

The variables ρ and μ in 5.19 are the density and viscosity of the diluent, respectively. Also, 5.19 and 5.18 are non-dimensionalized. The non-dimensionalizations are built using the following:

$$\sigma^* = \sigma * \frac{D_h^2 \rho}{\mu^2} \quad 5.21 \quad \mathbf{a}^* = \frac{a}{D_h} \quad 5.22$$

$$\nabla \phi^* = \nabla \phi * \frac{e z}{k_B T} \quad 5.23 \quad \mathbf{l}^* = \frac{l}{D_h} \quad 5.24$$

$$\mathbf{t}^* = \frac{\mu}{D_h^2} \rho \quad 5.25 \quad \mathbf{v}^* = \mathbf{1} \quad 5.26$$

In the non-dimensionalized equations, the variable D_h is the hydrodynamic diameter. For a channel with a square cross section, that works out to:

$$D_h = 2a \quad 5.27$$

where a is the diameter of the channel.

5.2.3.2 Electrical initial conditions

The coupling between the mechanical conditions and the electrical conditions is with the final term of Equation 5.19. This term is the electric potential due to the strength of the EDL and the streaming potential. The EDL strength is calculated by

$$\phi(y) = \frac{-\rho_e y^2}{2\varepsilon_r \varepsilon_0} + \frac{\rho_e h y}{\varepsilon_r \varepsilon_0} + \zeta \quad 5.28$$

where ζ is the zeta potential, ε_r is the relative dielectric constant of the diluent within the channel and ε_0 is the free permittivity.

The streaming potential is initially zero and is calculated as[108]:

$$E_p = \frac{\partial \phi}{\partial x} = \frac{-\rho_e a^2 \bar{u}(y, t)}{\lambda_{av}} \quad 5.29$$

where λ_{av} is the conductivity of the diluent. This is calculated as[108]:

$$\lambda_{av} = \frac{(eN_A D_i \rho_e)}{R_u T} \quad 5.30$$

In 5.30, e is the elementary electric charge; N_A is Avogadro's number, D_i is the diffusion constant of the ions. Combining Equations 5.28 and 5.29, this creates the following equation for the distribution of the electrical potential field in the channel as follows:

$$\phi(x, y) = E_p x - \frac{\rho_e}{\varepsilon_r \varepsilon_0} \left[\frac{y^2}{2} - h y \right] + \zeta \quad 5.31$$

Equation 5.31 is used within 5.19. Since divalent ions create further complexity to the problem[109], it is necessary to point out that this derivation would only apply to single valence ions. Further assumptions in the application of 5.31 are: (i) the zeta potential is constant for the length of the channel (constant for all x), (ii) quasi-steady development of the streaming potential (not requiring this assumption would require a detailed energy balance) and (iii) this is for a constant temperature. In reality, this system could face possible heat generation that would tie in with assumption (ii). It is also important to note that there are other forces that can possibly in play, such as ion-correlation effects or image effects[62]. However, since the main objective is to build a model that assists in optimizing IPT capability, it is decided to focus on the major effects of the polymer, diluent and major electrical forces. The initial condition for the potential, current and fluid velocity is zero (at rest).

5.2.3.3 Channel boundary conditions and electrolyte velocity equation

The velocity boundary conditions are shown in the following figure.

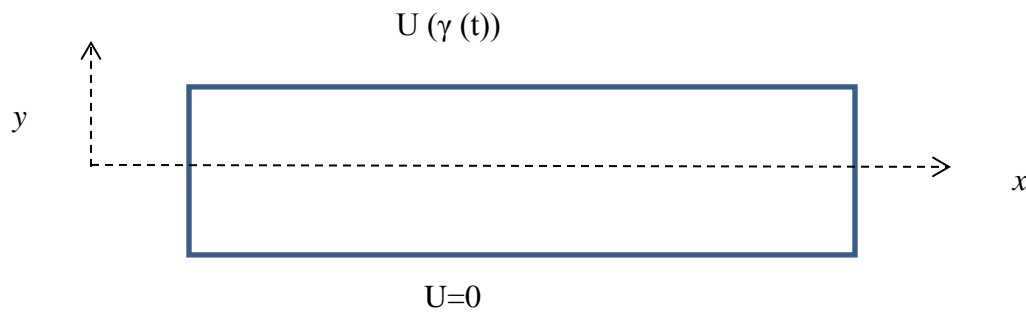


Figure 5.4: Velocity boundary conditions

In order to determine the velocity at the top border of the channel (which has been noted to consist of the polymer chains), the momentum integral equation is used. In this case, this equation becomes important along the length of the channel (in the x -direction):

$$\frac{\sigma(x,t)}{\rho} = \frac{\partial}{\partial x} U^2 \quad 5.32$$

This will yield the following result for the velocity at the top of the channel boundary:

$$U_x^* = \frac{2\sigma^*(x,t)t}{l^*\mu} \quad 5.33$$

It is important to note the boundary condition is time dependent. Thus, the solution has the form:

$$\mathbf{u}(\mathbf{y}, t) = \mathbf{K}(\mathbf{y}, t) + \mathbf{v}(\mathbf{y}, t) \quad 5.34$$

with the boundary and initial conditions:

$$\text{B.C.} \quad \mathbf{K}(\mathbf{0}, t) + \mathbf{v}(\mathbf{0}, t) = \mathbf{0} \quad \mathbf{K}(2\mathbf{h}, t) + \mathbf{v}(2\mathbf{h}, t) = \mathbf{U}(t) \quad 5.35$$

$$\text{I.C.} \quad \mathbf{K}(\mathbf{y}, \mathbf{0}) + \mathbf{v}(\mathbf{y}, \mathbf{0}) = \mathbf{0} \quad 5.36$$

Given these conditions, a functional form of K is selected in order to satisfy the time dependent conditions. Such a functional form is chosen to be:

$$\mathbf{K}^*(\mathbf{y}, t) = \mathbf{U}^*(t) \frac{\mathbf{y}^*}{2\mathbf{h}^*} \quad 5.37$$

The boundary conditions for Equation 5.37 are given as:

$$\text{B.C.} \quad \mathbf{K}^*(\mathbf{0}, t) = \mathbf{0} \quad \mathbf{K}^*(2\mathbf{h}^*, t) = \mathbf{U}^*(t) \quad 5.38$$

By assigning such conditions to the K function, this enables the function of v in Equation 5.34 to have homogenous boundary conditions. However, there is still a ‘generation’ term (from the development of the streaming potential) that creates the necessity of the eigenvalue expansion method in order to develop a complete picture of the velocity over time. The equation to solve becomes:

$$\frac{\partial^2 v^*}{\partial y^{*2}} = \frac{1}{v} \left(\frac{\partial v^*}{\partial t^*} + \frac{\partial K^*}{\partial t^*} \right) - \rho_e \nabla \phi^* \quad 5.39$$

where $1/\nu$ is the inverse of the kinematic viscosity. For this 5.39, a solution form is assumed:

$$\mathbf{v}^*(\mathbf{y}, t) = \sum_{n=1}^{\infty} \mathbf{E}_n^*(t) \boldsymbol{\varphi}_n^*(\mathbf{y}) \quad 5.40$$

where E_n are the Fourier coefficients. . The associated eigenvalue problem reveals eigenvalues are:

$$\lambda_{n,n=odd} = \frac{n\pi}{2h^*} \quad 5.41$$

With the corresponding solution of:

$$\boldsymbol{\varphi}_n(\mathbf{y}) = \sum_{n=1}^{\infty} \mathbf{C}_n \sin(\lambda_n \mathbf{y}) \quad 5.42$$

By substituting the differentiations of v into the governing equation, this yields the following equation to solve for the Fourier coefficients:

$$\mathbf{E}_n^*(t) = \frac{1}{h^* \nu^*} \int_0^t e^{\lambda_n \tau \nu^*} \left[\frac{1}{\nu^*} \int_0^{2h^*} (K_t(\mathbf{y}, t) - E_p^*(\mathbf{y}, t)) \sin\left(\frac{n\pi \mathbf{y}^*}{2h^*}\right) d\mathbf{y} \right] d\tau \quad 5.43$$

Substituting the result back into 5.40, the velocity result will be

$$\mathbf{u}^*(\mathbf{y}, t) = \mathbf{U}^*(t) \frac{\mathbf{y}^*}{2h^*} + \sum_{n=1}^{\infty} \mathbf{E}_n^*(t) \sin\left(\frac{n\pi}{2h^*}\right) \quad 5.44$$

Finally, since the result achieved in 5.44 will be dimensionless, a diluent velocity value can be backed out by:

$$\mathbf{u}(\mathbf{y}, t) = \mathbf{u}(\mathbf{y}, t)^* \frac{\mu}{\rho D_h} \quad 5.45$$

This can be substituted back into the original equation for streaming current given by Equation 4.7. Thus, the derivation achieved in this section is a combination of mechanical and electrical phenomena. The most particular equation of note is Equation 5.44 because these equations have the important incorporation of time dependency into the streaming potential theory calculation of current.

5.2.4 Simulation Steps

The last concept that must be addressed in order to run the most complete model possible is the choice of time and coordinate step. These values must be chosen in order to give the most realistic simulation possible. Therefore, several simulations were run: first with differences in the spatial discretization of the channel. Next, several simulations were run in order to determine the best time step. The information was analyzed with an L_2 Norm via

$$L_2 = \frac{1}{M} \sqrt{\sum_{i=1}^M \left| y_i(\Delta t) - y_i\left(\frac{\Delta t}{2}\right) \right|^2} \quad 5.46$$

where M is the number of data points ($M = 4$ for spatial discretization and $M=5$ for temporal discretization).

The results are shown in the following figures:

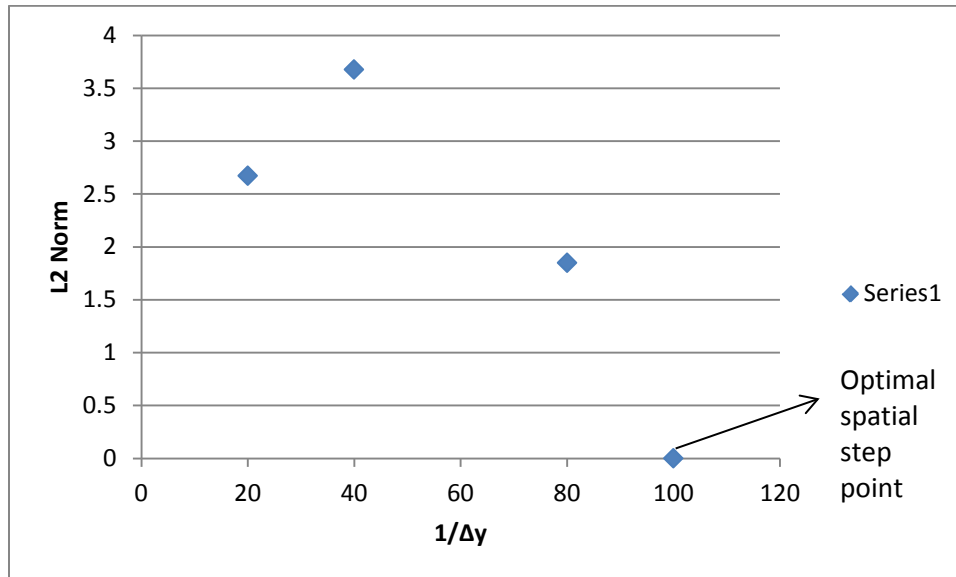


Figure 5.5: Residual calculations to determine spatial discretization

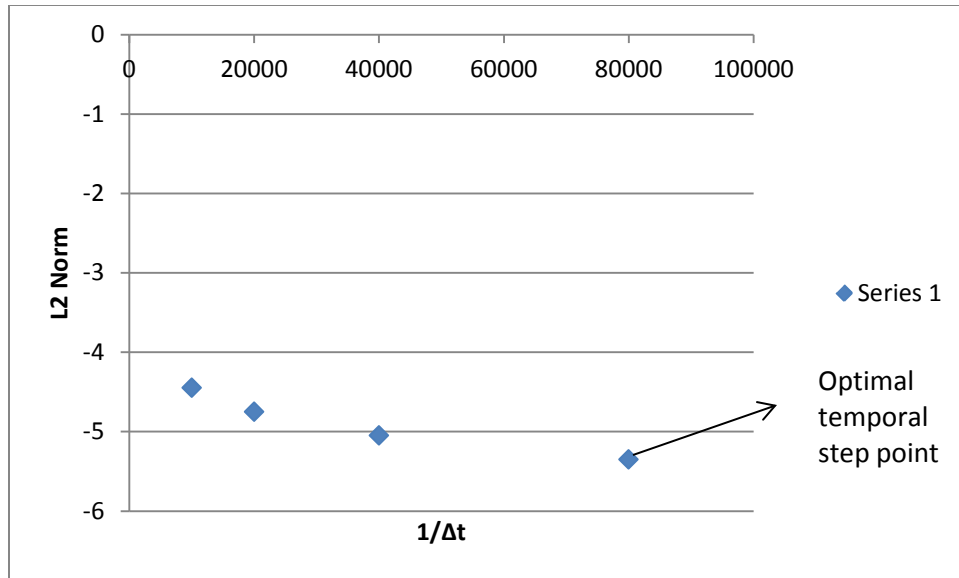


Figure 5.6: Residual calculation to determine temporal discretization

In Figure 5.5, after an initial spike, the norm calculation quickly drops to almost zero. Therefore, the final data point yielded the optimal spatial discretization for the channel. In Figure 5.6, the calculations show a smooth rise until the residual calculations were stopped. It was felt that the final data point yielded a satisfactory time step. The respective discretization steps are noted as follows:

Table 5.1: Optimal model discretization values

Temporal	12.5 μs
Spatial	0.0001 μm

With the initial conditions defined, the simulation steps are as follows:

- 1) Input the shear
- 2) Calculate the free energy steps to find the damping coefficients (Equations 5.3-5.11)

- 3) Calculate the evolution equation for the particular time step, based on the type of shear input (Equation 5.12-5.17)
- 4) Input the results from steps 2 and 3 into the stress equation (Equation 5.1)
- 5) Step forward the velocity boundary conditions (Equation 5.33)
- 6) Calculate the streaming current (Equation 4.7)
- 7) With the mean velocity across the height of the channel, calculate the streaming potential *for that particular time step* and use this calculation in the subsequent time step calculation as a force that affects the velocity development. A key point here is that the change in velocity (for this model) cannot occur at very high dynamic frequencies, for a cosine strain input. This simulation is built to assume that the displacements occur at a pace that enables a quasi-steady state to develop at each time step.
- 8) Update the time step and repeat.

5.3 RESULTS AND DISCUSSION

The model outlined in the previous section was run for a step strain input given by Equation 5.12. The sample was considered fully hydrated by the respective diluents. The important parameter differences are given in Table 5.2. The density and viscosity values are the standard, known values for the liquid density and viscosity.

Table 5.2: Input Parameters

	Water	EMI-Tf
Viscosity (kg/m*s)	1.002×10^{-3}	45×10^{-3}
Density (kg/m ³)	998	1387
Backbone Modulus (MPa)	9.7*	5.9*
r_0 (Å)	19.9*	22.6*

*Backbone moduli and average r -values are derived from the RIS methodology described in Chapter 3.0.

In this section, the results when the shear strain input is a simple step are considered first. In the following section, the results are considered when the input is a dynamic shear strain.

5.3.1 Step shear strain results

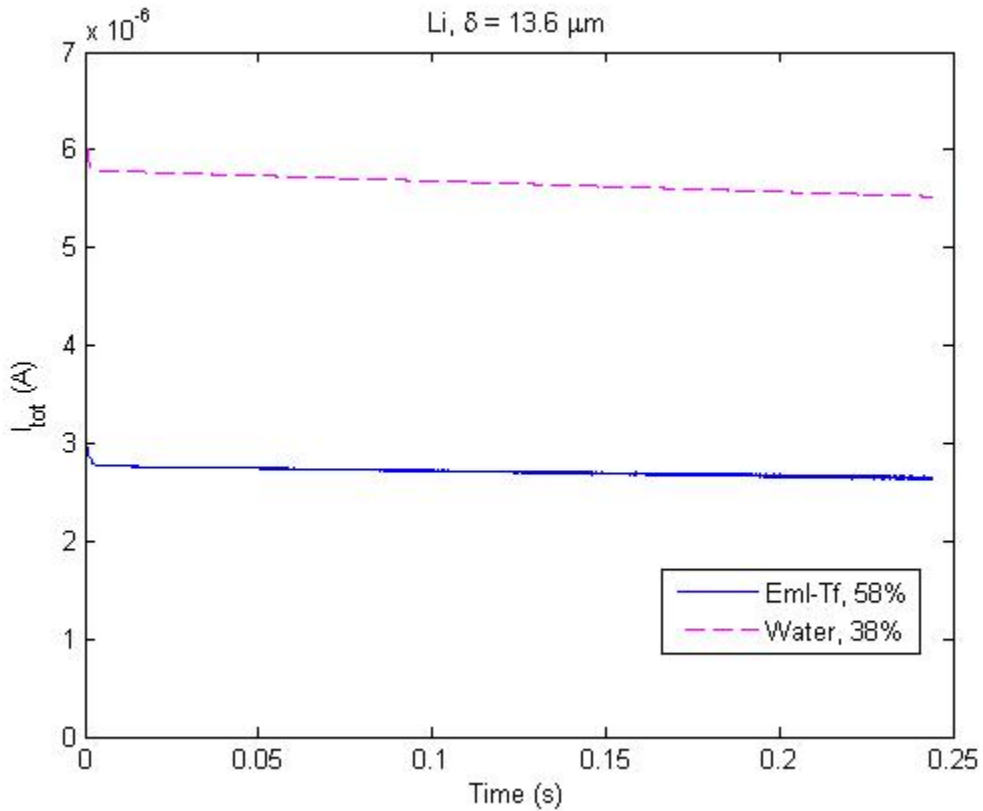


Figure 5.7: For a step input, Li+ exchanged IPT, delta = 13.6 micrometers

Table 5.3: Maximum current values for Li⁺ ion models with different diluents

Case	Max current (μA)
EmI-Tf	3.17
Water	6.65
Ratio	~2.1

The maximum, peak currents for a step strain input with different diluents are given in Table 5.3. This shows us that water gives us a higher current output than EmI-Tf as a diluent by a factor of about 2. For purposes of experimental comparison between these two diluents, bending tests can reviewed, as there is a lack of experimental results for a water-imbued IPT in shear deformation. Bennett and Leo compared water and EmI-Tf in bending tests by measuring sensitivity (C/ϵ). While they measured their samples at various frequencies, water showed about 2.7 fold higher sensing signal than EmI-Tf, which compares well with this model results[30].

In Figure 5.7, the expected decay that should occur over time is illustrated. However, zooming in to very quick time scales (Figure 5.8 and Figure 5.9), reveals a peak development, similar to what was seen in the ANSYS model. These peaks appear at a comparable time with what has been measured in experiment[98].

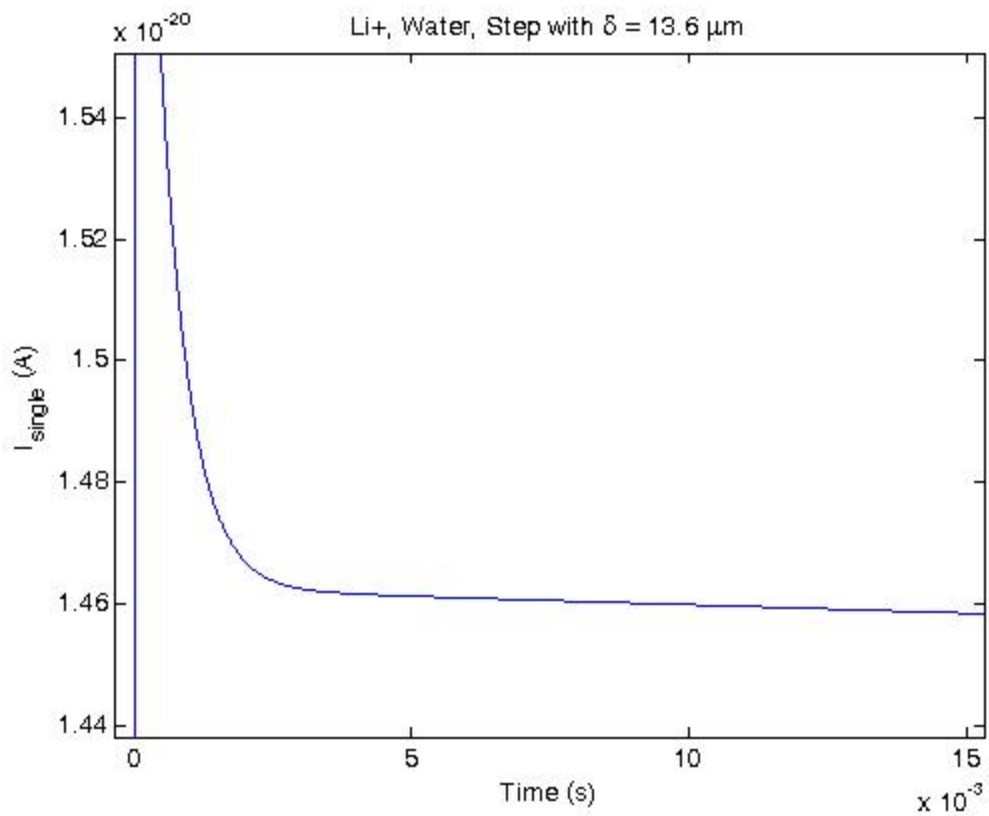


Figure 5.8: Zoom in of the streaming current with water diluent (single channel results)

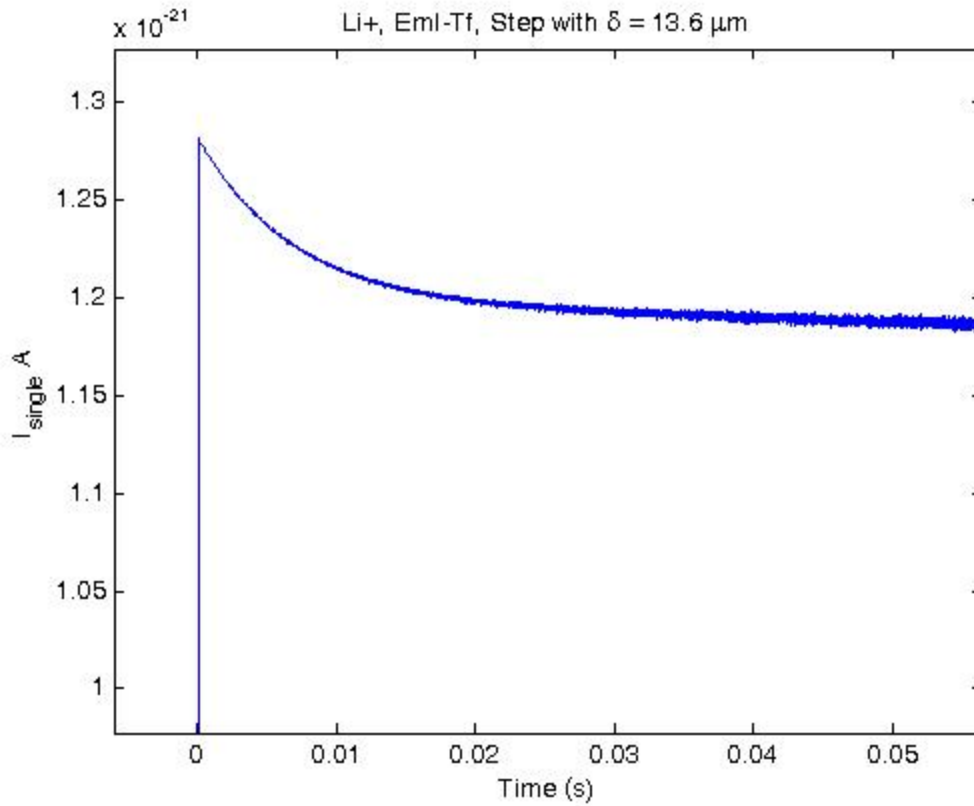


Figure 5.9: Zoom in of the streaming current with EMITf diluent (single channel results)

Considering a trend line on how fast the signals begin to decay in Figure 5.8 and Figure 5.9, the current signal with water drops off at a faster rate; by a factor of 11.

Table 5.4: Rate of current signal decay.

Case	Slope of linear fit
Water	-2.9e-21
EmI-Tf	-2.66e-22
Ratio	11.2

This rate of decay is intuitive because EmI-Tf has both a higher density and a higher viscosity. However, the significance of the numerical ratio cannot be commented on at this time.

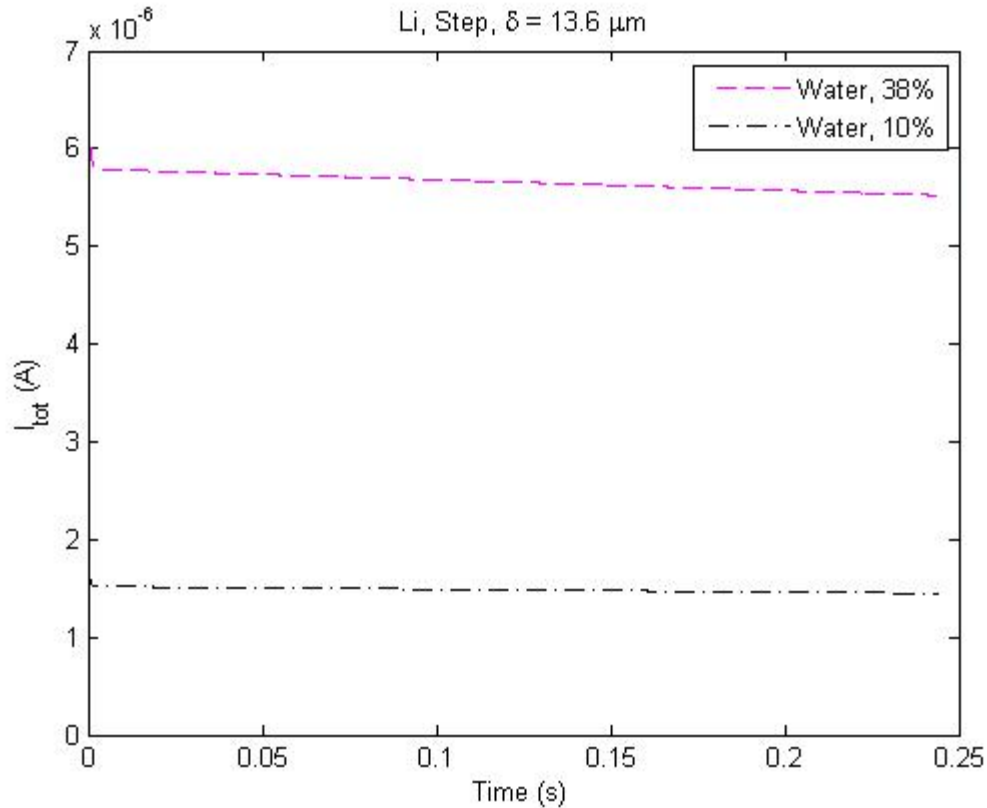


Figure 5.10: Comparison of total expected current for Lithium at different hydration levels (total current output)

The next consideration in this model is the results shown in Figure 5.10 of water with different levels of hydration. The results here also show the expected result that the fully-hydrated sample has a stronger current output than the dehydrated sample. The maximum current values, along with the ratio comparing the two cases are shown in Table 5.5. The results show that the fully hydrated water case only performs better than the dehydrated case by a factor of 3.8 *in shear*. Again, unfortunately, there are no known analogous cases in literature for comparison, not to mention that the bending studies are inconclusive. Further, experimental reports note that the actual measurement of hydrated vs. dehydrated IPT samples are difficult to control [44,110]. The only comparison that is somewhat related is a measurement of conductance by Aldebert et al. [88]. In this work, the authors found an improvement in the conductance by a factor of 6

when going from a dehydrated IPT sample to a fully hydrated IPT sample. This compares well to this model, given the different measurement values and the different form of stress inducement to the sensor.

Table 5.5: Maximum current results for water cases, varied hydration

Case	Max Current (μA)
Water – 38%	6.65
Water – 10%	1.74
Ratio	~3.8

The other major variable investigated in this work was the difference in counterion types. The results comparing Li^+ and Na^+ ions are given in Figure 5.11.

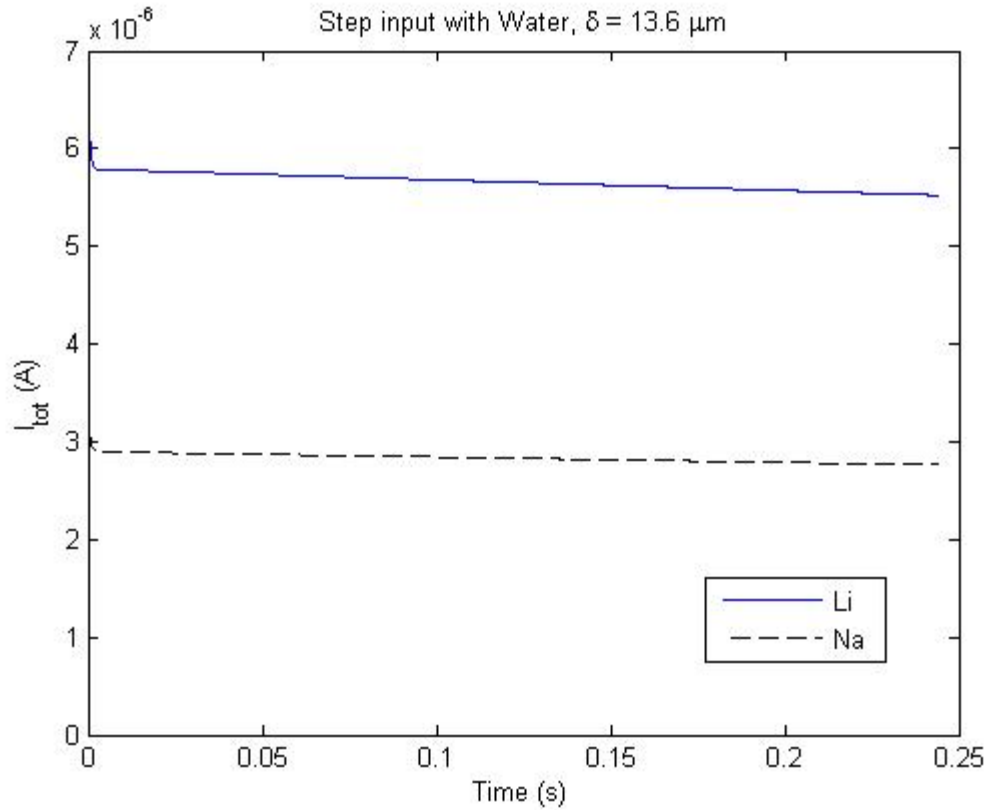


Figure 5.11: Total current output for a Li- and Na-exchanged IPT samples

The maximum current values for the model with different cation considerations are given in Table 5.6.

Table 5.6: Maximum current value comparison with different cations

Li	6.65 (μA)
Na	3.31 (μA)
Ratio	2.01

As shown in Table 5.6, there is a ratio of about 2 when comparing results from different ion-exchanged IPT predictions. Experimental results indicate that samples exchanged with Li^+ should perform better than Na^+ by a factor between 5-10[34]. Comparing the modeling methods

used to generate the information in Table 5.6 with the modeling methods used in Table 3.7 (modeling Li^+ vs. Na^+ exchanged IPTs in bending), a pertinent note is the consistency of ratio of the predicted current results. Here, Li^+ has a stronger expected current by a factor of 2, while Li^+ -exchanged IPTs have a stronger expected current by a factor of 2.3 in Table 3.7.

While the ratio in Table 5.6 is meant to evaluate the capability of the model to compare between IPTs exchanged with different cations, there is experimental work with regard to Li^+ -exchanged IPTs in shear. The results are shown in Figure 5.12.

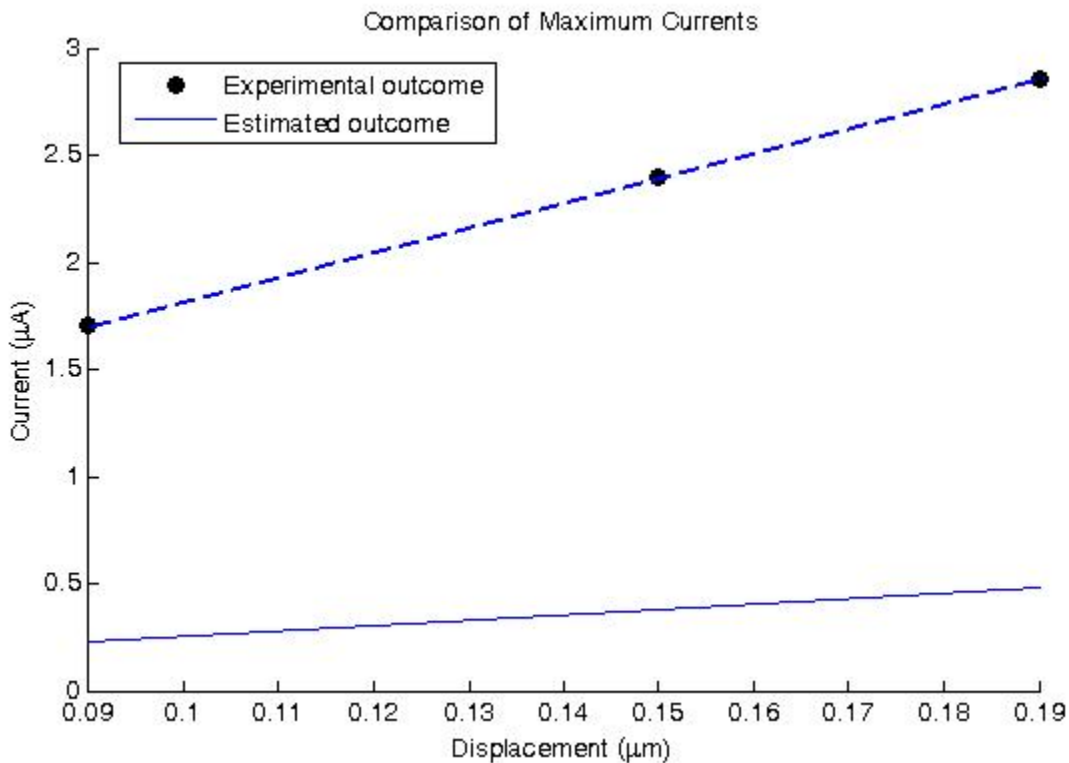


Figure 5.12: Comparison of experimental[98] and estimated current outcome. Note: No empirical fitting imposed

The results here show the strength in predictive capability of the streaming potential model. A key point on these results is that there is no empirical fitting in order to obtain the results given in Figure 5.12.

The final consideration for a step input strain is how the difference in electrode volume fraction affects the sensing signal of an IPT. The step input was modeled on a Li⁺-exchanged, IPT permeated with EmI-Tf. The results are shown in the Figure 5.13 below.

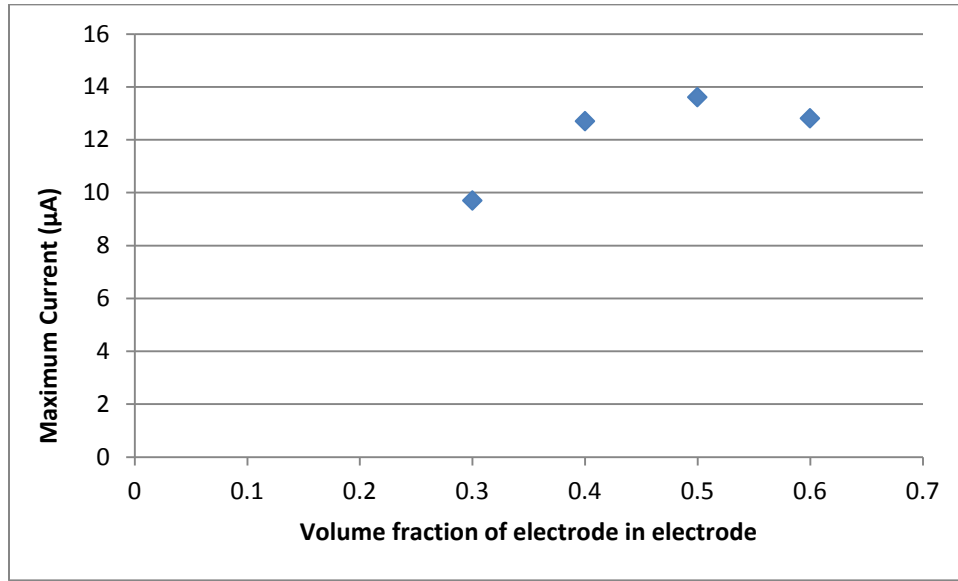


Figure 5.13: Maximum current for different volume fractions of RuO₂ ($\delta=13.6 \mu\text{m}$)

The model predicts that there is an optimum value of the volume fraction of electrodes, similar to the model for IPTs in bending previously presented by Gao [111]. A further note on the calculations used to generate Figure 5.13 is the inclusion of the streaming factor as described by Weiland and Akle. The purpose of the streaming factor is to account for the change in the channel diameters as the electrode loading begins to increase [15]. The peak under the shear deformation is consistent with the peak observed by the prediction of Gao for bending deformation, at an optimum value of 50% [111]. This is potentially a significant result, as the calculation used to generate the results in Figure 5.13 is slightly modified from the work of Gao, yet the trend remains the same. A discussion is given as follows.

Consider the amount of ionic liquid that is actually available for channel formation (since the DAP steps consider the electrode mixed in with the ionic liquid[1], the concentration of the electrode necessarily affects how much diluent is available for uptake), then the volume fraction of the ionic liquid is actually given by Equation 5.48.

$$\varphi_{IL} = \frac{w_{IL}*(1-\varphi)*Vol*\rho_{Nafion}}{\rho_{IL}} \quad 5.47$$

In Equation 5.48, the variables are defined in the following table:

Table 5.7: Input parameters for Equation 5.48

w_{IL}	Weight uptake of liquid	0.59
φ	Electrode volume fraction	0.2-0.6
Vol	Volume of IPT electrode region	2*Len*width*thickness
ρ_{Nafion}	Density of Nafion (kg/m ³)	2000
ρ_{IL}	Density of ionic liquid (kg/ m ³)	1387

The reason for this calculation step is that there is electrode and liquid Nafion® within the mixture that also includes the ionic liquid. Once the expected volume fraction of the semicrystalline regions is defined within the polymer region ($f_{s,c}$), it is possible to determine how much volume fraction of the backbone is available by subtracting from the volume fraction of Nafion®:

$$f_{bb} = f_{Nafion} - f_{sc} - f_{liq} \quad 5.48$$

These results indicate that a 50% volume fraction of particulate should be used, similar to the case in bending presented in Gao's earlier work[65].

5.3.2 Oscillating shear strain results

The current output response was considered for a cosine-type strain input of the type given in Equation 5.13. First, the model was run for a total of 3 seconds. This created the following result:

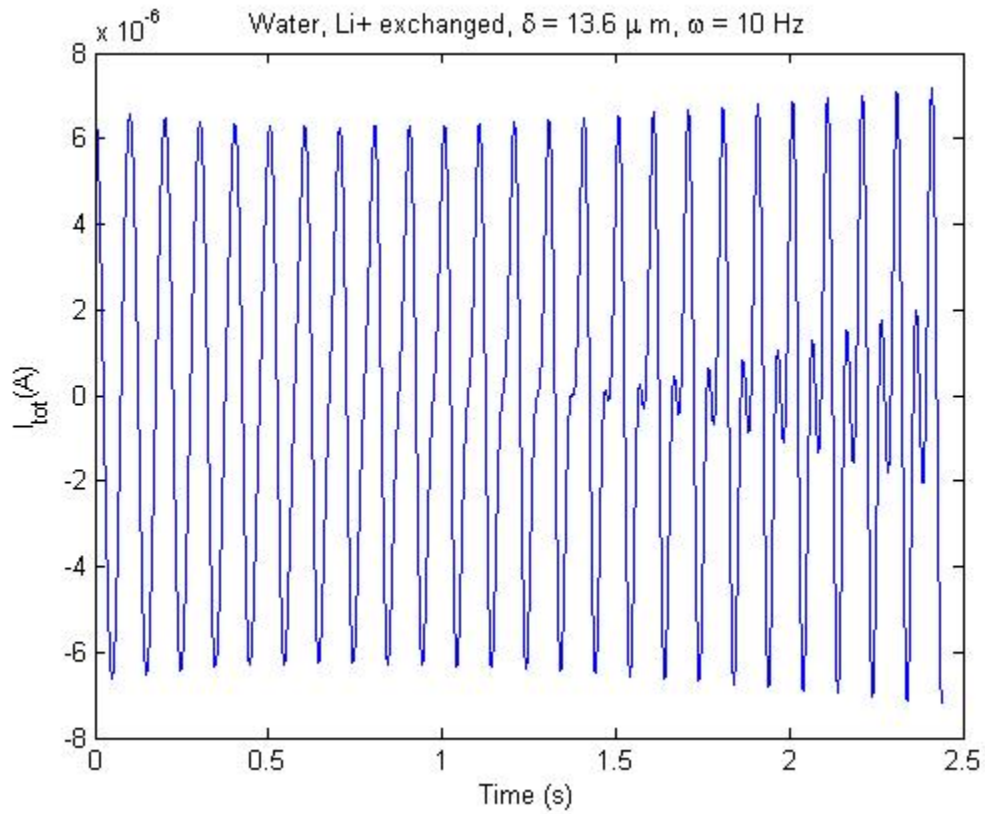


Figure 5.14: Current output for input strain of $\gamma = \delta \cos(\omega t)$

The results in Figure 5.15 show the current output grows with time. The reason for this growth in the current signal output is found in the transient velocity term in Equation 5.34 and plotted in Figure 5.16.

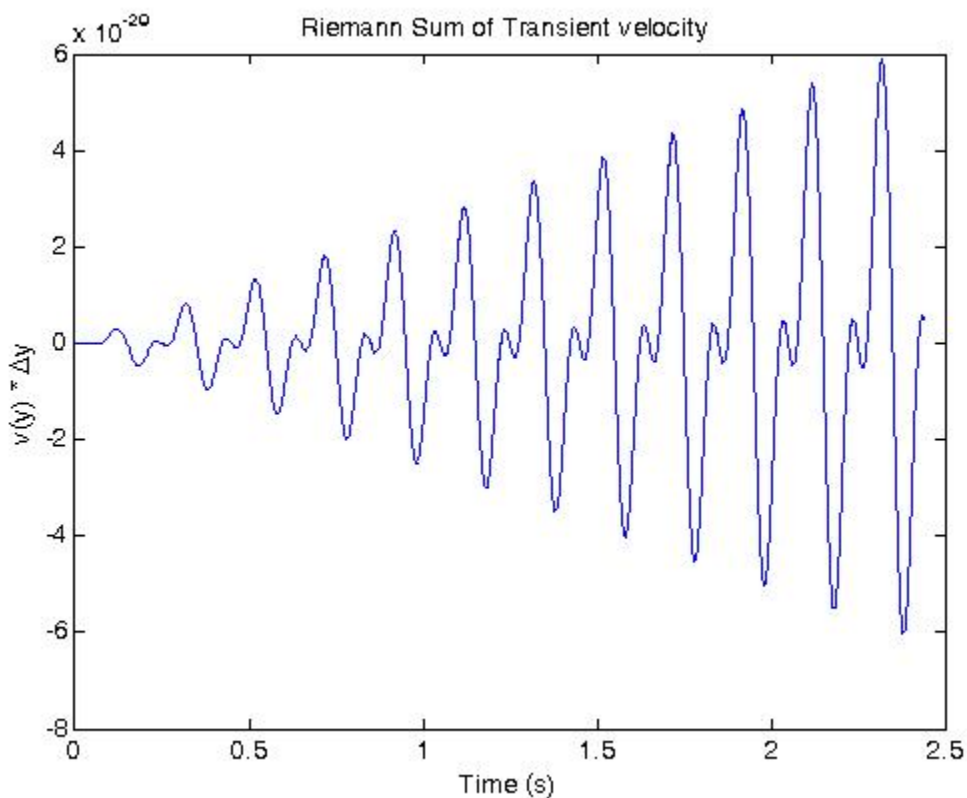


Figure 5.15: Plot of the average transient velocity

Considering how this term is derived as noted in Section 5.1, the exponential terms make a big difference. There are two important points to note in this transient term. First, a possible source for allowing this type of growth is that not all of the contributions to the energy of the diluent flow are considered. A big factor of concern is the temperature. First, the temperature will affect how compliant the polymer chains are. This is evident in statistical weight matrices that are dependent on the temperature. The second piece of evidence in the theoretical view is

the lack of the temperature *generation*, or Joule heating, considered as negligible in the velocity equations developed in this chapter. There is experimental evidence that the role of temperature plays a big role in how an IPT behaves. If a heat lamp was used in the production of the IPT, in our lab, there was a noticeable two second delay before the IPT deformed significantly, indicating the effect of the heat lamp. It is possible that considering further energy terms, like temperature, would make a difference on whether this growth in the current signal would be cancelled out and reversed.

A second reason for this unstable growth in the expected current is explained as follows. This comes from the work of Kumar and Shankar [42]. These authors were investigating how the ability of the channel wall (consisting of material such as a polymer) affects the flow of a fluid in Couette flow. Considering just the more simplified explanation of their results, the authors first consider the wavespeed of the fluid. A simple proportionality is given by[42]:

$$v \propto \sqrt{\frac{\eta}{(\tau_R \rho)}} \quad 5.49$$

where v is the wavespeed, η is the fluid viscosity, τ_R is the ‘relaxation time of the system’ (given by Equation 5.8) and ρ is the fluid density. The resulting wavespeed is used to calculate the wavelength[42]:

$$\lambda = v / \omega \quad 5.50$$

where ω is the frequency of the dynamic strain input into the system. Finally, the reciprocal of the wavelength is the wavenumber[42]:

$$\alpha = \frac{1}{\lambda} \quad 5.51$$

According to Kumar and Shankar, instabilities arise when the wavenumber is “large”. Conversely, when the wavenumber is “small”, you can achieve stable results.

There is no certain definition given as to what these values of “small” and “large” are. It was determined that in this system, “small” and “large” are dependent upon the diluent and the strength of the polymer backbone (τ_R is a function of the polymer backbone stiffness). The calculated wavenumbers are given in Table 5.7.

Table 5.8: α -values for different diluents at different frequencies

ω	Water	EmI-Tf
10 Hz	1.745	0.307
5 Hz	0.8725	0.1535

For example, with water as the diluent, when $\alpha > 1$, the predictions on current generation begin to grow (Figure 5.17). However, if $\alpha < 1$, the predictions show an expected decay (Figure 5.18).

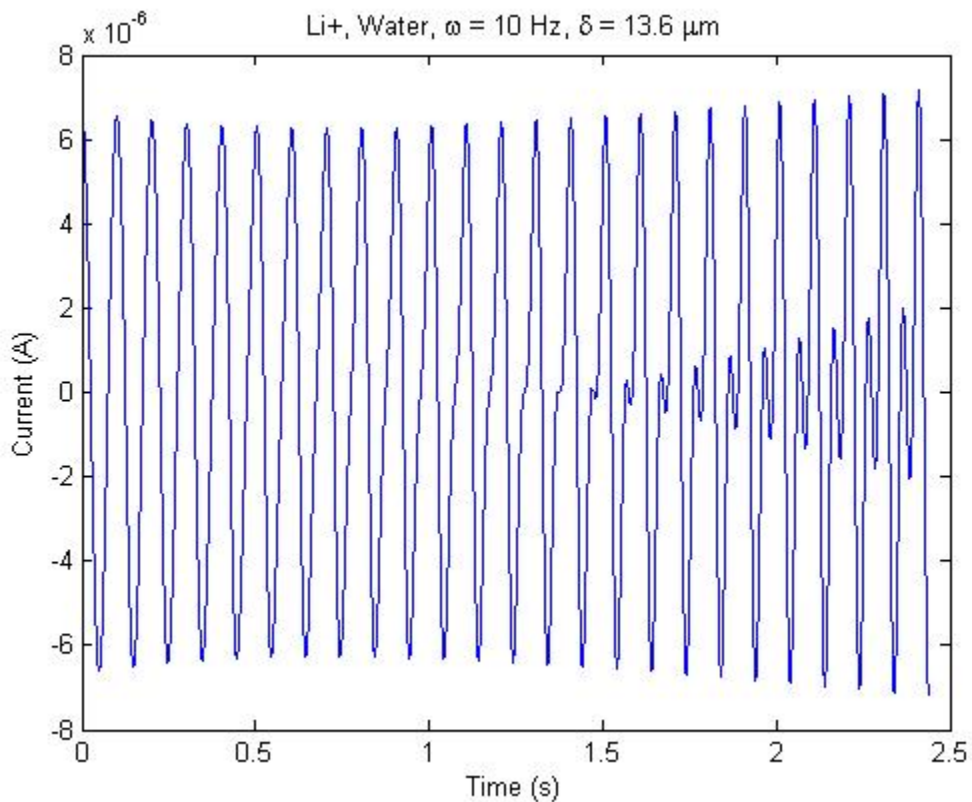


Figure 5.16: Predictions for an IPT with Li+, Water, $\omega = 10$ Hz, $\alpha = 1.745$

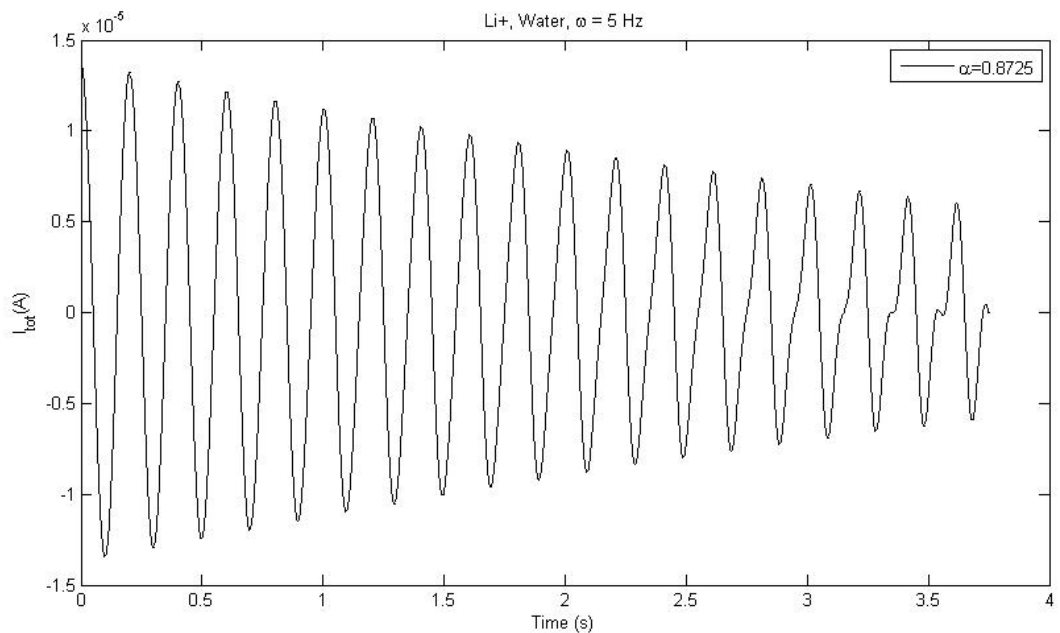


Figure 5.17: Output current for an IPT with $\omega = 5$ Hz and $\alpha=0.8725$

However, with EmI-Tf as a diluent, unstable behavior appears even with $\alpha=0.307$. But, reducing the frequency of the dynamic strain leads to an adjustment of α to $\alpha=0.1535$ and a current output signal that decays in a similar fashion to Figure 5.18.

It is clear that such unstable behavior is not physical, as oscillating strain inputs of various methods show stable behavior[55]. There are two ways to address this discrepancy between model and experiments. First, in terms of the model, a functional form can be determined to find the maximum frequency that a model can produce reasonable results. A second method would arise in perhaps an experimental correction factor. This factor would be a function of time, the diluent density, viscosity and the stiffness of the polymer backbone. All of these are important as it is clear that α is a function of each of these variables.

A final point that should be considered is to compare how the model predicts the differences between oscillating and step inputs with experiments. When looking at the model results presented so far, the result given a cosine-type input is slightly more than the result for a step-type input.

Table 5.9: Maximum current output comparison, given strain input

Current output (μA)	EmI-Tf	Water
Step	3.07	5.89
Cosine (10 Hz)	3.17	6.67

Looking at experimental results, there is consistent evidence that a step input should yield a higher current signal than some form of dynamic input. The difference in terms of experimental results is exactly how much larger the output signal is for a step input than for a oscillating input. First, Chen et al. found that the step input yielded current measurements that were double those of a dynamic input. Again, these authors investigated IPTs under bending strain. Further, the authors discuss the oscillating input only as “damped, oscillatory input”[89]. A second reference gave a difference of about five: that is, the step input yields better current output by a factor of five. Kothera (who’s objective was to study non-linear effects) discusses an input only as subjecting the sample to an *s*-curve for 10 seconds, followed by 50 seconds of no input[112]. Looking at the results from this model, there is not as a significant difference in the magnitude of the different inputs, but there is still a slightly higher output signal from the step input than the oscillating input. The experiments performed by Chen et al. looked at IPMCs with water as a diluent. In the work of Kothera, the diluent was EmI-Tf.

A possible reason for the increased parity between the two different strain cases in the model is due to its simplicity. Intuitively, the experimental results seem to indicate a higher

resistance to the mechanical input strain. This resistance appears to be either weaker or not accounted for in this model. Causes for such a resistance can include temperature effects, or further electrical forces not accounted for in this model. Looking at the initial strains (such as Figure 5.8 or Figure 5.9), the current output develops quite rapidly. Again, the intuitive sense would be that there would be a slight delay in the output signal.

5.4 METHODOLOGY STRENGTHS AND WEAKNESSES

The strength of the modeling method presented in this chapter is that it begins to capture the time-dependent behavior of the polymer based on local variables. Further, this method is easy to adjust for different IPTs. That is, this method can easily generate results based on simple inputs of diluent type, stress input and cation type. However, the key weakness in this method is it can only be applied to small, viscoelastic behavior. Larger deformations and nonlinear behavior will require a more advanced modeling methodology, which would include more advanced understanding of time-dependent responses of the local constituents of the material.

5.5 CHAPTER SUMMARY

While Chapter 4 provided insightful observations on the effect of the morphology, Chapter 5 improved the level of accuracy of the predicted current. Second, the work in this chapter validates the peak seen in the current output signal in Chapter 4, but includes the expected decay in the signal over time for step input, along with more accurate boundary conditions. Also, the

work presented in this chapter enabled a more thorough review of several variables: including the effect of the diluent, electrode load variation and the type of input strain that the IPT can be subjected to in shear.

With an oscillating shear strain, the model displays instability in the velocity of the diluent. It is assumed that a more thorough model (such as including temperature effects) would correct this instability. By creating a more thorough model that includes temperature effects, it is possible to capture a more accurate picture of energy in the system that could balance out the instability shown in this oscillating model.

As the model currently stands, calculations of the wavenumber enable a preliminary understanding of what combination of diluent and at what frequency the shear strain should be input in order to develop the experimentally observed, steady current oscillation.

6.0 EXPERIMENTAL VALIDATION

Until this point in the dissertation, a model to explain the sensing of IPTs has been presented based upon streaming potential theory. The modeling results have shown the importance of the strength of the polymer backbone at the *local* level in predictions of the streaming current for IPTs. The modeling results have also shown the ability to predict how this streaming current would respond to different processing techniques (such as extrusion and drawing). Of course, the bulk of the modeling work has focused on predicting the sensing response of the IPTs in shear.

The purpose of this chapter is to present experimental work to validate modeling results on the effects of: annealing and diluent uptake. It should be noted that the experimental work was performed collaboratively with Bilge Kocer.

6.1 EXPERIMENTS: ANNEAL VS. ISOTROPIC

Within the lab, the supply of Nafion® is type N117, which refers primarily to the thickness of the polymer. According to DuPont, this material is extrusion-cast[113]. Nafion® samples manufactured with extrusion can force crystallinity to develop within the polymer[12].

Annealing Nafion® has been shown to affect the mechanical and electrical properties of the material. Reports have looked at how thermal treatments of the material affect these

properties when the thermal treatment is applied at different points in the processing of the final product. For example, annealing has been investigated by the fuel cell community (prior to fuel cell pretreatment steps) to see how heating affects the conductivity of Nafion®[114]. Another report focused on fuel cells looked at the mechanical properties and the water uptake differences among stretched and annealed Nafion®[77]. Here, Lin and coauthors acknowledge that *with* annealing, the “mechanical properties” (specified only in terms of fuel cell operations) are not as good as Nafion® samples *without* annealing. However, the problem is that if the polymers are ‘substantially more crystalline’ (as noted by the authors), then there might be a reduction in water uptake. In this case, the crystallites would behave as cross-links that would limit membrane swelling. Between these two reports alone, the results indicate that annealing can improve conductivity, yet be detrimental to the mechanical properties of the polymers.

Even the term “mechanical properties” is a general description in terms of what annealing does to Nafion® samples. Questions arise as to how the annealing affects stiffness and even the morphology. Therefore, some research has also focused on how hydrothermal treatments affect the performance of Nafion® [115]. Again, this is another factor that is important to the fuel cell community and should be understood in dealing with sensors because the temperature and hydrothermal cases still affect the performance of the material, even if the pre-treatments are a little bit different between fuel cell processing and IPT processing.

While the work of Hensley et al. and Lin et al. demonstrate that the question of *when* to anneal Nafion® makes a difference in the quality of the final polymer, there is also a question of *how* to anneal the polymer. Specifically, there are variations in the environmental conditions of the annealing process. For example, previous works cite annealing in vacuum at temperatures ranging from 60°C-140 °C for a wide variety of time (e.g. 4 hr.-1 day) [77,115-119]. However,

there was also a report of annealing Nafion® in an air environment, thus removing the necessity of building a vacuum chamber. It is important to reiterate that in this cited work, the final application of the polymer was for fuel cells. Here, the polymer was annealed for 165 °C for only a short time: 3 hours[114]. Because of the simplicity of this procedure, this was chosen as the procedure with which to pursue the experimental study.

6.1.1 Annealing Experimental procedure

Since the procedure to anneal the Nafion® samples for production of the IPTs was chosen to follow the work of Hensley, et al., the authors' conclusions were taken into consideration when joining the annealing treatment with the DAP. The authors concluded that it was better to anneal the as-received samples *before* the ion-exchange procedure because it was found that the samples were more ion-conductive than if the ion-exchange was done after the annealing.

6.1.1.1 Preliminary Annealing Results

In order to evaluate the effectiveness of the annealing temperature and time of Hensley, et al., preliminary annealing was carried out on Nafion® samples in order to confirm that the thermal treatments would have a noticeable effect on the global stiffness of the polymer. For these experiments, dog bone samples were cut according to standard ASTM D638[120]. The method of cutting was to draw templates of the specimen dimensions in a SolidWorks sketch and print out paper templates. Then, the paper template were placed over the Nafion® and cut using an X-Acto® knife. However, in this preliminary stage, the samples were *not* cut in the same direction. That is, while samples may be cut along one direction of the larger Nafion® sheet, other samples would be cut at a 90° angle to the other samples.

On the first day, two as-received samples were cut and placed into a MTI-1K tensile machine. The setup parameters are noted in Table 6.1.

Table 6.1: Tension test sample and machine setup

Velocity (m/s)	0.05
Preload Force (N)	0.0055
Dog bone width (mm)	6.35
Dog bone gage length (mm)	33
Nafion® thickness (µm)[113]	183

The velocity of the tensile machine crosshead was chosen according to the standard ASTM D882[121]. The preload force was added in order to comply with the tensile machine software. This particular force value was chosen to be similar to the work of Kawano et al. [32].The dog bone width and gage length were measured according to the ASTM D638 standard[120].

Further, four more samples were cut and annealed according to the specifications laid out in Hensley et al.[114]. Two samples were then tested to the same tensile test specifications as the as-received samples within ½ hour after being removed from the oven. The final two, annealed samples were stored in a fume hood until the following day for tensile testing. The tensile test results are noted as follows:

Table 6.2: Preliminary Tensile Test Results

<u>'As received'</u>	<u>Day 1</u>		
Sample No.	Modulus (MPa)	Sample No.	Modulus (MPa)
1	126		
2	152		
<u>Annealed</u>	<u>Day 1</u>	<u>Annealed</u>	<u>Day 2</u>
1	153	1	165
2	163	2	146

The results of Table 6.2 tell a few important conclusions. First, there is a significant difference first between the two as-received samples. While two sample measurements cannot be considered a representative sample, the difference could indicate the importance of cutting the samples in the same direction. The second important conclusion from these results shows that there is no significant difference in the overall polymer modulus in waiting overnight. The third result is that there is not a significant difference in the modulus between the as-received and the annealed samples. Therefore, the conclusion is that there has been a significant change in the polymer cannot be made at this point.

6.1.1.2 Preliminary Annealing Procedure Alterations

Given that the preliminary annealing results showed little difference in polymer effects, it was decided to increase both the time and temperature of the thermal treatment.

The melting temperature of Teflon® and Nafion® were taken into consideration in choosing this new value. According to the work of Starkweather,[122] the melting temperature of Nafion® increases linearly with the equivalent weight of the polymer. Given that the data

from this work estimates a melting temperature of 250°C for Nafion® with EW of 1100, an annealing temperature well below this was chosen. A second check was made as to the melting temperature of the Teflon® backbone, which is in the range of 327-370°C [32,122,123]. Given these temperature considerations, the new annealing temperature was raised to 195°C. A second temperature concern is the glass transition temperature. Page et al. give an excellent review that places this temperature for Nafion® in the range of 140-150°C[124]. With regard to time, it was decided to anneal the samples overnight (specifically 14.5 hr) and then allowed to cool for about 3 hr. It can be noted here that the Nafion® samples changed colors during this process. Hensley, et al. noted that the polymer color changed to amber. In both the preliminary testing given in Section 6.1.1.1 and the increased temperature and annealing time given here, the samples turned a black color. Also, the annealed samples here developed some wrinkles on the surface of the polymers. This is a possible source of problem in the electroding part of the DAP and will be discussed later.

With this updated procedure, ten dog bone samples were cut from Nafion® sheets. In addition to these ten samples, samples were cut for batch annealing with five of the dog bone samples. These samples are used for actual IPT fabrication. The final five dog bone samples were used for tensile testing for the as-received samples that would be made into the standard IPTs (i.e. no annealing treatment). This way, it is reasonable to assume that the average global stiffness measurements for the dog bones will be the same as it is for the Nafion® samples used to produce the annealed and regular IPTs for the sensing test. Care was taken to ensure that the samples were all cut in the same direction to one another. Further, all samples were cut from the same Nafion® sheet. The five dog bone samples were annealed according to the new

temperature and time, while five as-received samples were tested according to the specifications listed before in Table 6.1. The results for these tests are given in the following Table 6.3.

Table 6.3: As-received Moduli and Annealed Moduli under adjusted temperature and time conditions

Sample No.	As-received Modulus (MPa)	Annealed Modulus (MPa)
1	179	337
2	199	292
3	182	309
4	197	295
5	199	260
Average	191	299
Standard Deviation	9	25

The results in Table 6.3 address the concerns noted with the preliminary results listed in Table 6.2. First, a consistency in the as-received sample moduli is obtained by ensuring that the samples are all cut in the same direction. Second, by annealing the samples at a higher temperature for a longer amount of time, there is a consistent change in the modulus. This increase in the modulus over the as-received samples is attributed to an increase in semi-crystallinity. This was noted in the literature review of this chapter. For example, Hensley et al. note that cast Nafion® films will acquire crystallinity upon annealing. However, some samples investigated by Hensley et al. show that crystallinity is a function of the Nafion® thickness[114], while other works indicate in more general terms that annealing increases crystallinity[49,125].

Once that it was established that the annealing procedure would produce a significant difference in the stiffness of the Nafion®, the samples that were cut specifically for IPT creation were fabricated using the DAP[1]. The IPTs were fabricated using EmI-Tf and exchanged with the Na⁺ ions. Weight measurements of the Nafion® were taken twice during this procedure in order to establish the uptake of diluent. This data is given in the following table:

Table 6.4: Weight measurements of *annealed* Nafion® both before and after EmI-Tf uptake

Annealed samples prior to uptake	Weight (gm)	Average weight (gm)
1	0.6592	0.6564
2	0.6536	
Annealed samples after uptake		
1	0.7581	0.7586
2	0.7590	
%(w/w) per Equation 6.1	15.5	

Table 6.5: Weight measurements of *as-received* Nafion® both before and after EmI-Tf uptake

'As-received' samples prior to uptake	Weight (gm)	Average weight (gm)
1	0.6569	0.6603
2	0.6636	
'As-received' samples prior to uptake		
1	1.0567	1.055
2	1.0533	
%(w/w) per Equation 6.1	59.7	

The percent weight uptake, which is necessary for the modeling work is calculated by:

$$\% w/w = (weight_{after} - weight_{before}) / weight_{before} \quad 6.1$$

where $weight_{before}$ and $weight_{after}$ refers to the average measured weights before and after the EmI-Tf uptake step respectively.

6.1.2 Sensing Experimental Procedures

After the IPT samples were created, sensing measurements were taken for bending. The bending apparatus consists of an IPT cantilever that is displaced by a step input. The control for the step input was guided by programs written in LabView®. Further apparatus equipment included a circuit in order to measure the IPT output. The procedures for measuring the current output for these system is given in greater detail by Bilge Kocer in her publications[97].

As noted in the introduction of this chapter, the experimental work, in general, has been performed in cooperation with Bilge Kocer. Since the experimental sensing measurements were taken by Ms. Kocer, the results will therefore also be reported in her future publications.

6.2 MODELING: ANNEAL VS. ISOTROPIC

The purpose of the section is to connect the modeling methodology of this dissertation to the experimental methods and results presented in this chapter. The identified case is a sodium exchanged IPT with EmI-Tf as diluent. As shown in the experimental section, the primary variables between the annealed and as-received samples will be: semi-crystallinity of the samples, the amount of EmI-Tf uptake and the polymer backbone stiffness. As was discussed in

the literature background for this section, the semi-crystallinity is expected to increase for the annealed samples. This level of semi-crystallinity can be found by reversing the rule of mixtures and with the updated calculation of the fluid uptake discussed in Section 5.3.1.

Another item of note is that the difference in the amount of EmI-Tf uptake was measured and tabulated in Table 6.4 and Table 6.5. In terms of the polymer backbone stiffness, this difference in EmI-Tf uptake will necessarily affect the RIS predictions.

6.2.1 RIS Predictions

The first part of the model that must be updated to adequately reflect the process of annealing is the RIS model predictions. The model parameter that must be updated is the predicted size of the ionic domains, which are dependent upon diluent uptake. As discussed in Section 4.2, the fact that the ionic liquid EmI-Tf is used will alter the predicted strength of the polymer backbone.

The RIS model was adjusted accordingly to these concerns and the results on the polymer backbone strength is listed in Table 6.6.

Table 6.6: RIS results for Na⁺, EmI-Tf IPT

Cation Type	Na ⁺ <u>cubic</u>	
EmI-Tf volume fraction uptake	59.7%	15.5%
Young's Modulus (MPa)	7.81	1.30
Modulus standard deviation	0.29	0.04
KS statistic average	0.11	0.12

From these results, the increase in temperature is predicted to have a significant effect on the stiffness of the polymer backbone chains. Referring to the result given in Table 3.2, an IPT with Li⁺ and an uptake of 10% actually has an increase in predicted stiffness. However, the other major difference between these results is the diluent used. In Table 4.4, an IPT with Li⁺ ions, complete uptake of EmI-Tf diluent has a comparable stiffness to the Na⁺ sample listed here in Table 6.6, which shows that it is the temperature variable that plays a significant difference in the degradation of the polymer chain stiffness shown here for the Na⁺ sample with less uptake.

As noted in the introduction to this section, the semi-crystallinity of both the as-received and annealed samples can be backed out from the rules-of-mixtures approach. First, the rules-of-mixture approach is rewritten here for continuity (originally Equation 3.23)

$$E_{tot} = E_{bb}f_{bb} + E_{sc}f_{sc} + E_{cl}f_{cl} \quad 6.2$$

In Equation 6.2, the contribution of the clusters (*cl*) is neglected as there is no stiffness contribution to the overall polymer. The backbone volume fraction (f_{bb}) is rewritten in terms of the other volume fraction constituents:

$$E_{tot} = E_{bb}[1 - f_{sc} - f_p - f_{il}] + E_{sc}f_{sc} \quad 6.3$$

Equation 6.3 can be solved for in terms of known values for the unknown semi-crystalline volume fraction. Taking into account Section 5.3.1 for the experimental results given in Tables Table 6.3 and 6.4, the values used in this equation, along with the corresponding result is given in the following table.

Table 6.7: Semi-crystallinity estimates

	As-received	Annealed
E_{bb} (MPa)	7.8	1.3
f_p	0.25	0.25
f_{il}	0.51	0.134
E_{sc} (MPa)	5000	5000
E_{tot} (MPa)	191	299
f_{sc}	0.037	0.059

The results indicate that the semi-crystallinity goes up with the annealing.

6.2.2 Sensing Predictions

The sensing predictions were first investigated using the model built by Gao [65]. However, the results were not comparable to experiment. It was believed that the lack of variables to address semi-crystallinity and time was the main cause for the deficiency in the model. Therefore, a model is drawn up for the case of a bending IPT that considers both of these crucial variables. The method almost the same as Section 5.2, with the primary difference being the boundary conditions in the channel. However, in order to use the modeling framework used in Section 5.2, the initial model of the free energy, as produced by Marucci and Grizzutti must be re-evaluated[105].

6.2.2.1 Free-energy calculations

Un-deformed coordinates for a point at the edge of a channel can be given by:

$$r^2 = x^2 + y^2 + z^2 \quad 6.4$$

These variables are illustrated in Figure 6.1.

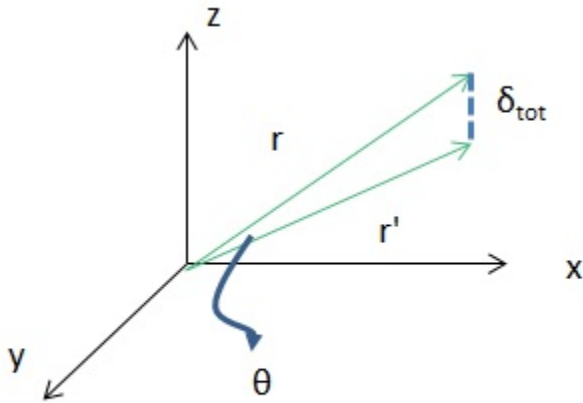


Figure 6.1: Illustration of bending deflection

With a small deformation, a cantilever will move from r to r' . The new coordinates can be given by:

$$x' = x \pm r \cos(\theta) \quad 6.5$$

$$y' = y \quad 6.6$$

$$z' = z \pm r \sin(\theta) \quad 6.7$$

The total deflection can be defined as:

$$\delta_{tot} = \sqrt{\delta_x^2 + \delta_z^2} \quad 6.8$$

Equation 6.8 can be expressed as a function of r and r' if the following figure is considered:

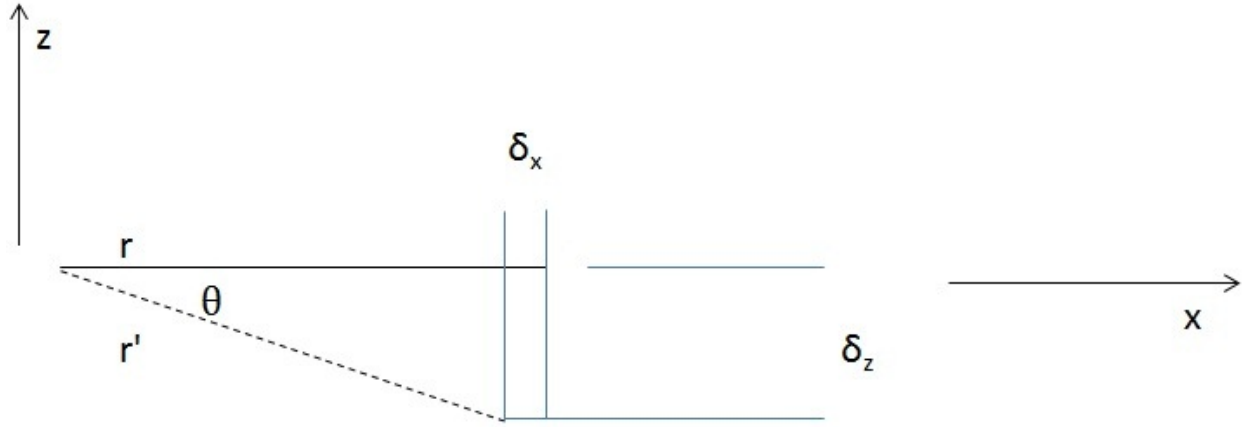


Figure 6.2: 2D deflection

The expressions for δ_x and δ_z can be defined by:

$$\delta_x = r - r' \cos(\theta) \quad 6.9$$

$$\delta_z = r' \sin(\theta) \quad 6.10$$

Substituting Equations 6.9 and 6.10 into Equation 6.8 and simplifying:

$$\frac{r'^2}{r^2} - \frac{2r'}{r} \cos(\theta)^2 - \delta_{tot}^2 + 1 = 0 \quad 6.11$$

While the solution to Equation 6.11 should be investigated in a more thorough way, the initial solution is via a quadratic equation. From this, two solutions are obtained; however, only the term with positive values will make sense. This is because in order to finally get the free energy of the polymer change, integration over the natural logarithm of the solution to Equation 6.11 is required. This means that the free energy can be determined:

$$\mathcal{A} = k_B T \int_0^l \ln\left(\frac{r'^2}{r}\right) dx \quad 6.12$$

Equation 6.12 is evaluated from this point just the same as if the strain input was a shear (that is, considering enthalpy and frequency of polymer chain jumps as outlined in Section 5.2.2). The variables in this equation are: k_b is the Boltzmann constant, T is temperature and l is length

of a channel. The next item of significant change between a shear deformation and a bending deformation is how the fluid flow needs to be considered.

6.2.2.2 Pressure response to bending deformation

The flow of the electrolyte for the case of bending is given by the following equation:

$$\rho(\partial \mathbf{u} / \partial t) = \mu \left(\partial^2 \mathbf{u} / \partial y^2 \right) - \frac{\partial P(x,t)}{\partial x} + \rho_e \nabla_y \varphi(x,y) \quad 6.13$$

The terms in Equation 6.13 match those given in Equation 5.19 (i.e. ρ is electrolyte density, μ is the electrolyte viscosity, ρ_e is charge density and $\varphi(x,y)$ is given by Equation 5.31). The objective in this section is to derive an expression for derivative of the pressure term: $P(x,t)$.

From the work of Gao[65], the maximum pressure gradient is given by:

$$\frac{\Delta p(x)}{l} = \frac{3E}{L_f^2} \delta \quad 6.14$$

where δ is the deflection of the cantilever. In the model developed here, it is assumed that the strain within the polymer region upon bending can be related to the imposed deformation and the length of the channel. This means the local deflection is:

$$\delta_{ch} = \epsilon_{ch} x \quad 6.15$$

where x is the cantilever length. The cantilever length x (defined by L_f by Gao and Weiland[63]) will be utilized for the value of δ because it is understood that the microscale channels will experience more strain than the channels closer to the free end.

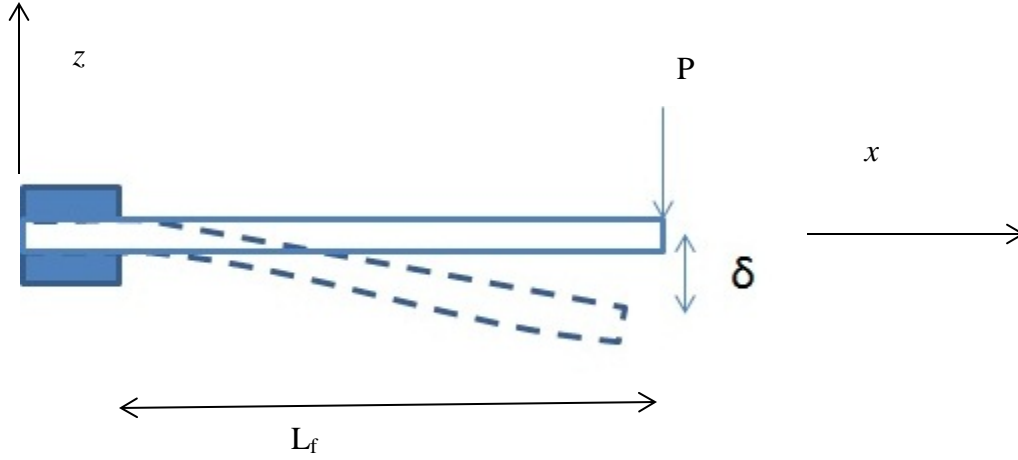


Figure 6.3: IPT cantilever, where δ is the macro displacement and P is an imposed force

Therefore, the maximum current will still take place at the deflected end of the cantilever and for this reason going forward, $x = L_f$. The strain, in turn can be represented in a viscoelastic sense by the relaxation modulus ($J(t)$) and the viscoelastic stress:

$$\delta_{ch} = J(t)\sigma(t)L_f \quad 6.16$$

Recall that the *local* properties of the ionic polymer are of interest in this dissertation, which is the reason why the deflection at the local level is under investigation. Keeping the 2N+1 model, the relaxation modulus becomes (for a step deflection input) [126]:

$$J(t) = \mathbf{1} * ([E_{sc} + \sum_{i=1}^N E_i \exp(-E_i t / \eta_i)])^{-1} \quad 6.17$$

Next, the stress is rewritten for the bending strain input:

$$\sigma(t) = (\epsilon_{est} f_{sc} E_{sc} + \sum_{i=1}^N (\epsilon_{est} f_{bb} E_i - f_{bb} E_i q_i m)) \quad 6.18$$

Substituting Equations 6.17 and 6.18 back into Equation 6.16 and subsequently the Equation, 6.14, an expression for the local pressure difference is given by:

$$\frac{\partial P(x,t)}{\partial x} = \frac{3E_i}{L_f} \left[\frac{1}{E_{sc} + \sum_{i=1}^N E_i \exp(-E_i t / \eta_i)} (\epsilon_{est} E_{sc} + \sum_{i=1}^N (\epsilon_{est} f_{bb} E_i - f_{bb} E_i q_i m)) \right] \quad 6.19$$

There are two significant qualifications on the expression given by (6.19). First, the assumption about this particular pressure gradient is that it occurs at the tip of the IPT cantilever and hence would be a maximum pressure gradient. Considering channels closer to the clamped position, the pressure gradient given by 6.19 would decrease.

The second point to consider is the term ϵ_{est} . This is an estimation of the strain induced into a channel wall. A more thorough investigation would include an iterative procedure as it is clear that the stress and strain are interdependent according to Equations 6.15 and 6.16. However, it was found that with an increase in time, the value $\epsilon_{ch} \rightarrow \epsilon_{est}$. This estimated strain is simply taken to be a proportion and must be non-dimensionalized with respect to the size of the cantilever IPT:

$$\epsilon_{est} = \frac{\delta_{tot}}{L_f} \frac{len}{L_f} \tag{6.20}$$

This equation is a similar method that was considered for the shearing deflection input in Chapter 4.0.

6.2.2.3 Electrolyte velocity

The method to develop an expression for the electrolyte velocity is similar to the method given by Section 5.2.3.3. The same non-dimensionalization was applied in this section. The objective is to solve Equation 6.13. The spatial boundary conditions are given by the no-slip conditions [63]. In the time domain, it is assumed that the electrolyte starts from rest. A solution form is assumed:

$$\mathbf{u}(\mathbf{y}, t) = \sum_{n=1}^{\infty} \mathbf{E}_n(t) \phi_n(\mathbf{y}) \tag{6.21}$$

This equation can be developed into a solution by the eigenvalue expansion method. First, the associated eigenvalue problem is given by $Y'' + \lambda Y = 0$. The solution to this problem is given by the form:

$$\phi(y) = \sum_{n=1}^{\infty} c_n \sin(n\pi y / 2h) \quad 6.22$$

The following function is defined and solved by a simple Simpson's Method:

$$Q_n(t) = \frac{1}{h} \int_0^{2h} \left[\rho_e \nabla_y \psi(x, y) - \frac{\partial P(x, t)}{\partial x} \right] \sin(n\pi y / 2h) dy \quad 6.23$$

Once Equation 6.22 is solved, then the term $E_n(t)$ can be solved from Fourier expansion methods described in math texts for eigenfunction expansion methods[127]:

$$E_n(t) = \left[c_n + \frac{1}{v} \int_0^t \exp\left(\frac{n\pi y \tau}{2h v}\right) Q_n(\tau) d\tau \right] \exp\left(-\frac{n\pi y t}{2h v}\right) \quad 6.24$$

The variable c_n drops out from Equation 6.23 due to the temporal initial conditions of starting from rest. The final form of the velocity varies from the shear case due to these initial and boundary condition considerations. The final expression for the velocity is given by substituting Equations 6.23 and 6.21 into Equation 6.20. The steps of the computation are carried out in the same manner as described in Section 5.2.4.

6.3 DISCUSSION OF RESULTS

The objective of this section is to compare the experimental results from Section 6.1 and the modeling results from Section 6.2.

6.3.1 Experimental Results

Preliminary experimental results are given in the following figures:

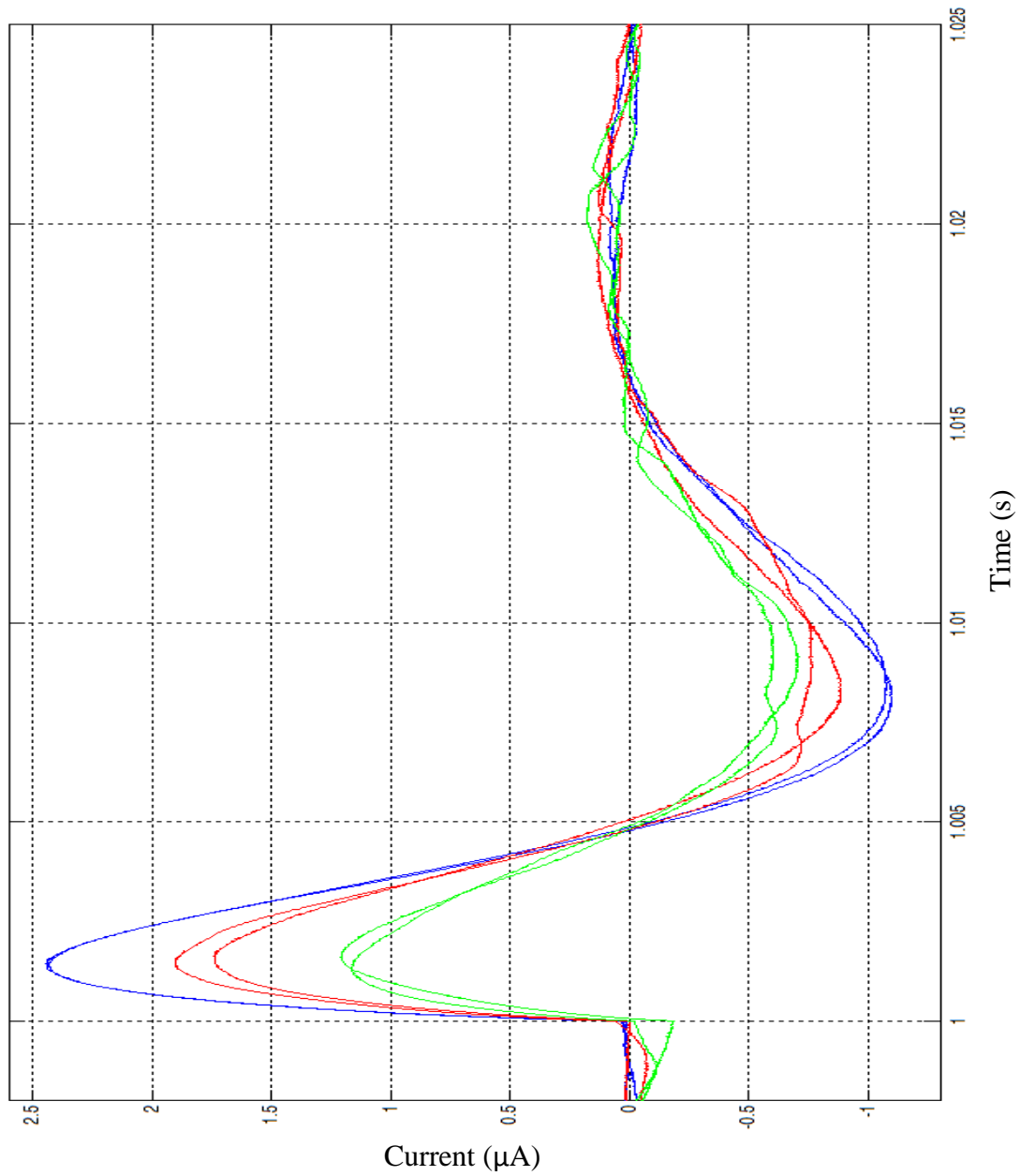


Figure 6.4: Sample 1a, without annealing. Deflection values: Blue = 20 mm, Red = 15 mm, Green = 10 mm[128]

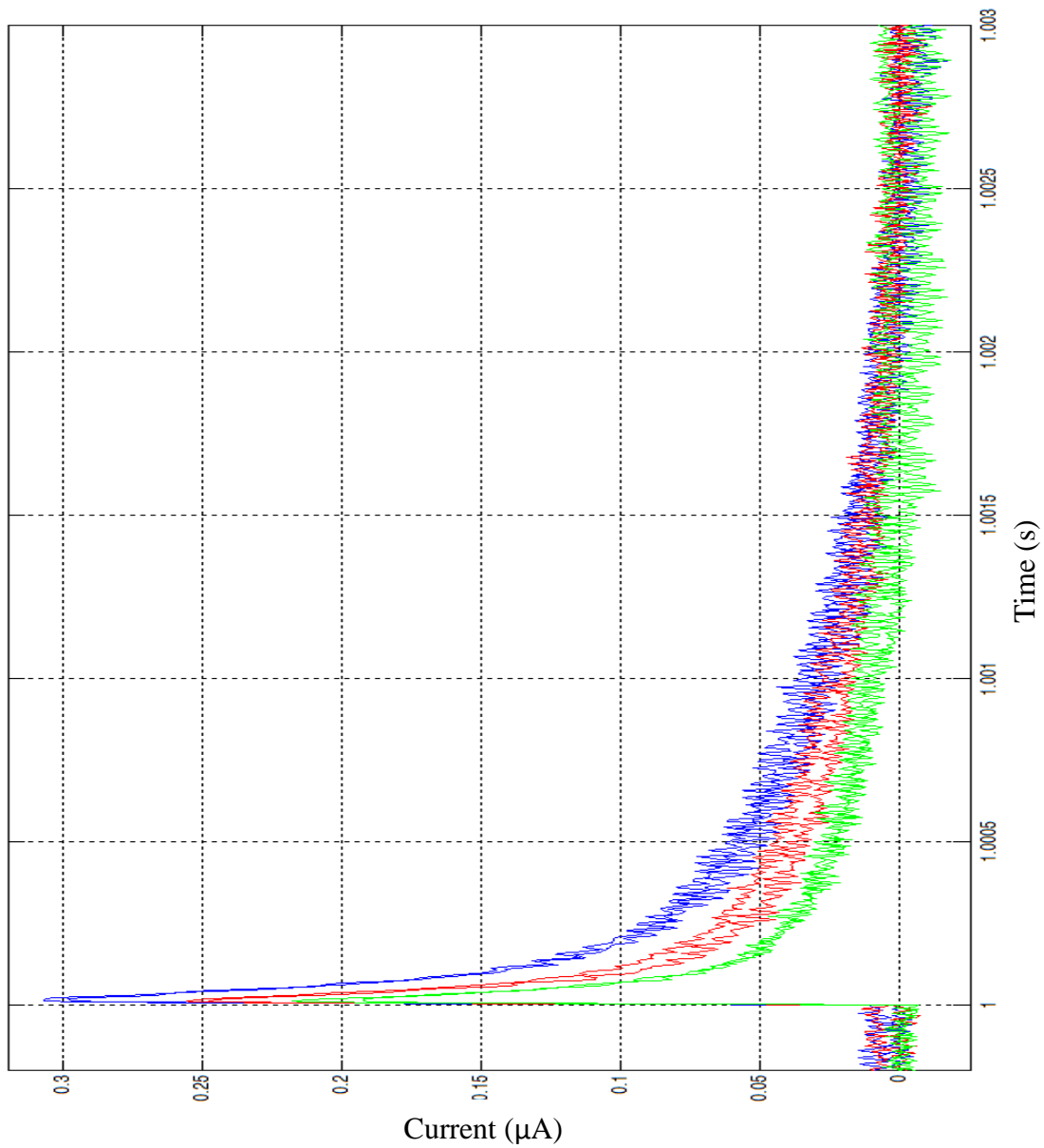


Figure 6.5: Sample 1b, with annealing. Deflection values: Blue = 20 mm, Red = 15 mm, Green = 10 mm[128]

Experimentally, there are a few differences. First, the as-received IPT sample has the characteristic current reversal that was seen in previous experimental results presented by Bilge Kocer[97]. This reversal is not present in the annealed sample. The second point of interest about these two different IPTs (besides the peak current values) is the speed of signal decay. The IPT with the annealed base IPT decreases very rapidly in Figure 6.6.

6.3.2 Modeling Results

The first set of model results is given for the as-received Nafion®-based IPT:

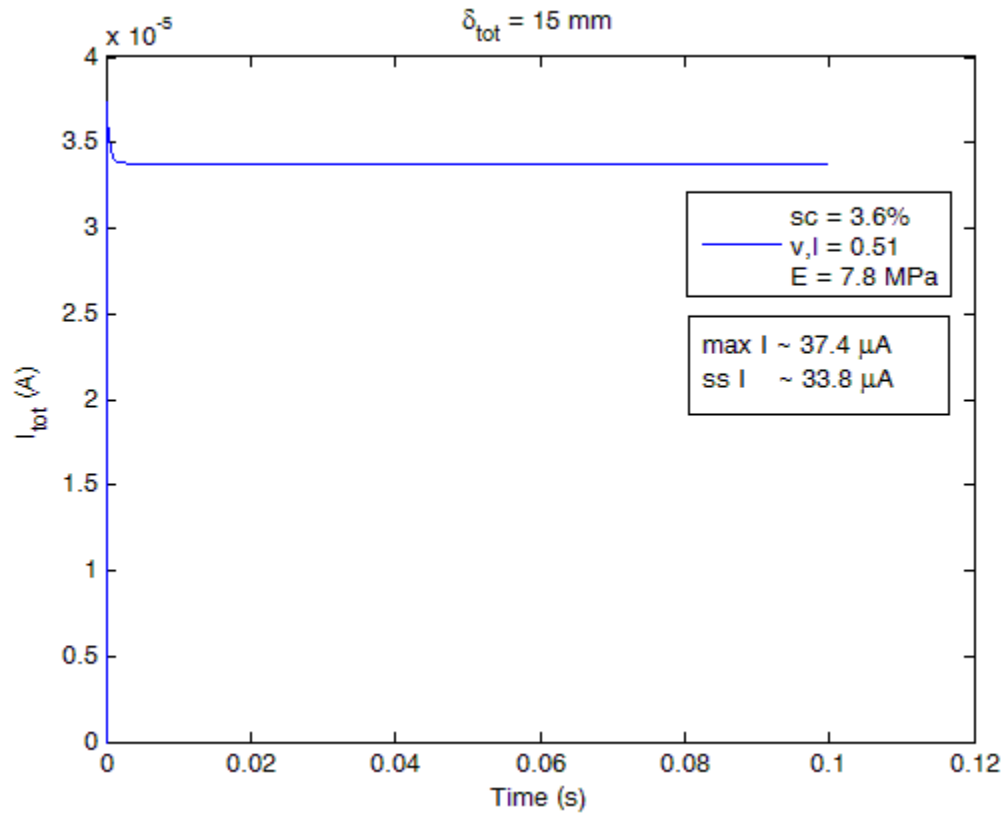


Figure 6.6: As-received Nafion®, IPT sensing results for step deflection input of 15 mm

The second set of model results is given for the annealed Nafion®-based IPT:

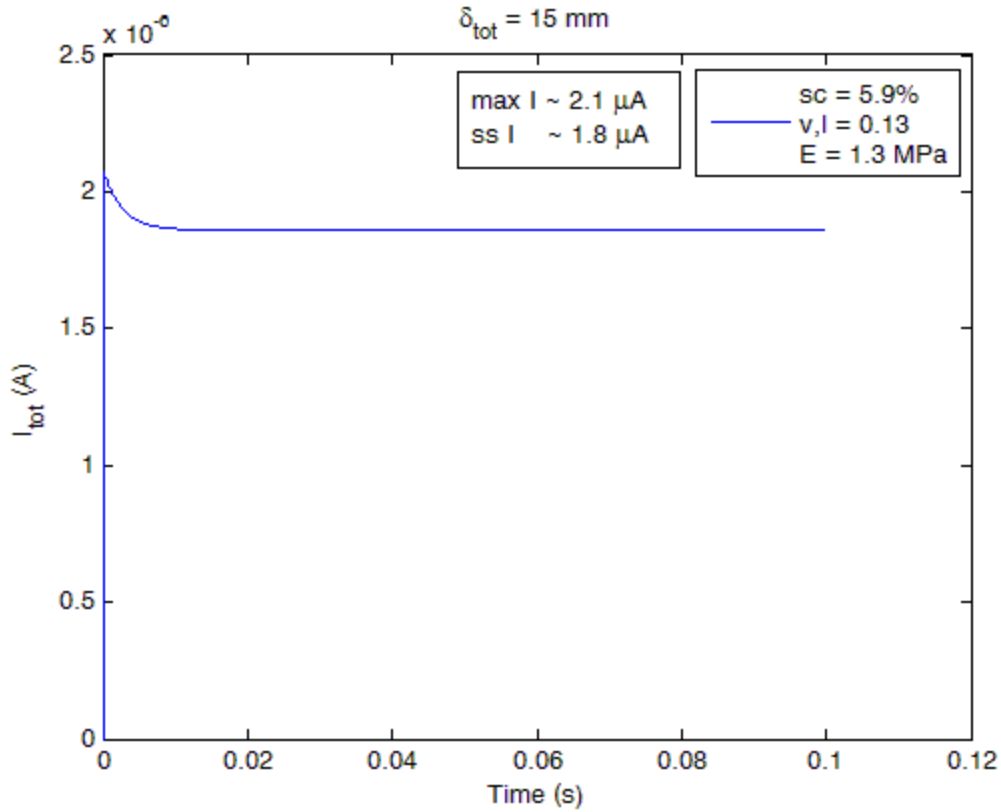


Figure 6.7: Annealed Nafion®, IPT sensing results for step deflection input of 15 mm

For a complete comparison, the varied variables are collected into one table, including the results of both the models and the experimental measurements.

Table 6.8: Complete summary of modeling and experimental work between the as-received and annealed polymer-based IPTs (for the specific case of the deflection = 15 mm)

$\delta_{tot} = 15 \text{ mm}$	As-Received		Annealed	
	Model	Experiment	Model	Experiment
Semicrystallinity (%)	3.7		5.9	
Electrolyte volume Fraction (%)	0.52		0.13	
Backbone Modulus (MPa)	7.8		1.3	
Predicted, steady state current (μA)	33.7	~1.75	2.7	~0.25

The most important result is the last line of Table 6.8. One way to look at the results in this table is to compare the difference in current output between the as-received samples and the annealed samples. That is, define the ratio as:

$$\mathbf{Ratio} = \frac{I_{as-received}}{I_{annealed}} \quad 6.25$$

Comparing these ratios yields the following information in Table 6.9.

Table 6.9: Comparison of ratio trends between experiment and model

	Ratio
Experimental	7
Model	17.7

While there shows some difference in the magnitude of the predicted change, there are two important points to note. First, the predicted order of magnitude of the results is in agreement. This is important because the stress induced on the IPT is pressure-based and not shearing, showing the validity of this model under various stress conditions, which is one of the ultimate goals of this work. The second important point to note is that the model can capture the effect of the engineered polymers. That is, the direction of the trend in the predicted current change is changed in the same direction.

These results are very promising. These results show the importance of the variables: semicrystallinity, electrolyte volume fraction and backbone modulus. Also, please note that these calculations are including the volume average of the rotated channels that was described Chapter 4.0. The results are given in terms of the steady state results because of the discussion regarding the differences in the strain that is discussed at the end of Section 6.2.2.2.

Clearly, a significant question arises from the expected lack of decay in the current signal of the modeling results. This indicates that the time-dependent, *local* effects are important; the models clearly need more work to incorporate more thorough considerations of this behavior. A further question arises to assessing the microstructure under annealed conditions. Clearly, more thorough experiments, such as SEM results are warranted. However, the assumptions made in modeling this experiment are indicative of experimental trends. For example, annealing is believed to increase the distance between clusters and packing of transport regions[129]. Further, several literature reports increase in crystallinity of polymers subjected to annealing [49] and further that the annealing decreases the order of the side-chain packing, giving rise to more crystalline regions [124]. Therefore, the estimates on the changes in the microstructure are within reason.

A second possible explanation that can address the differences between the experimental and modeling work is in the setup of the experimental apparatus. Reviewing the modeling results and the experimental results, the speed of the signal decay varies between the results. Despite the focus in this work on the microscale effects, some other phenomena may be present in the experimental setup which can explain the differences in transient response. For example, there is a possibility of leakage current in the apparatus. Such leakage current would be classified as ac leakage current, arising from possible capacitance in the circuit board [130]. Further experimental research should be conducted to investigate if improved apparatus design can isolate this as a probable cause for the transient signal.

6.4 CHAPTER SUMMARY

This chapter provided some experimental validation of the streaming potential model presented in this dissertation. Since the main objective of this work is to develop a modeling framework for mechanically robust IPTs, the Nafion® membranes were subjected to annealing in order to increase the polymer strength. An experiment was performed with two primary parts. First, an annealing procedure was carried out to increase the stiffness of polymer samples. Secondly, IPT sensing experiments in bending were performed. The modeling framework was then adapted to scenario where an IPT is bent in order to obtain the electrical current signal, specifically the inclusion of a pressure gradient. The framework included the modeling considerations detailed in Chapters 3-5. While the results still require work to capture a complete picture of transient effects, the final steady-state results show good agreement.

7.0 CONCLUSION

In this dissertation, the overall objective was to explain the fundamental physics of IPT sensing as viewed through the streaming potential theory. This required a detailed understanding of several interacting variables particularly: the polymer backbone strength, the type of diluent used and cation type. Foundational science to build the relation between these variables and the streaming potential hypothesis included important understandings of multi-scale modeling theory. In addition, the mode of IPT sensing is a significant factor in this work. The objective was to build upon previous work of streaming potential theory applications to IPT in bending and apply this IPT sensing in shear. However, the interplay that was found with microscale phenomena such as diluent flow, polymer backbone stiffness and semicrystallinity enabled further insight into IPT sensing in bending. Major chapter conclusions will be noted in the following paragraphs.

The work in Chapter 3 introduced RIS theory and the use of this theory to model the variable of polymer backbone stiffness. Various scenarios were investigated in order to establish a baseline. Next, the model was used to predict how polymer processing effects (such as extrusion and drawing) would in turn affect the polymer backbone stiffness. With a preliminary look into the predicted IPT sensing response in bending based on previous work, it was found that utilization of the polymer backbone stiffness instead of the global polymer backbone stiffness gave a better prediction of the experimentally observed sensing results.

The work in Chapter 4 turned in detail to building a model to predict the IPT sensing under shear deformation. The model used the ANSYS® computational package in order to establish how ionic channel alignment with the IPT sheared surface affected expected current output. With a mathematical equation that could distribute rotated ionic channels in a three-dimensional space, the predicted current for perfectly aligned channels reduced the current prediction from an order of mA to an order of μA for the case of distributed ionic channel alignment. This μA result was on a similar magnitude to preliminary shear experiments found in literature. However, there was still a significant difference in not only the steady-state magnitude of the expected current, but also how the current output was predicted respond over time. This required further investigation of the microscale phenomena and investigation of the time-dependent properties at this level. This was the work pursued in Chapter 5.

In Chapter 5 the foundation for a viscoelastic framework was laid in order to look at time-dependent properties of the IPT. A “ $2N+1$ ” model was constructed, considering the polymer backbone strength, the semicrystallinity volume fraction and diluent effects. The model was run for various scenarios combining different diluent, cation types and shear strain input values. These results were then considered in context of the three-dimensional ionic channel rotation distribution found in Chapter 4. The results show that the magnitude of the predicted output current was reduced to a value still in terms of μA and modeled an apparent decay in the current.

Finally, the work in Chapter 6 was an effort for some experimental work to test the predictive capabilities for the model. Prior comparison work between model and experiments has shown promise in that the predictive trends matched experimental trends when particular variables were altered. The eventual comparison of experimental and modeling work further

strengthened the hypothesis of streaming potential hypothesis to the fundamental, local effects of the IPT. As the Nafion® base was altered by an annealing process; the streaming potential theory still captured very well the expected magnitude of the streaming current.

This work in Chapter 6 opens up more questions in terms of the kinetics of semicrystalline formation and how this can be controlled to assist IPT sensing instead of hindering it. These questions will contribute to the section on future work.

7.1 PROCEDURE IMPLEMENTATION

The purpose of this section is to incorporate into a summary how to apply this research into constructing an IPT model beginning with the work in Chapter 3 through Chapter 5. This strategy could be applied to any ionic polymer-based IPT.

1. Begin with the chemical formula of the polymer backbone chain. Important parameters in this step include: any significant temperature differences due to fabrication such as annealing, bond lengths and valence angles. Further parameters to include within the model during the RIS stage include the expected uptake of diluent, as well as the type of cation exchanged. An expected morphology for the ionic transport regions should be assumed *a priori*, such as parallel channels.
2. After the RIS model yields an expected polymer backbone modulus, the density and viscosity of the diluent are the required inputs in order to model the expected current. Also, a further requirement for the model is the expected level of semicrystallinity. This can be achieved from the base polymer by either tensile

testing, as described in Chapter 6, or via Scanning Electron Microscopy. At this point, another important parameter that is required is the size of the expected IPT, such as length, width and electrode layer thickness.

3. With the information gleaned from step 2, the expected current from an IPT can be gleaned. This information would require a stress input, whether it is pressure or shear based.

An advantage to using this model is that it primarily focuses on controllable, microscale phenomena. Further, by not relying on experiments with fabricated IPTs, but only requiring some base polymer characterization, this model can make precise predictions as to the expected current. This model can assist in a timely fashion ways to engineer an IPT both mechanically and electrically.

7.2 CONTRIBUTIONS

The major contributions of this work are noted as follows:

1. Assessed the importance of the local stiffness in the prediction of IPT sensing current.
2. Developed modeling connection between the streaming potential theory and IPT sensing in shear.
3. Quantified the effects of ionic transport morphology, indicating that ways to increase the current output in shear would be to engineer ionic transport channels in a direction parallel to the surface of the IPT. This would increase the current by 99%.

4. Established a model that has successfully predicted the trends in an engineered IPT, specifically that the model predicted a decrease in current with an increase in mechanical strength.
5. Showed the strength of the streaming potential hypothesis in predicting the current output is effective for sensors in both shear and pressure driven stresses.
6. Established modeling framework for the study of local, microscale phenomena that can affect the time-dependent behavior of IPT sensing.

7.3 FUTURE WORK

Based upon the work done in this dissertation, some major theoretical questions that should be resolved in the future include:

1. Investigate how the strain input, either step or dynamic, impacts the polymer backbone stiffness. Iterative RIS methods are a possible method to incorporate the evolution of polymer stiffness.
2. Temperature can play a major role in coupling of the polymer stiffness and fluid dynamic effects. Incorporating energy terms based on temperature differences and thermal effects can be instructive.
3. Incorporate time dependent modeling of semicrystallinity formation kinetics and determine how this affects IPT sensing.

APPENDIX A

DIRECTIONAL STREAMING CURRENT PREDICTIONS

The following table yields the streaming prediction currents from

$$I_{tot} = \frac{3C v_f f_{cl} w \beta^2 a^2 \rho_e E}{2 \phi \mu L} \delta_f \quad 3.24$$

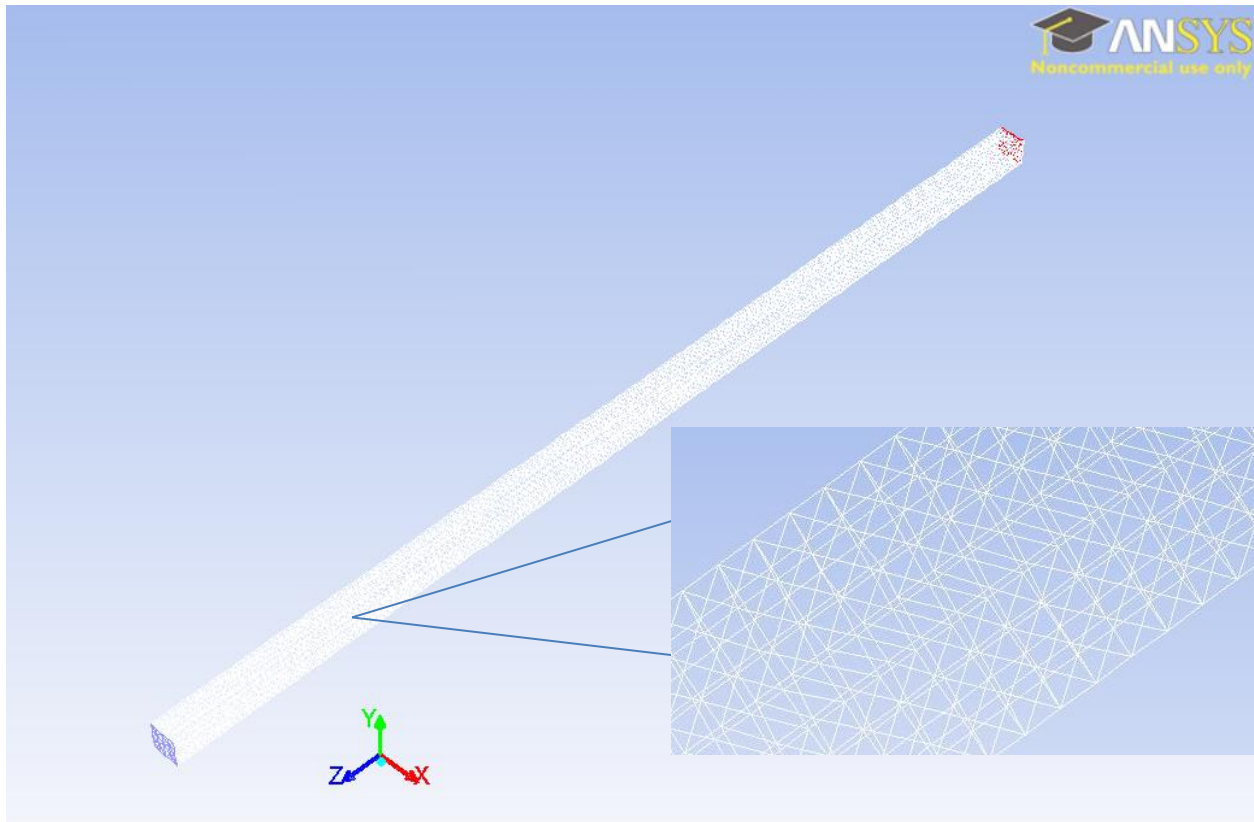
Table A.7.1: Anisotropic streaming current predictions

Direction	Modulus (MPa)	Current (mA)	Modulus (MPa)	Current (mA)
<u>Sphere</u>	$\delta = 1.1$		$\delta = 0.8$	
x	13.0	1.387E-21	22.5	2.401E-21
y	13.0	1.387E-21	22.0	2.348E-21
z	13.6	1.451E-21	20.8	2.22E-21
<u>Cylinder</u>	$\delta = 1.3$		$\delta = 1.2$	
x	12.6	2.71E-17	31.5	6.77E-17
y	12.6	2.71E-17	26.0	5.59E-17
z	18.3	3.93E-17	33.0	7.09E-17

APPENDIX B

MESH FIGURES FROM CHAPTER 4

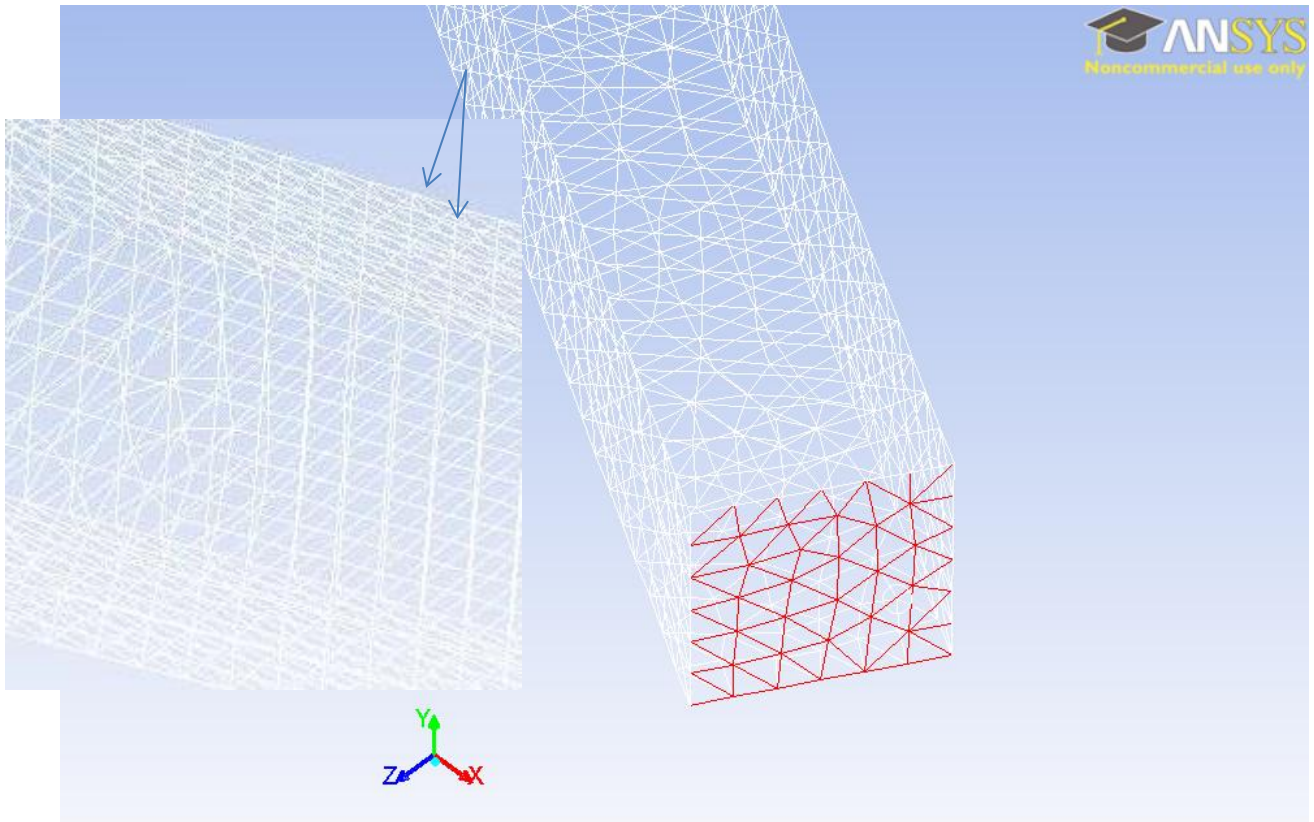
The following meshes were created in ANSYS using a tetrahedron type mesh, as discussed in Chapter 4. Looking more closely at the meshes the only difference between the various channels at each of the different angles is in the refinement of the element size. The reason for that is based on the mesh verification to ensure the simulation results weren't affected by mesh quality.



Mesh (Time=2.5000e-04)

Apr 17, 2013
ANSYS FLUENT 14.0 (3d, dp, pbns, vof, lam, transient)

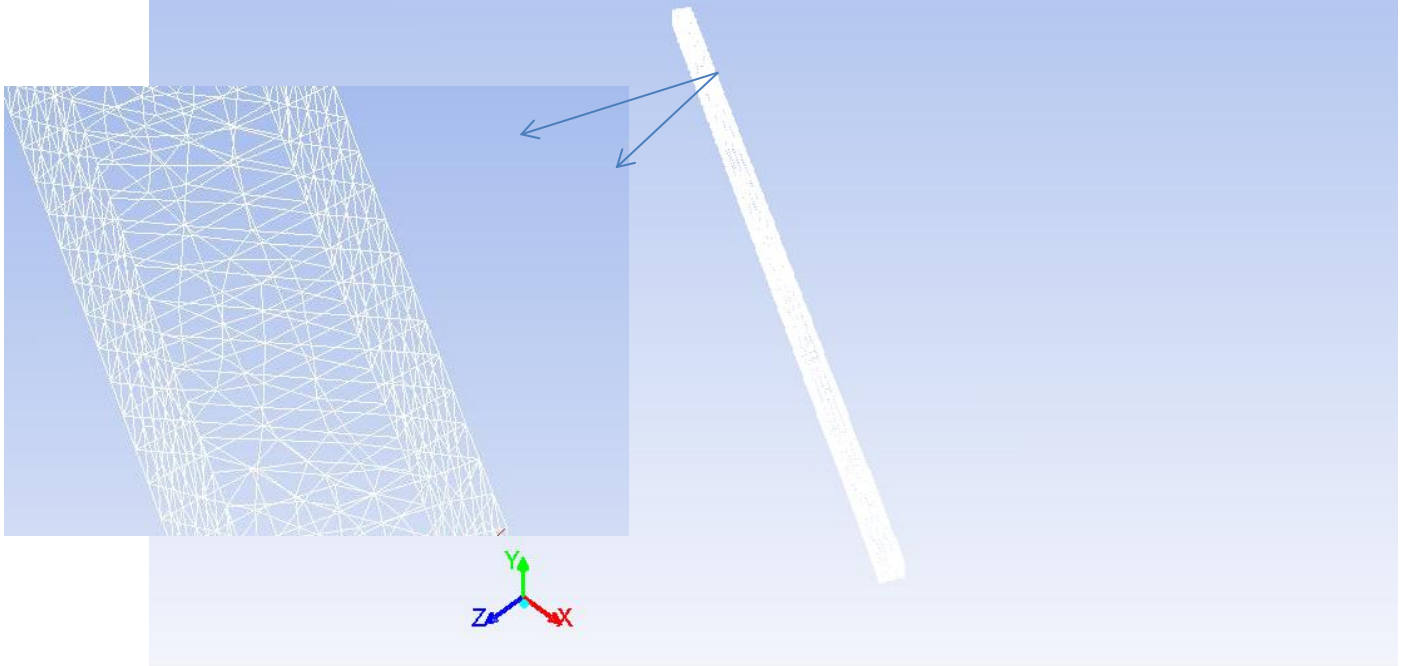
Figure B.1: Picture of parallel channel mesh used in the generation of current predictions in Chapter 4.



Mesh (Time=3.1250e-05)

Apr 26, 2013
ANSYS FLUENT 14.0 (3d, dp, pbns, vof, lam, transient)

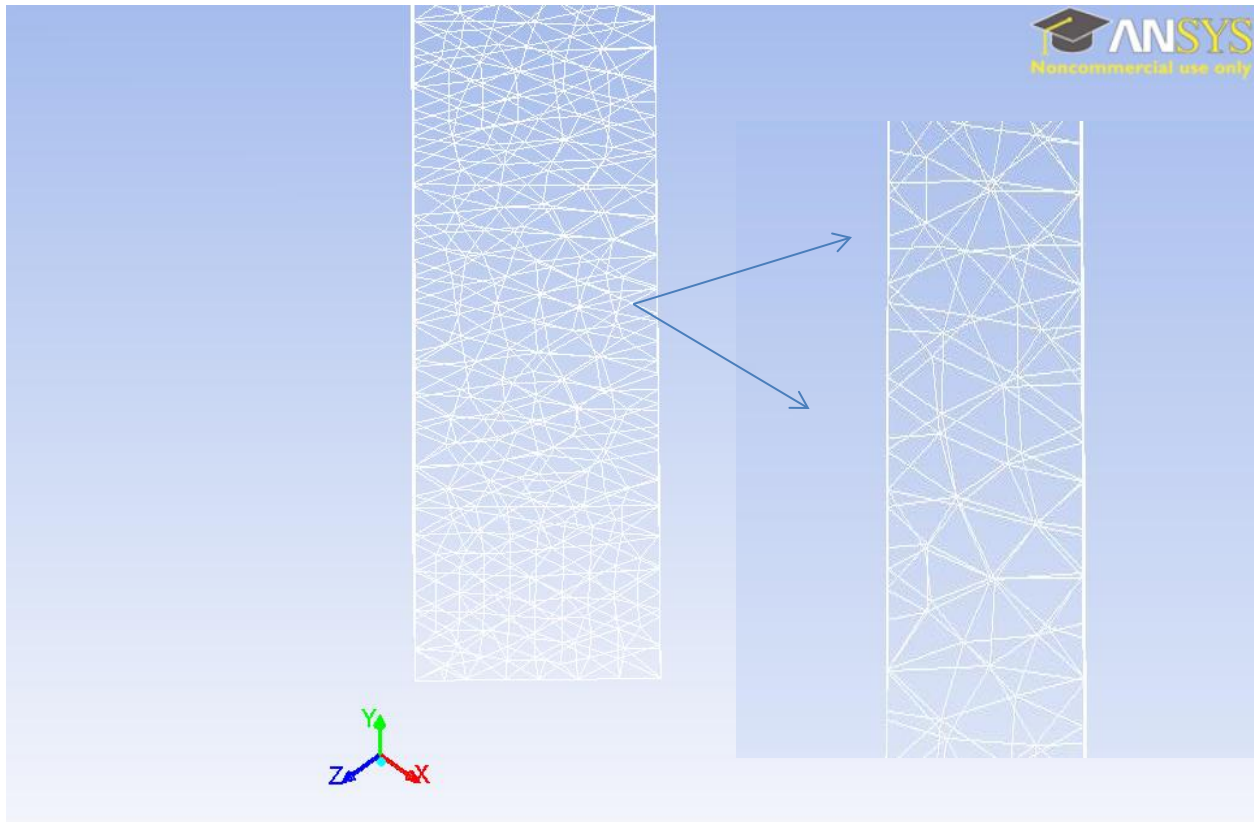
Figure B.2: Picture of mesh rotated $\pi/4$ in the xy plane



Mesh

Apr 17, 2013
ANSYS FLUENT 14.0 (3d, dp, pbns, lam)

Figure B.3: Picture of channel, rotated in direction of $\pi/3$ with regard to model presented in Chapter 4.



Mesh

Apr 17, 2013
ANSYS FLUENT 14.0 (3d, dp, pbns, lam)

Figure B.4: Picture of channel, rotated in direction of $\pi/4$ with regard to model presented in Chapter 4. This rotation is with respect to the xz axis.

BIBLIOGRAPHY

- [1] Akle, B. J., Bennett, M. D., Leo, D. J., Wiles, K. B. & McGrath, J. E. Direct assembly process: a novel fabrication technique for large strain ionic polymer transducers. *Journal of Materials Science* **42**,(16) 7031-7041 (2007).
- [2] Shahinpoor, M. & Kim, K. J. Ionic polymer–metal composites: III. Modeling and simulation as biomimetic sensors, actuators, transducers, and artificial muscles. *Smart Materials and Structures* **13**,(6) 1362-1388 (2004).
- [3] Konyo, M., Konishi, Y., Tadokoro, S. & Kishima, T. in *Proceedings of SPIE*. 307.
- [4] Etebari, A. Recent Innovations in Wall Shear Stress Sensor Technologies.(Journal Article) 22.
- [5] Farinholt, K. M., Pedrazas, N. A., Schluneker, D. M., Burt, D. W. & Farrar, C. R. An Energy Harvesting Comparison of Piezoelectric and Ionically Conductive Polymers. *Journal of Intelligent Material Systems and Structures* **20**,(5) 633 (2009).
- [6] Bonomo, C., Fortuna, L., Giannone, P., Graziani, S. & Strazzeri, S. Motion Sensors and Actuators Based on Ionic Polymer-Metal Composites. *Device Applications of Nonlinear Dynamics*,(Journal Article) 83-99 (2006).
- [7] Akle, B. J., Leo, D. J., Hickner, M. A. & McGrath, J. E. Correlation of capacitance and actuation in ionomeric polymer transducers. *Journal of Materials Science* **40**,(14) 3715-3724 (2005).
- [8] Shahinpoor, M. & Kim, K. J. Ionic polymer-metal composites: I. Fundamentals. *Smart Materials and Structures* **10**,(4) 819-833 (2001).

- [9] Kundu, S., Simon, L. C., Fowler, M. & Grot, S. Mechanical properties of Nafion™ electrolyte membranes under hydrated conditions. *Polymer* **46**,(25) 11707-11715 (2005).
- [10] Robello, D. R. *Introduction to Polymer Chemistry: Crystalline and Amorphous Polymers*, <<http://chem.chem.rochester.edu/~chem421/cryst.htm>> (2002).
- [11] in *Encyclopedia Britannica* (2013).
- [12] Mauritz, K. A. & Moore, R. B. State of Understanding of Nafion. *Chemical reviews* **104** 4535-4586 (2004).
- [13] Nemat-Nasser, S. Micromechanics of actuation of ionic polymer-metal composites. *Journal of Applied Physics* **92**, (Journal Article) 2899 (2002).
- [14] Hsu, W. Y. & Gierke, T. D. Elastic theory for ionic clustering in perfluorinated ionomers. *Macromolecules* **15**,(1) 101-105 (1982).
- [15] Weiland, L. M. & Akle, B. J. Ionic Polymer Transducers in Sensing: The Streaming Potential Hypothesis. *Smart Structures and Systems* **6**,(4) (2010).
- [16] Rubatat, L., Gebel, G. & Diat, O. Fibrillar structure of Nafion: Matching Fourier and real space studies of corresponding films and solutions. *Macromolecules* **37**,(20) 7772-7783 (2004).
- [17] Termonia, Y. Nanoscale modeling of the structure of perfluorosulfonated ionomer membranes at varying degrees of swelling. *Polymer* **48**,(5) 1435-1440 (2007).
- [18] Roche, E. J., Pineri, M. & Duplessix, R. Phase separation in perfluorosulfonate ionomer membranes. *Journal of Polymer Science: Polymer Physics Edition* **20**,(1) 107-116, doi:10.1002/pol.1982.180200109 (1982).
- [19] Starkweather Jr, H. W. & Chang, J. J. Water relaxation in perfluorosulfonate ionomers. *Macromolecules* **15**,(3) 752-756 (1982).
- [20] Elliott, J. A., Hanna, S., Elliott, A. M. S. & Cooley, G. E. The swelling behaviour of perfluorinated ionomer membranes in ethanol/water mixtures. *Polymer* **42**,(5) 2251-2253 (2001).

- [21] Litt, M. Polymer Preprints: Papers Presented at the San Francisco, California, Meeting ACS. *BM Culbertson, Ed* **38**,(Journal Article) 80 (1997).
- [22] Gierke, T. D., Munn, G. E. & Wilson, F. C. The morphology in nafion perfluorinated membrane products, as determined by wide- and small-angle x-ray studies. *Journal of Polymer Science Polymer Physics Edition* **19**,(11) 1687-1704 (1981).
- [23] Kreuer, K. D. On the development of proton conducting polymer membranes for hydrogen and methanol fuel cells. *Journal of Membrane Science* **185**,(1) 29-39 (2001).
- [24] Schmidt-Rohr, K. & Chen, Q. Parallel cylindrical water nanochannels in Nafion fuel-cell membranes. *Nature Materials* **7**,(1) 75 (2007).
- [25] Matthews, J. L., Lada, E. K., Weiland, L. M., Smith, R. C. & Leo, D. J. Monte Carlo simulation of a solvated ionic polymer with cluster morphology. *Smart Materials and Structures* **15**,(1) 187 (2006).
- [26] Nemat-Nasser, S., Zamani, S. & Tor, Y. Effect of solvents on the chemical and physical properties of ionic polymer-metal composites. *Journal of Applied Physics* **99**,(Journal Article) 104902 (2006).
- [27] Farinholt, K. & Leo, D. J. Modeling of electromechanical charge sensing in ionic polymer transducers. *Mechanics of Materials* **36**,(5-6) 421-433 (2004).
- [28] Sadeghipour, K., Salomon, R. & Neogi, S. 'Development of a Novel Electrochemically Active Membrane and 'Smart Material Based Vibration Sensor/Damper. ''*Smart Materials and Structures* **1**,(2) 172-179 (1992).
- [29] Shahinpoor, M., Bar-Cohen, Y., Simpson, J. O. & Smith, J. Ionic polymer-metal composites (IPMCs) as biomimetic sensors, actuators and artificial muscles—a review. *Smart Mater.Struct* **7**,(6) (1998).
- [30] Bennett, M. D. & Leo, D. J. Ionic liquids as stable solvents for ionic polymer transducers. *Sensors & Actuators: A.Physical* **115**,(1) 79-90 (2004).

- [31] Nemat-Nasser, S. & Wu, Y. Comparative experimental study of ionic polymer–metal composites with different backbone ionomers and in various cation forms. *Journal of Applied Physics* **93** 5255 (2003).
- [32] Kawano, Y., Wang, Y., Palmer, R. A. & Aubuchon, S. R. Stress-Strain Curves of Nafion Membranes in Acid and Salt Forms. *Polímeros* **12** 96-101 (2002).
- [33] Kim, K. J. & Shahinpoor, M. Ionic polymer-metal composites: II. Manufacturing techniques. *Smart Materials and Structures* **12**,(1) 65-79 (2003).
- [34] Farinholt, K. M. & Leo, D. J. in *Proceedings of SPIE*. 1.
- [35] Bar-Cohen, Y. *Electroactive Polymer (EAP) Actuators as Artificial Muscles: Reality, Portential and Challenges*. (SPIE Press, 2001).
- [36] Nemat-Nasser, S. & Thomas, C. W. Ionomeric polymer–metal composites. *Electroactive Polymer (EAP) Actuators as Artifical Muscles. Reality, Potential, and Challenges*, SPIE Press, Washington,(Journal Article) (2001).
- [37] Zangrilli, U., Gao, F. & Weiland, L. M. Implications of multiscale modeling on sensing predictions in Nafion. *Smart Materials and Structures* **19**,(Journal Article) 094011 (2010).
- [38] Park, J. K. & Moore, R. B. Influence of Ordered Morphology on the Anisotropic Actuation in Uniaxially Oriented Electroactive Polymer Systems. *ACS Applied Materials & Interfaces* **1**,(3) 697-702 (2009).
- [39] Weiland, L. M., Lada, E. K., Smith, R. C. & Leo, D. J. Application of rotational isomeric state theory to ionic polymer stiffness predictions. *JOURNAL OF MATERIALS RESEARCH-PITTSBURGH THEN WARRENDALE-* **20**,(9) 2443 (2005).
- [40] Gao, F. & Weiland, L. M. A multiscale model applied to ionic polymer stiffness prediction. *Journal of Materials Research* **23**,(3) 833-841 (2008).
- [41] Flory, P. J. *Principles of Polymer Chemistry*. (Cornell University Press, 1953).

- [42] Kumar, A. S. & Shankar, V. Instability of high-frequency modes in viscoelastic plane Couette flow past a deformable wall at low and finite Reynolds number. *Journal of Non-Newtonian Fluid Mechanics* **125**,(2) 121-141 (2005).
- [43] Porfiri, M. An electromechanical model for sensing and actuation of ionic polymer metal composites. *Smart Materials and Structures* **18**,(Journal Article) 015016 (2009).
- [44] Bonomo, C., Fortuna, L., Giannone, P., Graziani, S. & Strazzeri, S. A model for ionic polymer metal composites as sensors. *Smart Materials and Structures* **15**,(Journal Article) 749-758 (2006).
- [45] Newbury, K. M. & Leo, D. J. Electromechanical modeling and characterization of ionic polymer benders. *Journal of Intelligent Material Systems and Structures* **13**,(1) 51 (2002).
- [46] Newbury, K. M. & Leo, D. J. Linear electromechanical model of ionic polymer transducers-part ii: experimental validation. *Journal of Intelligent Material Systems and Structures* **14**,(6) 343 (2003).
- [47] Asaka, K. & Oguro, K. Bending of polyelectrolyte membrane platinum composites by electric stimuli Part II. Response kinetics. *Journal of Electroanalytical Chemistry* **480**,(1-2) 186-198 (2000).
- [48] De Gennes, P. G., Okumura, K., Shahinpoor, M. & Kim, K. J. Mechanoelectric effects in ionic gels. *EPL (Europhysics Letters)* **50**,(Journal Article) 513-518 (2000).
- [49] Deng, Z. D. & Mauritz, K. A. Dielectric relaxation studies of acid-containing short-side-chain perfluorosulfonate ionomer membranes. *Macromolecules* **25**,(9) 2369-2380 (1992).
- [50] Daniel, V. V. *Dielectric relaxation*. (Academic Press London, 1967).
- [51] Akle, B. J. Characterization and modeling of the ionomer-conductor interface in ionic polymer transducers. *PhD Dissertation*,(Journal Article) (2005).
- [52] Mauritz, K. A. Dielectric relaxation studies of ion motions in electrolyte-containing perfluorosulfonate ionomers. 4. Long-range ion transport. *Macromolecules* **22**,(12) 4483-4488 (1989).

- [53] Wintersgill, M. C. & Fontanella, J. J. Complex impedance measurements on Nafion. *Electrochimica Acta* **43**,(10-11) 1533-1538 (1998).
- [54] Li, J. Y. & Nemat-Nasser, S. Micromechanical analysis of ionic clustering in Nafion perfluorinated membrane. *Mechanics of Materials* **32**,(5) 303-314 (2000).
- [55] Farinholt, K., Newbury, K., Bennet, M. & Leo, D. in *First World Congress on Biomimetics and Artificial Muscles, Albuquerque, NM, 9–11 December 2002*.
- [56] Wallmersperger, T. & Ballhause, D. Coupled chemo-electro-mechanical finite element simulation of hydrogels: II. Electrical stimulation. *Smart Materials and Structures* **17**,(Journal Article) 045012 (2008).
- [57] Aureli, M., Prince, C., Porfiri, M. & Peterson, S. D. Energy harvesting from base excitation of ionic polymer metal composites in fluid environments. *Smart Materials and Structures* **19**,(Journal Article) 015003 (2010).
- [58] Stern, O. The theory of the electric double layer. *Z.Electrochem* **30**,(Journal Article) 508 (1924).
- [59] Bockris, J. O. M. & Devanathan, M. A. V. On the structure of charged interfaces. *Proceedings of the Royal Society of London. Series A, Mathematical and Physical Sciences* **274**,(1356) 55-79 (1963).
- [60] Joly, L., Ybert, C., Trizac, E. & Bocquet, L. Hydrodynamics within the electric double layer on slipping surfaces. *Mol.Phys Phys Rev Lett* **93**,(Journal Article) 257805 (2003).
- [61] Pletcher, D. *A first course in electrode processes*. (Royal Society of Chemistry, 2010).
- [62] Chang, H. C. & Yeo, L. Y. *Electrokinetically Driven Microfluidics and Nanofluidics*. (Cambridge University Press, 2010).
- [63] Gao, F. & Weiland, L. M. in *Proceedings of SPIE*. 72924H.
- [64] van der Heyden, F. H. J., Stein, D. & Dekker, C. Streaming Currents in a Single Nanofluidic Channel. *Physical Review Letters* **95**,(11) 116104 (2005).

- [65] Gao, F. *Computational Study of Ionic Polymers: Multiscale Stiffness Predictions and Modeling of the Electromechanical Transduction* Dissertation/Thesis thesis, University of Pittsburgh, (2010).
- [66] Qu, W. & Li, D. A Model for Overlapped EDL Fields. *Journal of colloid and interface science* **224**,(2) 397-407, doi:10.1006/jcis.1999.6708 (2000).
- [67] Kwak, H. S. & Hasselbrink Jr, E. F. Timescales for relaxation to Boltzmann equilibrium in nanopores. *Journal of colloid and interface science* **284**,(2) 753-758 (2005).
- [68] Di Pasquale, G. *et al.* All-Organic Motion Sensors: Electromechanical Modeling. *Instrumentation and Measurement, IEEE Transactions on* **58**,(10) 3731-3738 (2009).
- [69] Akle, B. J., Habchi, W., Wallmersperger, T., Akle, E. J. & Leo, D. J. High surface area electrodes in ionic polymer transducers: Numerical and experimental investigations of the electro-chemical behavior. *Journal of Applied Physics* **109**,(Journal Article) 074509 (2011).
- [70] Porfiri, M. Influence of electrode surface roughness and steric effects on the nonlinear electromechanical behavior of ionic polymer metal composites. *Physical Review E* **79**,(4) 041503 (2009).
- [71] Curro, J. G. & Mark, J. E. A non-Gaussian theory of rubberlike elasticity based on rotational isomeric state simulations of network chain configurations. II. Bimodal poly (dimethylsiloxane) networks. *The Journal of chemical physics* **80**,(Journal Article) 4521 (1984).
- [72] Bates, T. W. & Stockmayer, W. H. Conformational Energies of Perfluoroalkanes. II. Dipole Moments of H (CF₂) nH. *Macromolecules* **1**,(1) 12-17 (1968).
- [73] Eisenberg, A., Hird, B. & Moore, R. B. A new multiplet-cluster model for the morphology of random ionomers. *Macromolecules* **23**,(18) 4098-4107 (1990).
- [74] Moore, R. B., Cable, K. M. & Croley, T. L. Barriers to flow in semicrystalline ionomers. A procedure for preparing melt-processed perfluorosulfonate ionomer films and membranes. *Journal of Membrane Science* **75**,(1-2) 7-14, doi:10.1016/0376-7388(92)80002-2 (1992).

- [75] Johnson, N. L. SYSTEMS OF FREQUENCY CURVES GENERATED BY METHODS OF TRANSLATION. *Biometrika* **36**,(1-2) 149-176 (1949).
- [76] Cable, K. M., Mauritz, K. A. & Moore, R. B. Anisotropic ionic conductivity in uniaxially oriented perfluorosulfonate ionomers. *Chemistry of Materials* **7**,(9) 1601-1603 (1995).
- [77] Lin, J., Wu, P. H., Wycisk, R., Pintauro, P. N. & Shi, Z. Properties of water in prestretched recast Nafion. *Macromolecules* **41**,(12) 4284-4289 (2008).
- [78] Sharaf, M. A., Kloczkowski, A., Sen, T. Z., Jacob, K. I. & Mark, J. E. Molecular modeling of matrix chain deformation in nanofiber filled composites. *Colloid & Polymer Science* **284**,(7) 700-709 (2006).
- [79] Guth, E. Theory of filler reinforcement. *Journal of Applied Physics* **16**,(1) 20-25 (1945).
- [80] Treloar, L. R. G. *The Physics of Rubber Elasticity*. Vol. 3rd (Clarendon Press, 1975).
- [81] Soboyejo, W. O. *Mechanical properties of engineered materials*. Vol. 152 (Marcel Dekker, 2003).
- [82] Krüger, J. K., Fischer, C. & le Coutre, A. The mono-crystalline state of polyvinylidene fluoride/trifluoroethylene on nano-structured teflon. *Applied Physics A: Materials Science & Processing* **70**,(3) 297-305 (2000).
- [83] Paddison, S. J. Proton Conduction Mechanisms at Low Degrees of Hydration in Sulfonated CID-Based Polymer Electrolyte Membranes. *Annual Reviews in Materials Research* **33**,(1) 289-319 (2003).
- [84] Nemat-Nasser, S. & Wu, Y. Tailoring actuation of ionic polymer metal composites through cation combination. *Smart Structures and Materials 2003* **5051**,(Journal Article) 245-253 (2003).
- [85] Wang, S. & Mark, J. E. Generation of glassy ellipsoidal particles within an elastomer by in situ polymerization, elongation at an elevated temperature, and finally cooling under strain. *Macromolecules* **23**,(19) 4288-4291 (1990).

- [86] Mark, J. E., Abou-Hussein, R., Sen, T. Z. & Kloczkowski, A. Some simulations on filler reinforcement in elastomers. *Polymer* **46**,(21) 8894-8904 (2005).
- [87] Farinholt, K. M. Modeling and characterization of ionic polymer transducers for sensing and actuation. *Mechanics of Materials*,(Journal Article) (2005).
- [88] Aldebert, P., Guglielmi, M. & Pineri, M. Ionic Conductivity of Bulk, Gels and Solutions of Perfluorinated Ionomer Membranes. *Polymer Journal* **23**,(5) 399-406 (1991).
- [89] Chen, Z., Tan, X., Will, A. & Ziel, C. A dynamic model for ionic polymer–metal composite sensors. *Smart Materials and Structures* **16**,(Journal Article) 1477-1488 (2007).
- [90] Elliott, J. A., Hanna, S., Elliott, A. M. S. & Cooley, G. E. Interpretation of the small-angle X-ray scattering from swollen and oriented perfluorinated ionomer membranes. *Macromolecules* **33**,(11) 4161-4171 (2000).
- [91] Halpern, D. & Secomb, T. W. The squeezing of red blood cells through parallel-sided channels with near-minimal widths. *Journal of Fluid Mechanics* **244**,(Journal Article) 307-307 (1992).
- [92] Katritsis, D. *et al.* Wall shear stress: theoretical considerations and methods of measurement. *Progress in cardiovascular diseases* **49**,(5) 307-329 (2007).
- [93] Sparreboom, W., Van Den Berg, A. & Eijkel, J. C. T. Principles and applications of nanofluidic transport. *Nature Nanotechnology* **4**,(11) 713-720 (2009).
- [94] van Honschoten, J. W., Brunets, N. & Tas, N. R. Capillarity at the nanoscale.(Journal Article) (2010).
- [95] Wandschneider, A., Lehmann, J. K. & Heintz, A. Surface tension and density of pure ionic liquids and some binary mixtures with 1-propanol and 1-butanol. *Journal of Chemical & Engineering Data* **53**,(2) 596-599 (2008).
- [96] Stalcup, E. J., Seemann, R., Herminghaus, S. & Law, B. M. Dissipation mechanisms in ionic liquids. *Journal of colloid and interface science* **338**,(2) 523-528 (2009).

- [97] Kocer, B. & Weiland, L. M. in *Proceedings of the ASME 2011 Conference on Smart Materials, Adaptive Structures and Intelligent Systems*. (ASME).
- [98] Kocer, B., Zangrilli, U. & Weiland, L. M. in *Proceedings of the SPIE*. (SPIE).
- [99] Valavala, P. *Multiscale constitutive modeling of polymer materials* PhD thesis, MICHIGAN TECHNOLOGICAL UNIVERSITY, (2008).
- [100] Aluru, N. *Multiscale Simulation of Liquids Under Confinement*. (University of Illinois, Urbana-Champaign, 2011).
- [101] Di Marco, G. B., A.; Carini, G. . Size effect of the alkali cation on the structure and the molecular mobility of polymeric electrolytes. *Journal of Applied Physics* **71**,(12) 5834-5840 (1991).
- [102] Boyd, R. H. Relaxation processes in crystalline polymers: molecular interpretation--a review. *Polymer* **26**,(8) 1123-1133 (1985).
- [103] Satterfield, M. B. & Benziger, J. B. Viscoelastic properties of Nafion at elevated temperature and humidity. *Journal of Polymer Science Part B: Polymer Physics* **47**,(1) (2009).
- [104] Kyu, T. & Eisenberg, A. in *Journal of Polymer Science: Polymer Symposia*.1 edn 203-219 (Wiley Online Library).
- [105] Marrucci, G. & Grizzuti, N. The free energy function of the Doi-Edwards theory: analysis of the instabilities in stress relaxation. *Journal of Rheology* **27**,(Journal Article) 433 (1983).
- [106] Ward, I. M. & Sweeney, J. *An Introduction to the Mechanical Properties of Solid Polymers*. Vol. 2nd (John Wiley & Sons, Ltd., 2004).
- [107] Bokshteĭn, B. S., Mendeleev, M. I. & Srolovitz, D. J. *Thermodynamics and kinetics in materials science: a short course*. Vol. 1 (Oxford university press, USA, 2005).

- [108] Ban, H., Lin, B. & Song, Z. Effect of electrical double layer on electric conductivity and pressure drop in a pressure-driven microchannel flow. *Biomicrofluidics* **4**,(Journal Article) 014104 (2010).
- [109] Israelachvili, J. N. *Intermolecular and surface forces*. (Academic press London, 1992).
- [110] Bennett, M. D. *Electromechanical transduction in ionic liquid-swollen Nafion membranes*,(Journal Article) (2005).
- [111] Gao, F. Dissertation/Thesis thesis, University of Pittsburgh, (2010).
- [112] Kothera, C. S. *Characterization, modeling, and control of the nonlinear actuation response of ionic polymer transducers*,(Journal Article) (2005).
- [113] DuPont. *Fuel Cells: DuPont Nafion membranes and dispersions*, <http://www2.dupont.com/FuelCells/en_US/products/nafion.html> (2012).
- [114] Hensley, J. E., Way, J. D., Dec, S. F. & Abney, K. D. The effects of thermal annealing on commercial Nafion® membranes. *Journal of Membrane Science* **298**,(1-2) 190-201 (2007).
- [115] Alberti, G., Narducci, R. & Sganappa, M. Effects of hydrothermal/thermal treatments on the water-uptake of Nafion membranes and relations with changes of conformation, counter-elastic force and tensile modulus of the matrix. *Journal of Power Sources* **178**,(2) 575-583 (2008).
- [116] DeLuca, N. W. & Elabd, Y. A. Nafion®/poly (vinyl alcohol) blends: Effect of composition and annealing temperature on transport properties. *Journal of Membrane Science* **282**,(1) 217-224 (2006).
- [117] Peron, J. *et al.* Properties of Nafion® NR-211 membranes for PEMFCs. *Journal of Membrane Science* **356**,(1) 44-51 (2010).
- [118] Zawodzinski Jr, T. A. *et al.* A comparative study of water uptake by and transport through ionomeric fuel cell membranes. *Journal of the Electrochemical Society* **140**,(Journal Article) 1981 (1993).

- [119] Li, J., Yang, X., Tang, H. & Pan, M. Durable and high performance Nafion membrane prepared through high-temperature annealing methodology. *Journal of Membrane Science* **361**,(1) 38-42 (2010).
- [120] Standard, A. D638: Standard Test Method for Tensile Properties of Plastics. *ASTM International, West Conchohocken* (2008).
- [121] Standard, A.
- [122] Starkweather Jr, H. W. Crystallinity in perfluorosulfonic acid ionomers and related polymers. *Macromolecules* **15**,(2) 320-323 (1982).
- [123] Li, Q., He, R., Jensen, J. O. & Bjerrum, N. J. Approaches and recent development of polymer electrolyte membranes for fuel cells operating above 100 C. *Chemistry of Materials* **15**,(26) 4896-4915 (2003).
- [124] Page, K. A., Kevin, M. & Moore, R. B. Molecular origins of the thermal transitions and dynamic mechanical relaxations in perfluorosulfonate ionomers. *Macromolecules* **38**,(15) 6472-6484 (2005).
- [125] Yang, Y., Schulz, D. & Steiner, C. A. Physical gelation of hydrophobically modified polyelectrolytes. 1. Homogeneous gelation of alkylated poly [acrylamide-co-sodium acrylate]. *Langmuir* **15**,(13) 4335-4343 (1999).
- [126] Haupt, P. *Continuum mechanics and theory of materials*. (Springer, 2002).
- [127] Andrews, L. C. *Elementary partial differential equations with boundary value problems*. (Academic Press, 1986).
- [128] Kocer, B., Zangrilli, U. & Weiland, L. M. Predicting the streaming current of ionic polymer transducers subjected to Annealing treatment. *To be submitted for publication* (2013).
- [129] Marx, C. L., Caulfield, D. F. & Cooper, S. L. Morphology of Ionomers. *Macromolecules* **6**,(3) 344-353 (1973).

[130] Condor D.C. Power Supplies, I. *Leakage current*,
<<http://www.slpower.com/reference/An113%20Leakage%20Current.pdf>> (2001).